Universidade de Aveiro
2021

Farzin Mohseni

Magnetes Permanentes Nano-Estruturados Isentos de Terras-Raras

Nanostructured rare-earth free permanent magnets

Universidade de Aveiro
2021

Farzin Mohseni

Magnetes Permanentes Nano-Estruturados Isentos de Terras-Raras

Nanostructured rare-earth free permanent magnets

Tese apresentada à Universidade de Aveiro para cumprimento dos requisitos necessários à obtenção do grau de Doutor em Ciência e Engenharia de Materiais, realizada sob a orientação científica do Doutor João Cunha de Sequeira Amaral, Investigador Auxiliar do Departamento de Física da Universidade de Aveiro e co-orientação do Doutor Joaquim Manuel Vieira, Professor Catedrático do Departamento de Engenharia de Materiais e Cerâmica da Universidade de Aveiro.

Apoio financeiro da FCT e do FSE no âmbito do III Quadro Comunitário de Apoio.

o júri

presidente

Prof. Doutor José Carlos Esteves Duarte Pedro
Professor Catedrático, Universidade de Aveiro

Prof. Doutor João Pedro Esteves de Araújo
Professor Associado, Universidade do Porto

Prof. Doutor Bernardo Gonçalves Almeida
Professor Auxiliar Com Agregação, Escola de Ciências da Universidade do Minho

Prof. Doutor Pedro Manuel Lima de Quintanilha Mantas
Professor Auxiliar, Universidade de Aveiro

Prof. Doutor Aurelio Hierro Rodríguez
Professor Ayudante Doctor, Universidade de Oviedo

Doutor João Cunha de Sequeira Amaral
Investigador Auxiliar, Universidade de Aveiro (orientador)

agradecimentos

First, I would like to thank Dr. João Amaral for supervising this thesis and guidance in this work. I am grateful for the chance he gave me to work in collaboration with many talented colleagues in a friendly yet professional environment which allowed me to grow as a researcher. My special thanks go to Prof. Vitor Amaral, who gave me many opportunities to work in his group and supported me through this work. I also thank Prof. Joaquim Vieira for co-supervising this work, all his supports and all brilliant ideas and suggestions to improve the quality of this work. I also want to thank Dr. Rob Pullar who gave me the opportunity to work in his lab and his suggestions and collaborations which facilitated my work.

I would like to thank all the technicians who helped me with the characterisation techniques and all my colleagues and friends at the University for giving me a wonderful experience of working with them.

And last but not least, I thank my parents for their support during all the years of my studies.

palavras-chave

Magnetes permanentes livre de terras raras, Pulverização catódica, Alnico, $BaFe_{12}O_{19}$, $SrFe_{12}O_{19}$, Ferrite hexagonal, Magnetite Fe_3O_4, acoplamento de troca magnética, Magnetes duros de nanocompósitos, Magnetes *exchange-spring*, Compactação a quente, Magnetes ligados a polímeros, Micromagnetismo, Simulações Mumax[3].

resumo

Neste trabalho, exploramos magnetes permanentes nano-estruturados, livres de terras raras, incluíndo filmes finos, nanopartículas e nanocompósitos focando magnetes de Alnico e hexaferrites. Investigamos os efeitos de diferentes condições de tratamento térmico nas propriedades estruturais e magnéticas de filmes finos de Alnico V pulverizados por RF em substratos de Si. Fizemos uma análise mais aprofundada das várias amostras tratadas termicamente para desvendar a origem da alta coercividade nesses filmes finos com uma recentemente descoberta fase Tetragonal Centrada no Corpo (bct) rica em Fe-Co. Os magnetes *exchange-spring* também são explorados, e.g. hexaferrite de bário (BaM) e hexaferrite de estrôncio (SrM). Investigamos a possibilidade de revestir partículas de hexaferrite semelhantes a flocos de BaM e SrM por meio de métodos hidrotérmico e de coprecipitação para preparar nanocompósitos tipo núcleo-casca de BaM/Fe_3O_4 e SrM/Fe_3O_4, onde as partículas de ferrite foram preparadas por meio de método sol-gel de combustão. Mostramos como a relação de fases magnéticas macia e dura, mais as condições de preparação otimizadas, levam a um aprimoramento significativo das suas propriedades magnéticas duras em comparação com pós de ferrite comerciais. Além disso, usando o pó de nanocompósito de alto desempenho, investigamos as propriedades mecânicas e magnéticas do pó do nanocompósito comprimido a quente em uma matriz de epóxi. Mostramos como a combinação pó-resina e as condições de preparação levam à obtenção de propriedades mecânicas otimizadas e a um aprimoramento do produto de energia máxima do magnete composto. Finalmente, realizamos simulações micromagnéticas para melhor compreender e apoiar os resultados experimentais do comportamento de acoplamento de troca dos nanocompósitos magnéticos duros-macios de BaM/Fe_3O_4. Mostramos como a espessura das partículas BaM afetam a coercividade e como a fração de volume de cada fase magnética, assim como a área de interface entre elas, afetam o comportamento de acoplamento de troca bem como o produto energético máximo dos magnetes de nanocompósitos.

Keywords

Rare-earth free Permanent magnets, Sputtering, Alnico, $BaFe_{12}O_{19}$, $SrFe_{12}O_{19}$, Hexagonal Ferrite, Magnetite Fe_3O_4, Magnetic exchange coupling, Nanocomposite hard magnets, Exchange-spring magnets, Warm compaction, Polymer bonded magnets, Micromagnetism, Mumax3 simulations.

Abstract

In this work we explore on the rare-earth free nanostructured permanent magnets, including thin films, nanoparticles and nanocomposites with the focus on Alnico magnets and hexaferrites. Here we investigate the effects of different heat treatment conditions on structural and magnetic properties of RF-sputtered Alnico V thin films on Si substrates. We show an in-depth analysis of the various heat treated samples with high coercivity to unveil the origin of high coercivity in these thin films with a recently discovered Fe-Co rich Body-Centered Tetragonal (bct) phase. Exchange-spring magnets are also explored, namely barium hexaferrite (BaM) and strontium hexaferrite (SrM). We investigate on the possibility of coating BaM and SrM flake-like hexaferrite particles via a hydrothermal and coprecipitation method to prepare core-shell-like BaM/Fe_3O_4 and SrM/Fe_3O_4 nanocomposites, where the ferrite particles where prepared via a sol-gel auto-combustion method. We show how optimised hard to soft magnetic phase ratio and preparation conditions lead to a significant enhancement in their hard magnetic properties compared to commercial ferrite powders. Moreover, we employ the prepared high-performance exchange-coupled nanocomposite powder and investigate the mechanical and magnetic properties of warm compressed nanocomposite powder in an epoxy matrix. We show how the powder-to-resin ratio and preparation conditions lead to optimised mechanical properties, and enhancement in the maximum energy product of the composite magnet. Finally, micromagnetic simulations were employed to better understand and support the experimental results of the exchange coupling behaviour of the BaM/Fe_3O_4 hard-soft magnetic nanocomposites. We show how the thickness of BaM particles affect their coercivity and how the volume fraction of each magnetic phase, together with their interface area, affect the exchange coupling behaviour and maximum energy product of the nanocomposite magnets.

Contents

1 Introduction **1**

1.1 Figure of Merit of Permanent Magnets 2

1.1.1 Saturation Magnetisation 2

1.1.2 Remanence 3

1.1.3 Coercivity 3

1.1.4 Maximum Magnetic Energy Product 4

1.2 Rare Earth Free Permanent Magnets 7

1.2.1 Alnico Magnets 8

1.2.2 Ferrite Magnets 10

1.3 Advanced Nanostructured Magnets 13

1.3.1 Exchange Coupling 13

1.4 Motivation and Plan of Thesis 16

2 Experimental Techniques **21**

2.1 Sample Preparation 21

2.1.1 Alnico V Thin Films 21

2.1.2 BaM-SrM / Fe_3O_4 Nanocomposite Powder 23

2.1.3 Ferrite Based Exchange-Coupled Bonded Magnets 26

2.2 Characterisation Techniques 27

2.2.1 X-ray Analysis 27

2.2.2 Electron Microscopy 31

2.2.3 Superconducting Quantum Interference Device 33

2.2.4 Atomic Force Microscopy 36

2.2.5 Hardness Testing 37

2.2.6 Density Measurements 38

3 High Coercivity Alnico V Thin Films 39

3.1 RF-Sputtering of Alnico V Thin Films 40

3.2 Magnetic Studies of Alnico Thin Films 43

3.3 Structural Studies of Alnico Thin Films 45

3.4 Summary 53

4 Exchange-Coupled BaM/Fe_3O_4 and SrM/Fe_3O_4 Nanocomposites 55

4.1 Single Phase BaM and SrM Nanoparticles 56

4.1.1 $BaFe_{12}O_{19}$ Nanoparticles 56

4.1.2 $SrFe_{12}O_{19}$ Nanoparticles 58

4.2 Synthesis of Fe_3O_4 Nanoparticles 60

4.3 BaM/Fe_3O_4 Nanocomposite 65

4.4 SrM/Fe_3O_4 Nanocomposite 71

4.5 Summary 76

5 Bonded Ferrite-Based Exchange-Coupled Nanocomposite Magnets 79

5.1 Morphological characterisation of the Bonded Magnets 80

5.2 Density of the Bonded Magnet 81

5.3 Mechanical Stability of the Bonded Magnets 83

5.4 Magnetic Properties of the Bonded Magnets 83

5.5 Summary 86

6 Micromagnetic Simulations on the Ferrite Based Nanocomposites 89

6.1 Theory of Micromagnetism 89

6.1.1 Exchange Energy 89

6.1.2 Anisotropy Energy 91

6.1.3 External Field (Zeeman) Energy 93

6.1.4 Stray (Demagnetising, Magnetostatic) Field Energy 94

6.1.5 Micromagnetic Equations 94

6.2 MuMax^3: Numerical Method, Features and Capabilities 96

6.3 Model Description 98

6.3.1 Barium Hexaferrite Grain Model 98
6.3.2 Magnetite Model 99
6.3.3 Nanocomposite Model 100
6.4 Simulation Results 100
6.4.1 Effect of Thickness on the Magnetic Properties of BaM 100
6.4.2 Fe_3O_4: Film vs Grains 101
6.4.3 Nanocomposite Simulation 102
6.5 Summary 108

7 Conclusions and Future Works **109**
7.1 Future works 112

List of Figures

1.1 Hysteresis curve of soft and hard magnetic materials. 2

1.2 Progress in the 20th century in expanding the range of coercivity of the soft and hard magnetic materials. 4

1.3 (a) *MH* vs (b) *BH* curves. 5

1.4 The second quadrant showing both normal and intrinsic hysteresis curves and key figures of merit. Maximum energy product, $BH_{(max)}$, is represented by the shaded area. 6

1.5 Development in the energy product of the permanent magnets in the 20th century. 7

1.6 TEM images and schematics of $\alpha 1$ phase of (a-c) Alnico 5-7, (d-f) Alnico 8, (g-i) Alnico 9. 10

1.7 The schematic structure of $BaFe_{12}O_{19}$. 12

1.8 SEM images of strontium hexaferrite powders produced via a (a) conventional route and (b) sol-gel autocombustion. 13

1.9 Schematic hysteresis loops of a soft magnet, hard magnet and an exchange-coupled magnet. 14

1.10 Schematic of exchange-coupled Hard-Soft magnet. 15

2.1 Schematic diagram of sputtering. 22

2.2 RF sputtering setup used to prepare samples of Alnico V thin film. . . 24

2.3 Exothermic reaction during sol-gel autocombustion method. 25

2.4 a) Hydrothermal and b) coprecipitation synthesizing methods of Fe_3O_4 nanoparticles. 26

2.5 Warm compaction setup and the form bonded magnet sample. 27

2.6 X-ray reflectivity from thin films. 30

2.7 X-ray reflectivity pattern of Alnico V thin film sample deposited for 30 *min* at room temperature. 31

2.8 Principle of SQUID magnetometer. 35

2.9 Indentation of Vickers hardness test on the bonded magnets. 38

3.1 X-ray reflectivity patterns of Alnico V thin films deposited for 10 *min* and 30 *min*. 41

3.2 Illustration of Alnico V thin film samples deposited (a) on Si substrate with the natural SiO_2 layer and with an Ag capping layer, (b) on Si substrate without the SiO_2 layer and with an Ag capping layer, and (c) on Si substrate sandwiched between two layers of Ag. 41

3.3 Surface roughness measurements achieved from an AFM on the as-deposited Alnico V thin film sample prepared at room temperature and the prepared thin film sample from RF sputtering. 42

3.4 AFM analysis on the (a) Alnico V thin film samples heat treated at 600 °C for 1 h followed by quenching, and (b) Alnico V thin film sample deposited at 500 °C. 42

3.5 Room temperature hysteresis loops of the commercial bulk Alnico V and RF-sputtered Ag coated thin films deposited on cleaned Si(100) substrates and annealed at 600 °C, 800 °C and 900 °C in above ambient pressure Ar atmosphere followed by quenching. 44

3.6 Room temperature hysteresis loop of the sample with capping and buffer layers around Alnico thin film and the sample with only the capping layer, both samples annealed at 800 °C in 1.2 bar pressure Ar atmosphere, followed by quenching. 45

3.7 Cross-sectional TEM image of Alnico V thin film sample deposited at room temperature with the silver capping layer. 46

3.8 Cross-sectional TEM image of Alnico V film RF-sputtered onto a Si/SiO_2 substrate annealed at 800 °C followed by quenching. 47

3.9 Cross-sectional TEM image of Ag capped Alnico V thin film sample deposited at 500 °C. 48

3.10 (a) High-resolution TEM image and FFT from the Si substrate (1), a triangular shaped precipitates inside the substrate (2) and (b) HAADF-STEM image of of the sample of Alnico V RF-sputtered onto a Si/SiO_2 substrate and annealed at 800 °C sample. 49

3.11 (a) Cross-sectional STEM image of the 800 °C annealed sample with a coercivity of 1.8 kOe (145 kA/m), (b) Linear EDS. 50

3.12 (a) Cross-sectional STEM image of the thin film Alnico sandwiched between two buffer layers then annealed at 800 °C, (b) Linear EDS. . . . 51

4.1 XRD patterns of the BaM nanoparticles powder (a) calcined at 1000 °C for 5 h, (b) calcined at 600 °C for 1 h, (c) before calcination and (d) the peaks corresponding to BaM phase (JCPDS card no. 43-0002). Rietveld refinement data are also included in (a). The symbol (O) and full line represent the observed and calculated x-ray diffraction profiles, respectively. The vertical bars represent the Bragg reflection positions of the observed phase and the difference curve is plotted in the bottom. 58

4.2 (a) TEM image of the calcined BaM powders at 1000 °C for 5 h and (b) SEM image of the calcined BaM powders at 1000 °C for 5 h. 59

4.3 Room temperature magnetic hysteresis (MH) loops of the BaM powders calcined at different temperatures. 59

4.4 XRD patterns of the SrM nanoparticles powder (a) calcined at 1000 °C for 5 h and (b) the peaks corresponding to SrM phase (JCPDS card no. 43-006-3369). Rietveld refinement data are also included in (a). The symbol (O) and full line represent the observed and calculated x-ray diffraction profiles, respectively. The vertical bars represent the Bragg reflection positions of the observed phase and the difference curve is plotted in the bottom. 61

4.5 (a) TEM image of the calcined SrM powders at 1000 °C for 5 h and (b) SEM image of the calcined SrM powders at 1000 °C for 5 h. 62

4.6 Room temperature magnetic hysteresis (M–H) loop of the SrM powders calcined at 1000 °C for 5 h. 62

4.7 XRD patterns of the Fe_3O_4 nanoparticles synthesised via (a) a coprecipitation and (b) a hydrothermal method; and the peaks corresponding to Fe_3O_4 phase (JCPDS card no. 01-086-1336). Rietveld refinement data are also included in (a) and (b). The symbol (O) and full line represent the observed and calculated x-ray diffraction profiles, respectively. The triangles represent the Bragg reflection positions of the observed phase and the difference curve is plotted in the bottom. 63

4.8 TEM image of the Fe_3O_4 nanoparticles synthesised via (a)-(b) a hydrothermal and (c)-(d) a coprecipitation method. 64

4.9 Particle size distribution of Fe_3O_4 nanoparticles prepared via a hydrothermal and a coprecipitation method. 66

4.10 Room temperature magnetic hysteresis loops of the as-prepared Fe_3O_4 nanoparticles. 67

4.11 XRD patterns of (a) BaM/Fe_3O_4 1:1 nanocomposite powder, (b) the peaks corresponding to BaM phase (JCPDS card no. 43-002), and (c) the peaks corresponding to Fe_3O_4 phase (JCPDS card no. 01-086-1336). Rietveld refinement data are also included in (a) for the BaM/Fe_3O_4 1:1 nanocomposite powder. The symbol (O) and full line represent the observed and calculated x-ray diffraction profiles, respectively. The vertical bars and the triangles represent the Bragg reflection positions of the observed phases and the difference curve is plotted in the bottom. . 68

4.12 TEM image of the as-coated BaM/Fe_3O_4 9:1 nanocomposite powder with different magnifications. 69

4.13 (a) HRTEM of the interface between Fe_3O_4 and BaM nanoparticles in the as-coated 9:1 nanocomposite (b) zoomed in HRTEM image and FFT of the region I, corresponds to BaM nanoparticle, and (c) zoomed in HRTEM image and FFT of the region II, corresponds to Fe_3O_4 nanoparticle. 70

4.14 Room temperature magnetic hysteresis (MH) loops of the BaM powders calcined at 1000 °C for 5 h, as-prepared Fe_3O_4 nanoparticles, as-coated BaM/Fe_3O_4 nanocomposite powder with different mass ratios and BaM/Fe_3O_4 9:1 nanocomposite annealed at 300 °C and 600 °C for 1 h. 71

4.15 Switching field distribution curves (dM/dH of demagnetisation curves) of the BaM nanoparticles calcined at 1000 °C for 5 h, as-prepared Fe_3O_4 nanoparticles and BaM/Fe_3O_4 nanocomposite powder with different mass ratios. 72

4.16 XRD patterns of SrM/Fe_3O_4 9:1 nanocomposite powder. The corresponding peaks of SrM phase (JCPDS card no. 04-006-3369), and Fe_3O_4 phase (JCPDS card no. 01-086-1336) are marked. Rietveld refinement data are also included in (a) for the SrM/Fe_3O_4 9:1 nanocomposite powder. The symbol (O) and full line represent the observed and calculated x-ray diffraction profiles, respectively. The vertical bars and the triangles represent the Bragg reflection positions of the observed phases and the difference curve is plotted in the bottom. 73

4.17 TEM image of the as-coated SrM/Fe_3O_4 9:1 nanocomposite powder with different magnifications. 74

4.18 (a) HRTEM of the interface between Fe_3O_4 and SrM nanoparticles in the as-coated 9:1 nanocomposite (b) zoomed in HRTEM image and FFT of the region I, corresponds to SrM nanoparticle, and (c) zoomed in HRTEM image and FFT of the region II, corresponds to Fe_3O_4 nanoparticle. 74

4.19 Room temperature magnetic hysteresis (M–H) loops of the SrM powders calcined at 1000°C for 5 h, as-prepared Fe_3O_4 nanoparticles prepared via a coprecipitation method and as-coated SrM/Fe_3O_4 9:1 nanocomposite powder. 75

4.20 Switching field distribution curves (dM/dH of demagnetisation curves) of the SrM nanoparticles calcined at 1000 °C for 5 h, as-prepared Fe_3O_4 nanoparticles via a coprecipitation method and SrM/Fe_3O_4 9:1 nanocomposite powder. 76

5.1 SEM images of the epoxy bonded SrM/Fe_3O_4 composite warm pressed at 300 MPa with a ferrite powder component of (a) 80 wt.%, (b-c) 95 wt.% and (d) cross section SEM image of SrM/Fe_3O_4 composite with 95 wt.% ferrite content. 81

5.2 SEM images of the epoxy bonded BaM/Fe_3O_4 composite warm pressed at 300 MPa with a ferrite powder component of (a) 80 wt.% and (b) 95 wt.%. 82

5.3 Variation of density with compaction pressure and powder to resin ratio of (a) the epoxy bonded BaM/Fe_3O_4 composite magnet and (b) the epoxy bonded SrM/Fe_3O_4 composite magnet. 82

5.4 Variation of Vickers hardness with compaction pressure and powder to resin ratio of (a) the epoxy bonded BaM/Fe_3O_4 composite magnet and (b) the epoxy bonded SrM/Fe_3O_4 composite magnet. 83

5.5 Room temperature *MH* curves of the BaM/Fe_3O_4-based bonded magnets with different ferrite concentrations and warm compaction pressures compared to the parent exchange-coupled BaM/Fe_3O_4 nanocomposite powder. The inset shows the demagnetisation curve of the BaM/Fe_3O_4-based bonded magnets with different concentrations all prepared at 300 MPa. 84

5.6 Room temperature *MH* curves of the BaM/Fe_3O_4-based bonded magnets with different ferrite concentrations and warm compaction pressures compared to the parent exchange-coupled SrM/Fe_3O_4 nanocomposite powder. The inset shows the demagnetisation curve of the SrM/Fe_3O_4-based bonded magnets with different concentrations all prepared at 300 MPa. 85

5.7 Variations of (a) $BH_{(max)}$, (b) H_{ci} and (c) M_s, with compaction pressure and powder to resin ratio of the epoxy bonded BaM/Fe_3O_4 and SrM/Fe_3O_4 composite magnet. 87

6.1 The reduced magnetisation unit vectors at neighbouring sites i and j. . 91
6.2 Uniaxial anisotropy energy density when $K_1 > 0$ (right) and $K_1 < 0$ (left). 93
6.3 Cubic anisotropy energy density when $K_1 > 0$ (right) and $K_1 < 0$ (left). 93
6.4 Schematic of a 2D FD discretisation of space. 97
6.5 BaM model with 300 nm grain size, which the magnetic field was applied in z direction (Hz). The initial magnetisation set to random. The arrows represent the magnetocrystalline anisotropy of each grain. 98
6.6 Fe_3O_4 Model with (a) 10 nm sized layers and (b) 10 nm grain sized, to which the magnetic field was applied in z direction (Hz). The initial magnetisation set to random. The arrows represent the magnetocrystalline anisotropy of each grain. 99
6.7 Schematic of the model used for coated BaM with Fe_3O_4 layers. Each layer of BaM nanoparticles is coated with 1, 2, or 3 layers of Fe_3O_4 films or nanoparticles. 100
6.8 *MH* curves of 300nm sized BaM grains with different thicknesses. . . . 101
6.9 Dependence of intrinsic coercivity on thickness of simulated 300 nm sized BaM grains. 102
6.10 *MH* curves of 10 nm sized Fe_3O_4 grains and 10 nm sized Fe_3O_4 film. . . 103
6.11 *MH* curves of up to 3 layers of 10 nm sized Fe_3O_4 films coated on 90 nm sized BaM layer. 104
6.12 *MH* curves of up to 3 layers of 10 nm sized Fe_3O_4 particles coated on 90 nm sized BaM layer. 105
6.13 Comparison between the (a) H_{ci}, and (b) $BH_{(max)}$ of the simulation and experimental results of BaM/Fe_3O_4 with different BaM volume fractions. 106
6.14 Variation of H_{ci} with average thickness of the soft ferrite. 107

List of Tables

1.1 Typical values for the most important magnetic properties of some permanent magnets [20, 21]. 8

1.2 Compositional differences and magnetic properties of commercial grades of Alnico magnets [28]. 9

3.1 A summary of the effects of deposition temperature, post heat treatment conditions on M_s and H_{ci} of Alnico V thin films deposited on Si substrates without the SiO_2 layer. 52

4.1 The magnetic properties of the investigated nanoparticles and nanocomposite samples and the commercial BaM powder, as well as data from Refs [55, 56]. 77

5.1 A comparison between magnetic properties of our investigated samples with a commercial SrM based bonded magnet. 88

Nomenclature

List of Abbreviations

AC	Alternating current
AFM	Atomic force microscopy
BaM	Barium hexaferrite
bcc	Body centred cubic
bct	Body centred tetragonal
BET	Brunauer Emmett Teller
DC	Direct current
EDS	Energy-Dispersive X-ray Spectroscopy
fcc	Face centred cubic
FD	Finite difference
FFT	Fast Fourier transform
FWHM	Full width half maximum
GPU	Graphics processing unit
HAADF	High angle annular dark field
hcp	Hexagonal closed packed
HRTEM	high resolution transmission electron microscopy
HV	Vickers hardness
LL	Landau Lifshitz
LLG	Landau Lifshitz Gilbert
PBC	Periodic boundary conditions
PVD	Physical vapour deposition
RF	Radio frequency
SAED	Selected area electron diffraction

SEM	Scanning electron microscopy
SFD	Switching field distribution
SQUID	Superconducting quantum interference device
SrM	Strontium hexaferrite
STEM	Scanning transmission electron microscopy
TEM	Transmission electron microscopy
UTS	Ultimate tensile strength
VSM	Vibrating sample magnetometer
XRD	X-ray diffraction

List of Symbols

α	Gilbert damping coefficient
γ	Gyromagnetic ratio
J	Exchange Constant
A_s	Exchange stiffness
$BH_{(max)}$	Maximum magnetic energy product
B	Magnetic induction
d_{cr}	Critical exchange length
E_{anis}	Anisotropy energy
E_{demag}	Demagnetising energy
E_{exch}	Exchange energy
E_{Zeeman}	Zeeman energy
H_{ci}	Intrinsic coercivity
H_c	Coercivity
H_{eff}	Effective field
H	Magnetic field
K_H	Magnetocrystalline anisotropy
l_{ex}	Exchange length
M_r	Remanence
M_s	Saturation magnetisation
M	Magnetisation
T_C	Curie temperature

Chapter 1

Introduction

Magnetic materials are essential for modern lifestyle and industries. They are used in many electronic devices and medical equipment, and in emerging energy applications, such as renewable energy conversion and refrigeration. They also play a major role in electric motors, wind turbines and hydroelectric power generators, and hybrid car motors. For the past couple of centuries, electric motors played the main role in the technological society. In developed countries, nearly 20% of the produced electricity is consumed by electric motor devices in the industrial sectors. Therefore, a few percent of improvement in the efficiency of these electrical motors leads to saving of billions of dollars and reduction of CO_2 emissions. Thus, high-performance hard and soft magnets are necessary to make electric devices lighter and more energy efficient [1–4]. Considering the current applications, magnetic materials can be divided into two main groups: soft magnetic materials, which are easy to magnetise and demagnetise, and hard magnetic materials, which are hard to magnetise and demagnetise. Soft magnetic materials, such as iron, cobalt, nickel etc., have high permeability and low coercivity. On the other hand, the primary requirement of hard magnetic materials is high coercivity. The high coercivity is essential to increase the resistance to demagnetisation of the hard magnets, making them suitable to be used as permanent magnets [5]. Examples of hard magnetic materials are Alnico, barium and strontium ferrites and neodymium magnets. Figure 1.1 shows the distinguished characterisations of hard and soft magnetic materials.

The focus in this work is to improve characteristics of rare-earth free permanent

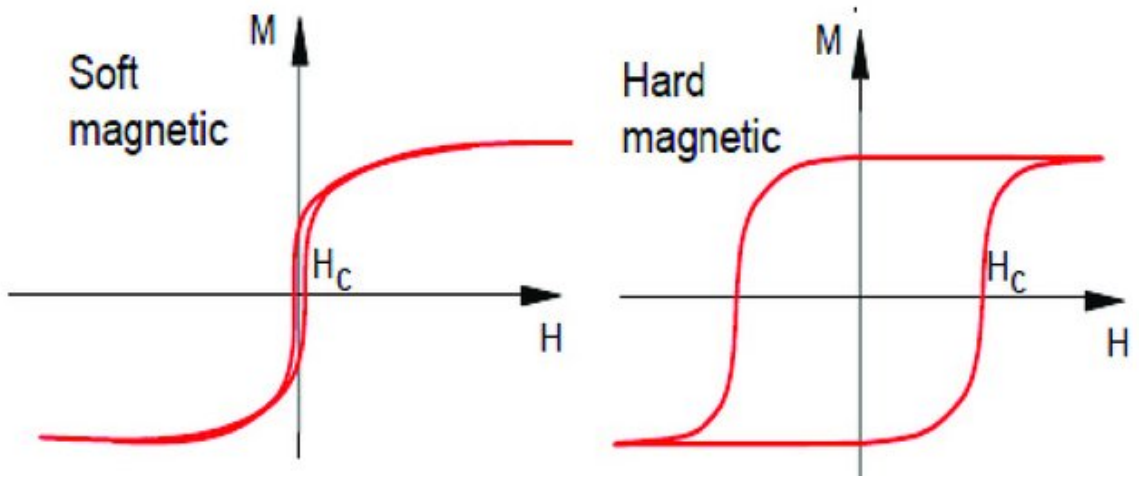

Fig. 1.1: Hysteresis curve of soft and hard magnetic materials [6].

magnets namely Alnico magnets and ferrite-based magnets. Before going any further, we shall first explore the main characteristics of magnetic materials.

1.1 Figure of Merit of Permanent Magnets

In ferromagnetic materials, the magnetisation (M) has a nonlinear response to an applied magnetic field (H) and shows hysteresis behaviour (Figure 1.1). Several features, that represent the magnetic properties of a magnetic material, characterise the hysteresis loop. In this section, we will explore the key features of ferromagnetic materials derived from the MH curves.

1.1.1 Saturation Magnetisation

At large enough values of the applied magnetic field, the magnetisation reaches its highest possible value. This constant value is called saturation magnetisation (M_s). Spontaneous magnetisation depends on temperature and on heating falls sharply to zero at the Curie temperature (T_C). Ferromagnetic elements such as Fe, Co and Ni, which have T_C values above 600 K, show a spontaneous magnetisation M_s of 1720, 1370 and 485 kA/m (or emu/cm^3 in cgs) at room temperature, respectively. For magnetic ferrites such as magnetite (Fe_3O_4) and barium ferrite ($BaFe_{12}O_{19}$) the room temperature M_s are 480 and 380 kA/m (emu/cm^3), respectively [7, 8]. Magnetite

and barium ferrite have a Curie temperature of 856 K and 723 K. To date, no new ferromagnetic material has been discovered with a M_s greater than that of "Premendur" alloy, $Fe_{65}Co_{35}$, discovered around 1920, with M_s of 1950 kAm^{-1} (Js = 2.45 T) [8].

1.1.2 Remanence

As can be seen in Figure 1.1, when the external magnetic field is removed from a ferromagnetic materials, the magnetisation does not reduce to zero. The residual magnetisation at $H = 0$ is called remanence (M_r).

1.1.3 Coercivity

In order to remove the magnetisation of a ferromagnetic material, a negative external field has to be applied. The intensity of the negative external field that removes the magnetisation (M=0) is called intrinsic coercivity (H_{ci}). Coercivity measures the resistance of the ferromagnetic material to become demagnetised. The coercivity is an important parameter to distinguish between a soft and hard magnetic material. Figure 1.2 shows the progress in the 20th century in expanding the range of coercivity of soft and hard magnetic materials [8, 9].

1.1.3.1 Intrinsic Coercivity and Coercivity

When a ferromagnetic material is exposed to an external field H, the magnetic induction inside the sample is referred as B. The total magnetisation M is given by the total magnetic moments m per unit volume V. We then have:

$$M = \frac{1}{V}\sum_{V} m, \tag{1.1}$$

$$B = H + 4\pi\mathrm{M}\ (\mathrm{cgs}), \tag{1.2}$$

$$B = \mu_0(\mathrm{H+M})\ (\mathrm{SI}), \tag{1.3}$$

where μ_0 is the magnetic permeability of free space ($\mu_0 \approx 4\pi \times 10^{-7}$ $\mathrm{N.A^{-2}}$).

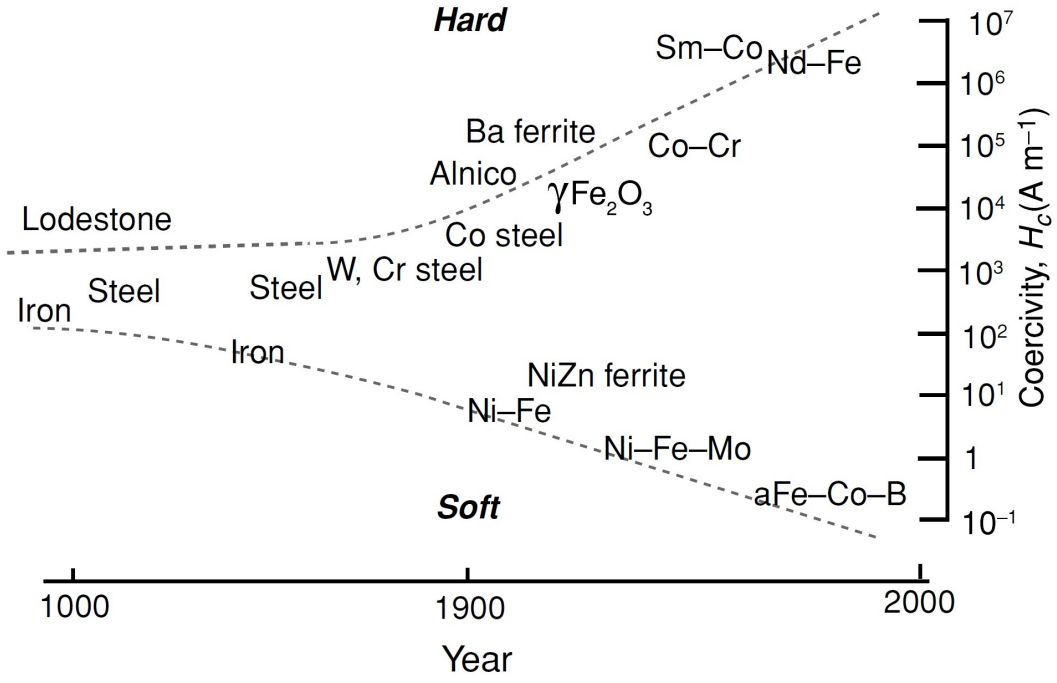

Fig. 1.2: Progress in the 20th century in expanding the range of coercivity of the soft and hard magnetic materials [8].

Both B vs. H and M vs. H show nonlinear hysteresis loops due to the magnetic domains existing in ferromagnetic materials. The curves differ at the saturation point where it reaches a horizontal straight line in the MH plot whereas the constant magnetic susceptibility is reflected as a slope in the BH plot. Figure 1.3 shows an illustration of how the MH and BH hysteresis loops may differ in ferromagnetic materials. As seen in Figure 1.3, the value of coercivity is also different in both curves, where the intrinsic coercivity (H_{ci}) is the reverse external magnetic field required to remove the magnetisation M from the remnant magnetisation M_r and coercivity (H_c) is a reverse external magnetic field required to remove the induced magnetisation B from the remnant induced magnetisation Br [9].

1.1.4 Maximum Magnetic Energy Product

The product BH has the unit of J/m^3 in the SI units and G.Oe in the cgs units. The point in the second quadrant of the hysteresis loop, also known as the demagnetisation curve, where the area of the rectangle under the BH curve is maximised defines maxi-

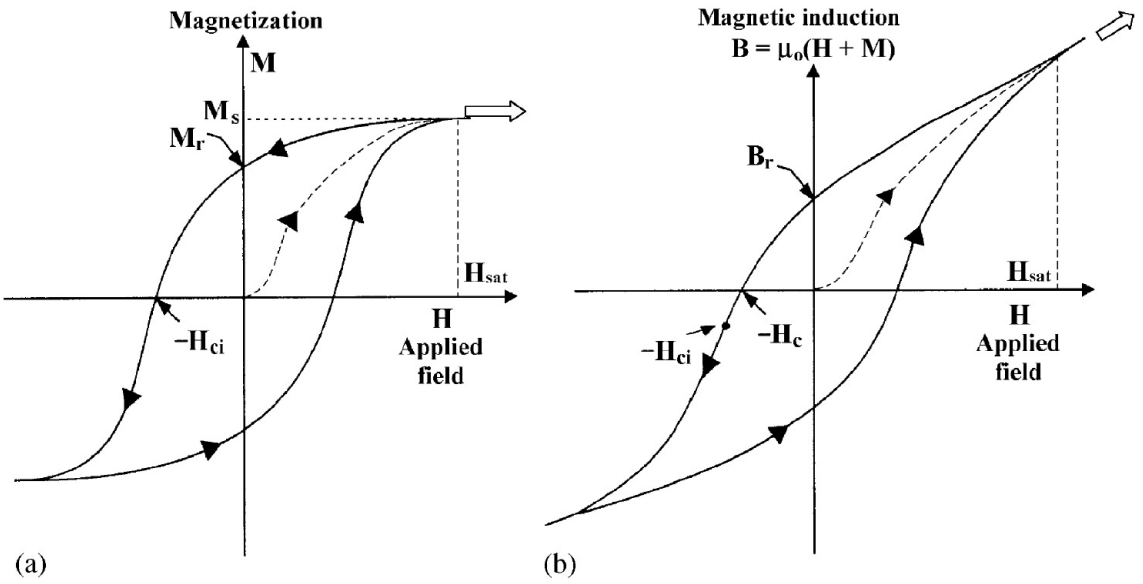

Fig. 1.3: (a) MH vs (b) BH curves. [9].

mum energy product ($BH_{(max)}$) (Figure 1.4). This is the key figure of merit for a hard magnet, and determines the maximum amount of magnetic energy that can be stored in the permanent magnet [10].

The theoretical maximum magnetic energy product is calculated as:

$$BH_{(\max)} = \frac{\mu_0 {M_r}^2}{4}, \tag{1.4}$$

which has been estimated to be 125 MG.Oe (1 MJ/m^3) [12]. Development in the energy product of the permanent magnets increased rapidly by the beginning of 20th century, as a result of using iron-based tungsten steel and cobalt steels with high magnetisation as permanent magnets, with $BH_{(max)} \approx 1$ MG.Oe (≈ 8 kJ/m^3) for the steels discovered during the early part of the century [1]. Alnico magnets, alloys of Fe with Al, Ni and Co, were the first advanced hard magnetic materials developed between 1930 and 1970. They are hard ferromagnets with high magnetisation and Curie temperatures above 800 °C. The main drawback in applications of Alnico alloys is their relatively low coercive field, below 700 Oe for the most used Alnico 5 or up to 1500 Oe for optimised Alnico 8 compositions [13–16]. In 1950s Philips laboratories introduced a new generation of permanent magnets by developing the barium and strontium hexaferrites (Ba/Sr)$Fe_{12}O_{19}$. These ceramics showed lower Curie temperature and magnetisation

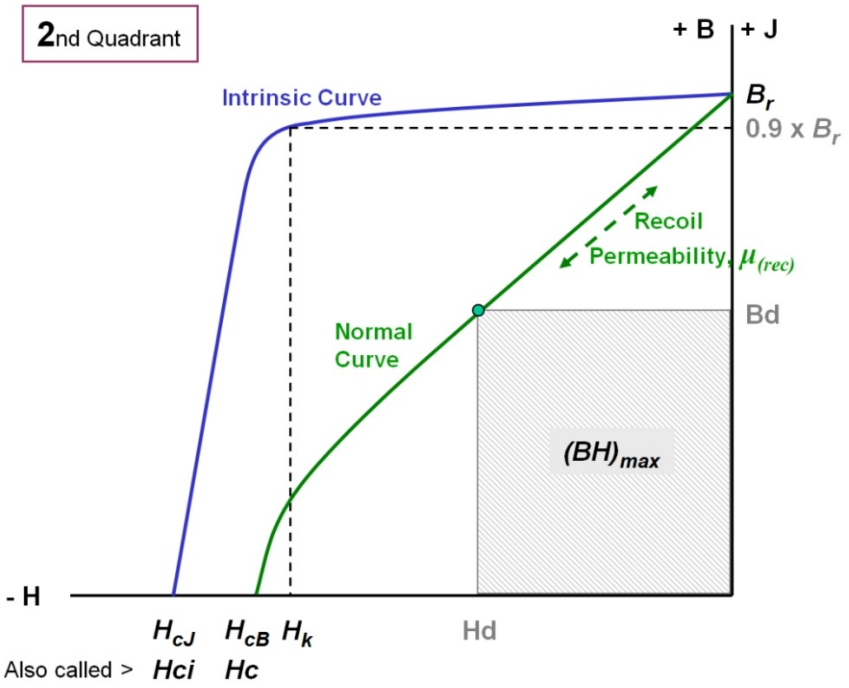

Fig. 1.4: The second quadrant showing both normal and intrinsic hysteresis curves and key figures of merit. Maximum energy product, $BH_{(max)}$, is represented by the shaded area [11].

comparing to Alnico magnets. However, the main advantage of these ceramic magnets is their very large coercivities due to the large magnetocrystalline anisotropy [17]. Figure 1.5 shows the development of permanent magnets during the last century [1]. The major development in the energy product of the permanent magnets occurred in the 1960s with the discovery of $SmCo_5$, the first generation of rare-earth based permanent magnets. These magnets showed much larger energy product and coercivity comparing to previous permanent magnets. They also have high Curie temperature making them useful for high-temperature applications [18]. The high price of Sm and Co sparked numerous attempts to produce permanent magnets with similar characteristics of Sm-Co magnet in the 1970s and 1980s. In 1984 Sagawa et al. [19] reported sintered and quenched $Nd_2Fe_{14}B$ as the new iron-based rare-earth-based permanent magnet of high energy product. The energy products of the Nd-based magnets, the third generation of rare-earth magnets, were surprisingly larger than in the Sm-based magnets. Since the introduction of Nd-based magnets, they have become the most attractive permanent magnets in the growing market. The developments in the en-

ergy product of the rare-earth permanent magnets during the past decades showed an improvement from ≈ 1 MG.Oe (≈ 8 kJ/m^3), for iron-based tungsten steels, to ≈ 3 MG.Oe (≈ 24 kJ/m^3), for hexagonal ferrites, and finally peaked to ≈ 56 MG.Oe (≈ 445 kJ/m^3) for neodymium-iron-boron magnets [1, 2, 10].

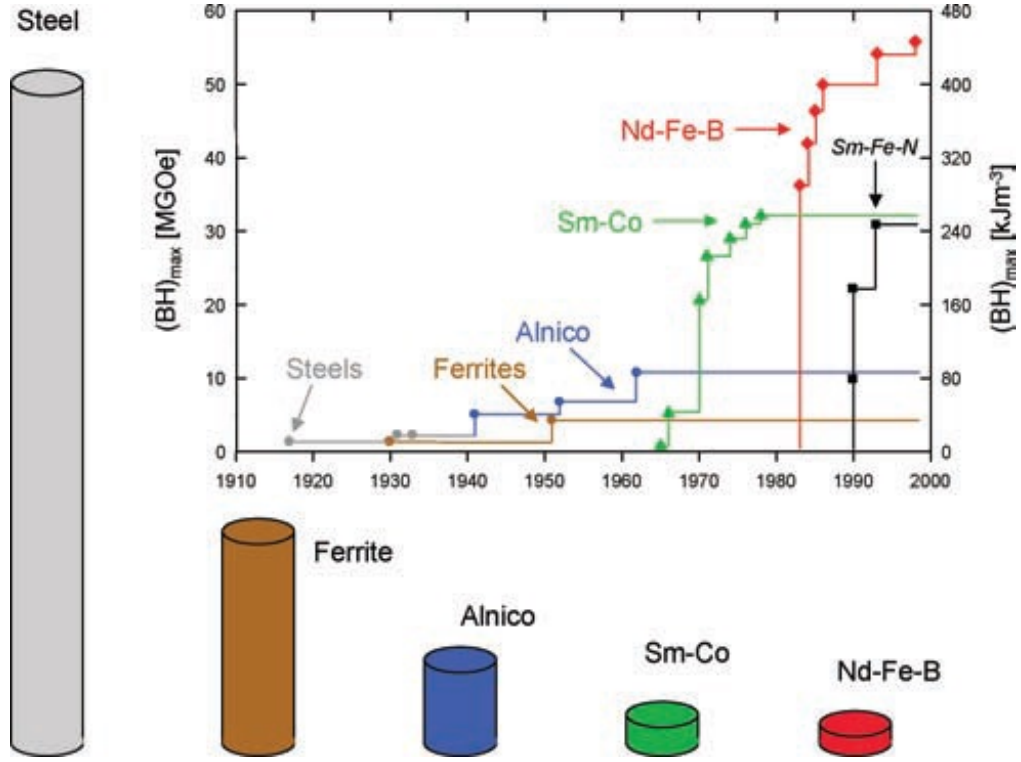

Fig. 1.5: Development in the energy product of the permanent magnets in the 20th century [1].

Table 1.1 shows the most relevant hard magnetic properties of the frequently used permanent magnets.

1.2 Rare Earth Free Permanent Magnets

The main concern about the $Nd_2Fe_{14}B$ magnets is the relatively low magnetocrystalline anisotropy and Curie temperature (≈ 300 °C). In order to increase the operating temperature of Nd-based permanent magnets above ≈ 180 °C, typical in electric car motors, a significant amount of heavy rare-earth elements (mainly Dy and Tb) must be added to their composition [22–24]. For the excellent properties and relatively low prices of the Nd-based magnets, they became the most important permanent magnets

Table 1.1: Typical values for the most important magnetic properties of some permanent magnets [20, 21].

Material	Category	Br (T)	H_c (kA/m)	H_{ci} (kA/m)	$BH_{(max)}$ (kJ/m^3)	T_W* (°C)	T_C (°C)
$MO{\cdot}6(Fe_2O_3)$	Ferrite	0.2-0.4	150-290	200-380	8-30	250	450
Alnico	Alloy	0.7-1.3	40-150	40-170	10-70	450-550	810-860
$SmCo_5$	Rare Earth	0.85-0.95	600-720	1300-2400	130-180	250-300	685-700
$Nd_2Fe_{14}B$	Rare Earth	1.0-1.4	760-1030	880-3300	190-400	125-150	310

* T_W represents the maximum working temperature of the permanent magnet.

in the market in the past two decades. Currently Asia produces nearly the entire global output of rare-earth metals (in particular, heavy rare-earths), which makes the production of the current high performance rare earth magnets heavily dependent on supply from this particular region. Rare-earth based magnets are the heart of many modern technologies such as mobile phones, laptops and even highly efficient washing machines. High-performance permanent magnets are also essential in the green economy. To put it into a perspective, an electric car carries $\sim$ 5 kg of rare-earth-based magnets. Around 2 tonnes of rare-earth-based magnets are included in a wind turbine. The demand for high rare-earth elements is booming from $\sim$ 30,000 tonnes in the 1980s to $\sim$ 200,000 tonnes in 2015 [25]. Because of the relatively recent hike in 2011 in the prices of rare-earth elements, and environmental issues with the mining and processing of these elements, there has been a significant interest in the development of rare-earth free permanent magnets for the European and US industry [1, 2, 26, 27].

1.2.1 Alnico Magnets

Alnico alloys are mainly composed of iron and cobalt, with about 30% of Al, Ni, Cu, and Ti in some of its grades. This class of magnets takes advantage of the spinodal

decomposition of the alloy during cooling into two body centred cubic (bcc) phases, the Fe-Co-rich rod precipitates ($\alpha 1$) and the Al-Ni-rich matrix ($\alpha 2$). The anisotropic growth of the $\alpha 1$ phase causes an anisotropic hysteretic response to the external magnetic field. The origin of the coercivity in Alnico alloys is mainly the shape anisotropy. Compared to the permanent magnets with high magnetocrystalline anisotropy, the shape anisotropy of Alnico alloys leads to lower values of coercivity and $BH_{(max)}$. Several grades of Alnico alloys contain a number of minor additives, such as Ti, Nb and Cu, and receive complex heat treatments under a strong magnetic field to optimise the magnetic properties. Table 1.2 shows the compositional differences and magnetic properties of commercial grades of Alnico magnets [28, 29].

Table 1.2: Compositional differences and magnetic properties of commercial grades of Alnico magnets [28].

Commercial grade	Composition (wt. %)							Br (kG)	H_{ci} (Oe)
	Fe	Co	Ni	Al	Cu	Nb	Ti		
5-7	49.9	24.3	14.0	8.2	2.3	1.0	0.0	13.5	740
8	30.0	40.1	13.0	7.1	3.0	0.0	6.5	7.4	1900
9	35.5	35.4	13.1	7.0	3.2	0.5	5.0	11.2	1375

Alnico 5-7, with the highest concentration of Fe in their composition, have the highest Br and the lowest H_{ci}. On the other hand, Alnico 8 with the least amount of Fe content have the lowest Br and highest H_{ci}. Alnico 9 has the highest $BH_{(max)}$ of $\sim$ 10 MG.Oe with values of H_{ci} and Br in between of the other grades. Figure 1.6 shows transmission electron microscopy (TEM) images and schematics of $\alpha 1$ phase in different grades of Alnico magnetic alloys. Alnico 5-7 and 9 have a high degree of grain alignment with most of the $\alpha 1$ grains aligned along [001] direction. These grades are produced by casting in a heated cylindrical die with a chilled bottom plate, to impose directional solidification, followed by a heat treatment in an external magnetic field aligned to the casting direction. In contrast to Alnico 5-7 and 9, grains in Alnico 8 are randomly distributed. Alnico 8 alloys are usually heat-treated at higher temperatures with the external magnetic field along the cylinder axis [28].

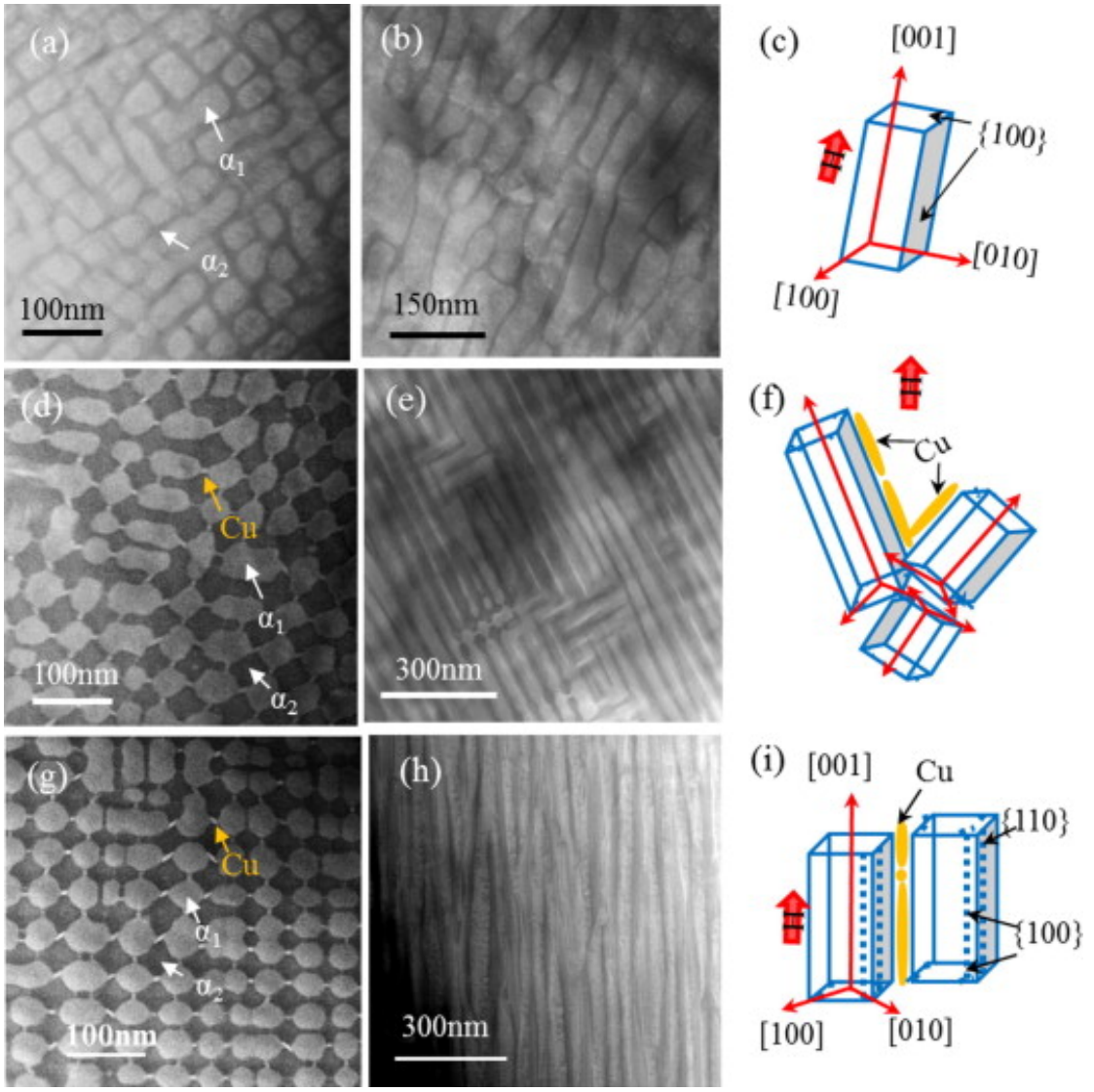

Fig. 1.6: TEM images and schematics of $\alpha 1$ phase of (a-c) Alnico 5-7, (d-f) Alnico 8, (g-i) Alnico 9 [28].

1.2.2 Ferrite Magnets

Hexaferrites have a crystal structure similar to the natural mineral magnetoplumbite, ($PbFe_{7.5}Mn_{3.5}Al_{0.5}Ti_{0.5}O_{19}$) without Ti, Al and Mn, and with the general structure of $MO{\cdot}6Fe_2O_3$ or $MFe_{12}O_{19}$, where the M ion is divalent [30]. Hexaferrite magnets were born out of the need for high coercivity which could not be provided by Alnico magnets. With coercivities around 2.5 kOe (200 kA/m), these ferrites can easily be produced in powder form and then shaped as required. Barium hexaferrite ($BaFe_{12}O_{19}$) and strontium hexaferrite ($SrFe_{12}O_{19}$) are among the best-known examples of M-type

hexaferrites which are technologically important and constitute more than 50% of the global consumption of magnetic materials [31]. The large Ba and Sr ions in their crystalline structure cause a slight distortion of the crystalline lattice, which is responsible for the large magnetocrystalline anisotropy.

Figure 1.7 shows the crystalline structure of barium hexaferrite. The M-type barium hexaferrite has lattice constants of a = 5.89 Å and c = 23.19 Å with a hexagonal closed packed (hcp) lattice structure of oxygen and Ba. The M-type strontium hexaferrite has identical crystalline structure with lattice constants a = 5.88 Å and c = 23.05 Å. Fe atoms are in octahedral (12k, 4f2, and 2a), tetrahedral (4f1), and trigonal bipyramidal/hexahedral (2b) sites. The Fe^{3+} cations are the source of magnetic moments in the structure where the Fe ions in the 12k, 2a, and 2b sites are spin up and the ones in 4f1 and 4f2 sites are spin down. The hexagonal structure with the space group of P63/mmc is constructed from 4 building blocks of S, S*, R, and R* with ten layers of oxygen atoms along the c-axis. The stared blocks (S* and R*) have the same structure as the ones without the star with a 180° rotation around the c-axis. The S and S* ($Fe_6^{3+}O_8^{2-}$) blocks have the structure of spinel ferrites with 2 oxygen layers and six Fe^{3+} ions. The R and R* blocks ($Ba^{2+}Fe_6^{3+}O_{11}^{2-}$) with hexagonal structures consist of three oxygen layers with one of the oxygen anions replaced by Ba or Sr and six Fe^{3+} ions. Each Fe^{3+} ion contributes 5 μ_B to the magnetic moment at 0 K. Therefore, the total magnetisation at 0 K can be calculated as 20 μ_B (eight Fe^{3+} ions are in the spin up state, and four are in spin down state) [32–34].

Hard magnetic hexagonal barium and strontium ferrites are suitable for numerous applications such as permanent magnets, electronic components, electromagnetic absorbers and also as a magnetic recording material, due to their low cost, high electrical resistivity, high oxidation and corrosion resistance, great chemical stability, large H_c, and high T_C, [31, 35]. Many of these applications require controlled particle size and magnetic properties, as well as homogeneous structure. There are several ways to prepare Ba/Sr hexaferrites. In the conventional method, submicron powders of barium carbonate ($BaCO_3$) or strontium carbonate ($SrCO_3$) are mixed with iron oxide (Fe_2O_3) followed by calcination at > 1200 °C and a prolonged ball milling of the calcined powder which results in powders with particles of small aspect ratio [36]. There are several

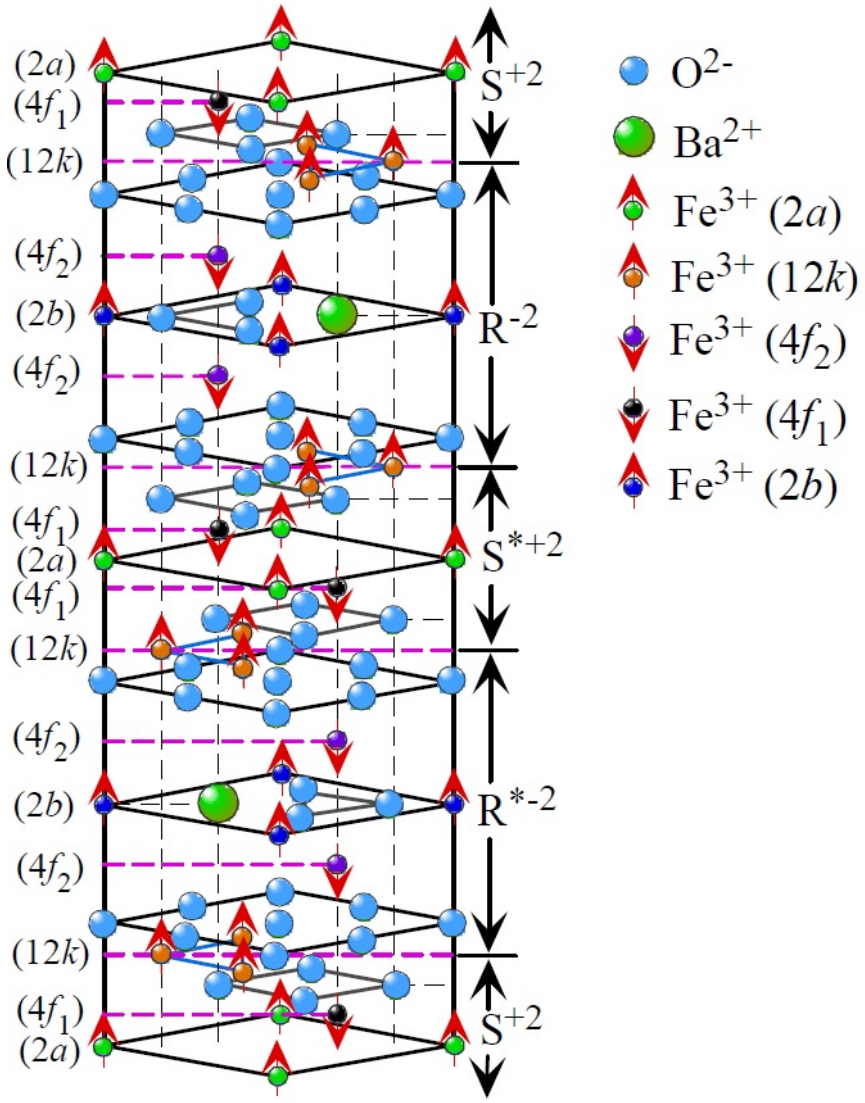

Fig. 1.7: The schematic structure of $BaFe_{12}O_{19}$ [34].

chemical synthesis techniques such as co-precipitation [37], hydrothermal [38] or sol-gel auto-combustion [39] to prepare the M-type ferrites which require lower calcination temperatures ($\sim$ 1000 °C). As a result of these chemical routes, hexagonal shaped plate-like particles of smaller size with high aspect ratio and larger coercivity can be produced. Figure 1.8 makes the comparison between the morphology of strontium hexaferrite powders produced via a conventional synthesis and a sol-gel auto-combustion method [36].

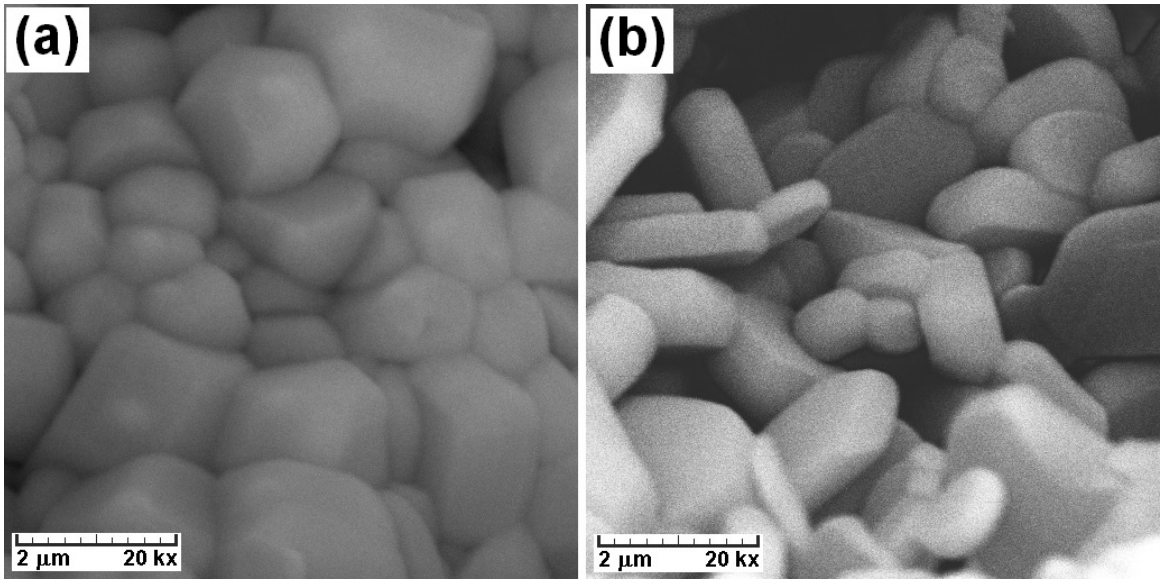

Fig. 1.8: SEM images of strontium hexaferrite powders produced via a (a) conventional route and (b) sol-gel autocombustion [36].

1.3 Advanced Nanostructured Magnets

A new generations of hard magnets, the exchange-coupled nanocomposites, contain different soft and hard magnetic phases in nanoscale morphology. By using these composite permanent magnets, it is possible to design magnets for different applications. For instance, in applications which require magnets in high temperature, nanocomposites of Sm-Co as the hard phase, and Fe or Fe-Co as the soft phase, could be used [40].

1.3.1 Exchange Coupling

The concept of exchange-coupled (also referred as exchange-spring) magnets was first introduced by Coehoorn et al. in 1989 [41]. Their investigations showed an enhancement in the remanence of the $Nd_2Fe_{14}B/Fe_3B$ composite, which they described as of the exchange coupling between the grains. Later in 1991, Kneller et al. [42] showed the possibility to produce high-performance permanent magnets by coupling soft and hard magnetic phases in a nanocomposite. Their simulations showed that the amount of hard phase in the composite could be less than 15% of the volume, thus reducing drastically the overall cost of the materials of the permanent magnets. Further inves-

tigations on this concept by Panagiotopoulos et al. [43], Skomski and Coey [12] and Schrefl et al. [44] showed the theoretical possibility to enhance the energy product of exchange-coupled magnets up to $\sim$ 120 MG.Oe (956 kJ/m^3), which is almost twice the energy product of the best single-phase rare-earth permanent magnets. Figure 1.9 shows schematic hysteresis loops of a soft magnet, hard magnet and an exchange-coupled magnet, which leads to a larger $BH_{(max)}$ in the composite magnet compared to the parent phases.

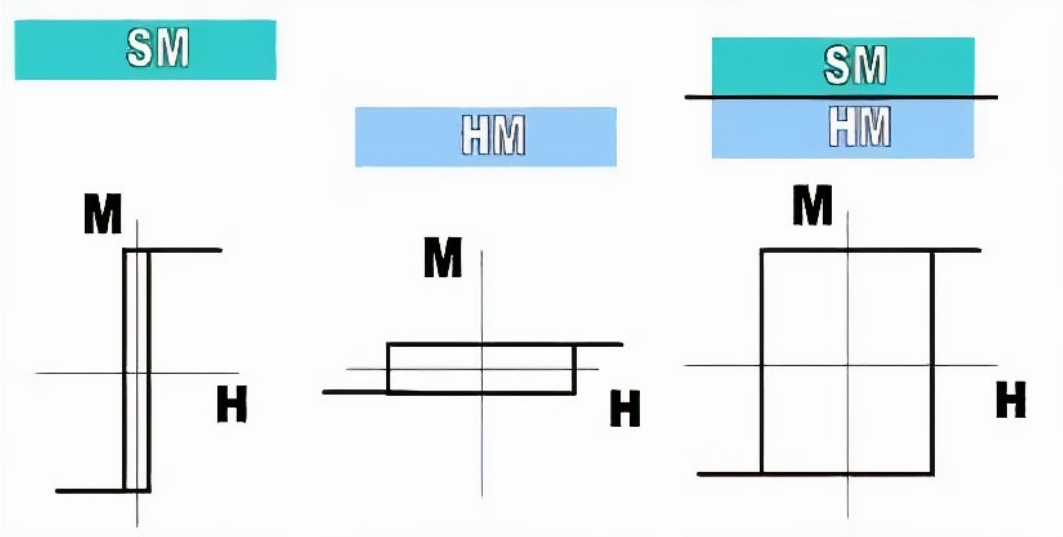

Fig. 1.9: Schematic hysteresis loops of a soft magnet, hard magnet and an exchange-coupled magnet [45].

In the exchange-coupling phenomena, the grains of the soft magnetic phase are pinned to the grains of the hard magnetic phase at their interfaces, while the centre of the soft phase can rotate in a reversed magnetic field (Figure 1.10). To achieve a complete exchange coupling between the hard and the soft magnetic phases, the grain size of the soft magnetic phase should not exceed twice the domain wall thickness of the hard phase. The critical exchange length (d_{cr}) can be described as $d_{cr} = \pi\sqrt{\frac{A_s}{K_H}}$ [42], where, A_s is the exchange stiffness of the soft magnetic phase and K_H is the magnetocrystalline anisotropy of the hard magnetic phase.

Since the discovery of the exchange coupling effect, many investigations have been done to produce hard/soft exchange-coupled magnets using various preparation techniques, including rapid quenching, melt spinning, mechanical alloying, and thin film

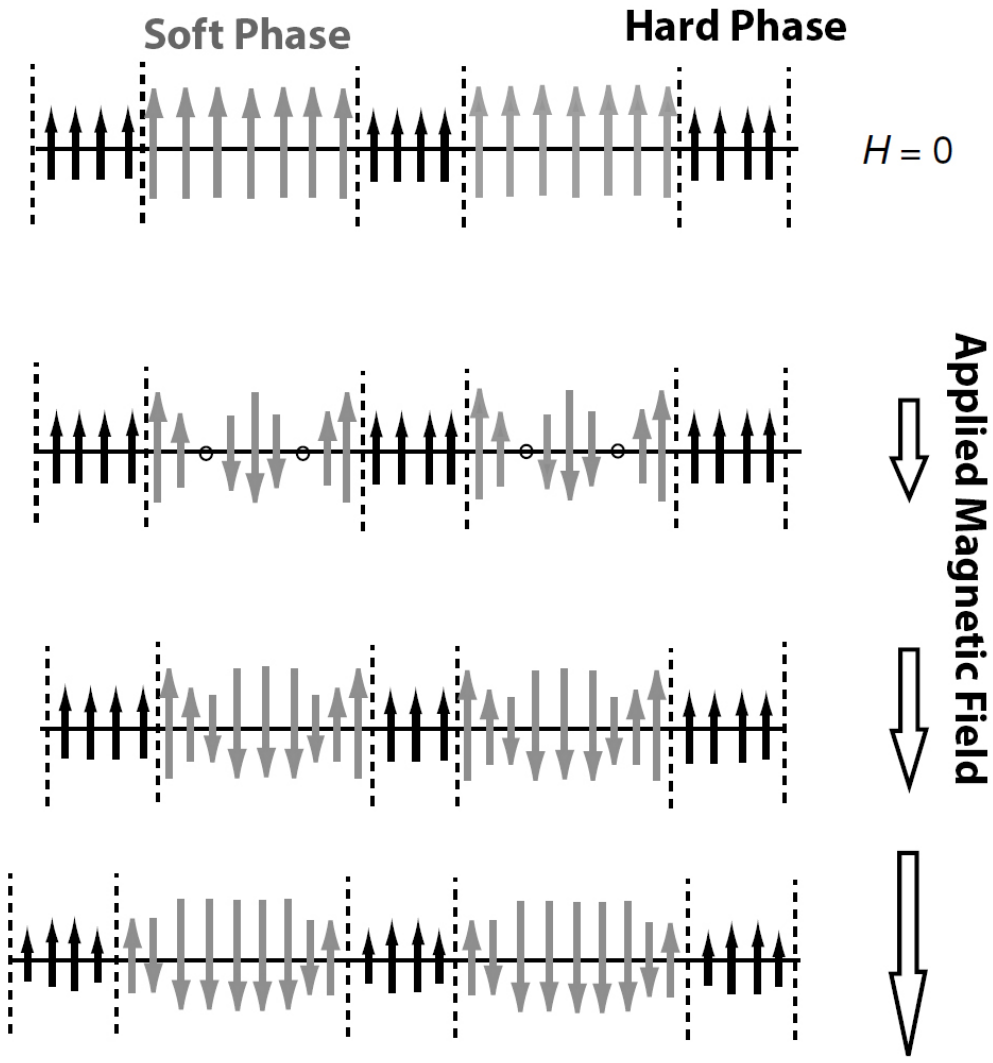

Fig. 1.10: Schematic of exchange-coupled Hard-Soft magnet [42].

deposition [24, 46–48]. The concept of producing exchange-coupled magnets opened new routes to provide permanent magnets with required properties by choosing proper soft and hard phases and by tuning the phase distribution. Since soft magnetic phases are mainly iron compounds, the exchange-coupled magnets become mostly cheap.

Bottom-up approaches, using magnetic nanoparticles, became the field of interest of many research groups to produce exchange-coupled nanocomposite magnets. However, the challenge for bulk nanostructured magnet synthesis is maintaining the homogeneous nanoscale morphology. Conventional compaction and condensation techniques lead to excessive grain growth. Recently, nontraditional approaches such as shock com-

paction [49], spark plasma sintering [50], and warm compaction [51] methods have been reported for producing dense bulk nanocomposite magnets with controlled grain size.

1.4 Motivation and Plan of Thesis

As described previously, Alnico magnets have low coercivities compared to the coercivity values up to 26 kOe (2069 kA/m) for Nd-Fe-B and Sm-Co rare-earth magnets. Yet, they present high saturation magnetisation and the highest energy product of rare-earth free permanent magnets. DC-sputtered Alnico V thin films on Si substrates showed unusually high H_c values $\sim$ 6 kOe (477 kA/m) [52], almost one order of magnitude higher than any of the known bulk samples. A strong dependency of magnetic properties on heat treatment was observed, but not understood. In 2012, films grown with different thicknesses and substrates [53] were shown to reach values of magnetic coercivity up to 10 kOe (796 kA/m), and Curie temperatures up to 300 °C. The unusually high coercivity value was suggested to be due to Si ions diffusing from the substrate to the thin film, leading to the formation of a novel body centred tetragonal (bct) Fe-Co-Si phase. Nonetheless, the diffusion mechanism, chemical composition and saturation magnetisation of this novel phase require further studies. In chapter 3 of this study, we investigate the effects of different heat treatment conditions on structural and magnetic properties of RF-sputtered Alnico V thin films on Si substrates. The work here presented led to the following publication:

[P1] F. Mohseni, A. Baghizadeh, A.A.C.S. Lourenço, M.J. Pereira, V.S. Amaral, J.M. Vieira, J.S. Amaral, *Interdiffusion Processes in High-Coercivity RF-Sputtered Alnico Thin Films on Si Substrates*, JOM. 69 (2017) 1427–1431. doi:10.1007/s11837-017-2382-y.

The published results of this chapter derived from a project entitled "Exploring Nano-fabrication Methods of High Coercivity Rare-earth Free Si-Alnico Permanent Magnets" led by Dr. J.S. Amaral. The Alnico V thin films were deposited by Prof. A.A.C.S. Lourenço, while some of the microscopy analyses were done with the assistance of Dr. A. Baghizadeh. The main tasks of the project, including sample preparation, heat treatments, magnetic, structural, chemical studies on the thin films, were

done by myself. The manuscript itself was mainly written by myself, benefiting from inputs, suggestions, and corrections from all co-authors.

In chapter 4, we investigate the exchange coupling behaviour on M-type ferrites, namely barium hexaferrite (BaM) and strontium hexaferrite (SrM.) Plate-like BaM and SrM nanoparticles were prepared by the sol-gel autocombustion method to achieve high aspect ratios and large surface areas of the nanoparticles. Spinel ferrites, of general chemical formula MFe_2O_4, where M is a divalent metallic ion or a combination of metallic ions, are also interesting due to their potential applications such as in magnetic devices, hyperthermia and drug delivery [54]. Among the soft spinel ferrites, Fe_3O_4 nanoparticles attracted the interest of many investigations for use as the soft magnetic phase in exchange-coupled magnets, due to their low cost, chemical stability, high M_s, and high T_C [55, 56]. These nanoparticles are typically synthesised using chemical methods, such as sol-gel, co-precipitation and hydrothermal methods. Organic-solvent-free hydrothermal methods for synthesising Fe_3O_4 nanoparticles are preferable due to their simplicity and good control of particle size [57]. This spinel ferrite was used as the soft magnetic phase in the ferrite based exchange coupled magnet. In this chapter, we explore correlation between the structural, compositional and microstructural changes and magnetic properties, of BaM/Fe_3O_4 and SrM/Fe_3O_4 nanocomposites.

Resin bonded magnets are among the most sold of the commercially available permanent magnets due to their low cost of preparation, lightweight structures and their low processing temperatures. They are produced from different types of polymers such as thermoplastic (e.g. polycarbonate, nylon, polyethylene) or thermoset materials (e.g. epoxy, phenolic or polyester resins), as the matrix mixed with a wide range of different hard magnetic powders [58–61]. These polymer matrix composite magnets exhibit interesting thermal, electrical, magnetic and mechanical properties [62–64]. To form complex geometries in a sintered permanent magnets, several manufacturing processes, such as cutting, machining and grinding are applied, which leads to the waste of magnetic materials and creates limitations for the geometric complexity of the final product [64]. On the other hand, bonded magnets can be fabricated in many shapes and sizes through injection moulding, extrusion moulding or compaction moulding processes. These low cost, complex shaped magnets find extensive applications, such

as flexible magnets, microwave absorbers and magnetic seals [65]. In chapter 5, we study the effects of compaction conditions, as well as the ferrite concentration in resin bonded exchange-coupled BaM/Fe_3O_4 and SrM/Fe_3O_4 composite magnets on their mechanical, magnetic and structural properties. The work on the exchange-coupled nanocomposites and resin bonded magnets has led to the following publications:

[P2] F. Mohseni, R.C. Pullar, J.M. Vieira, J.S. Amaral, *Enhancement of Maximum Energy Product in Exchange-Coupled $BaFe_{12}O_{19}/Fe_3O_4$ Core-Shell-Like Nanocomposites*, Journal of Alloys and Compounds 806 (2019) 120–126. doi:10.1016/j.jallcom.2019.07.162.

[P3] F. Mohseni, R.C. Pullar, J.M. Vieira, J.S. Amaral, *Bonded Ferrite-Based Exchange-Coupled Nanocomposite Magnet Produced by Warm Compaction*, Journal of Physics D: Applied Physics (2020) accepted manuscript. doi:10.1007/s11837-017-2382-y

The main idea of the published works of chapters 4 and 5 were mine benefiting from the collaboration with Dr. Rob Pullar and his expertise on the subject of ferrites synthesis techniques. The sample preparation, including exchange-coupled nanocomposite powders and warm pressed bulk magnets, heat treatments, magnetic, structural, chemical and mechanical studies were done by myself. The manuscript itself was mainly written by myself, benefiting from inputs, suggestions, and corrections from all co-authors.

To gain further understanding of the experimental results on the effect of thickness of the flake-like BaM nanoparticles on their magnetic properties on their magnetic properties and to optimise the phase balance of the exchange-coupled BaM/Fe_3O_4 hard-soft magnetic nanocomposites, micromagnetic simulations were performed and are presented in chapter 6. Simulations were performed using the MuMax^3 software, exploring the recent possibility of simulating 3D grains in modelling the superparamagnetic-like behaviour of the magnetite nanoparticles of the system and comparing to continuous film models. Relatively large size models of the nanocomposites (micrometer sized) with various phase fractions were simulated and the achieved magnetic hysteresis curves were compared to the experimental results. We show how phase balance and distribution affect exchange-coupling behaviour which ultimately govern the hard magnetic

properties of the nanocomposites.

The work in this chapter, particularly in its initial studies, greatly benefited from the collaboration with Dr. A. Hierro-Rodriguez and his expertise in the field of micromagnetic simulations. The model preparation and simulations were done by myself. The work here presented is aimed at a future submission as scientific publication.

Chapter 2

Experimental Techniques

2.1 Sample Preparation

2.1.1 Alnico V Thin Films

2.1.1.1 Principles of Magnetron Sputtering

Magnetron Sputtering is a physical vapour deposition (PVD) technique in which high-quality thin films can be prepared from materials such as metals, insulators, semiconductors, alloys, metal oxides, nitrides, and carbides. In a sputtering system, two electrodes are used inside a vacuum chamber ($<10^{-8}$ Bar), the target is the cathode and the substrate is the anode. The inert gas (usually argon gas) is then introduced in the chamber and electric potential is applied between electrodes. During the process, the target is bombarded with high-energy positively charged inert gas ions. When the kinetic energy of the bombarded ions exceeds the thermal energy of the atomic bonds of the target material, atoms of the target surface are ejected, or "sputtered" and can be deposited as a thin film on the surface of a substrate [66–69]. During the ion bombardment, secondary electrons are emitted from the target surface which maintain the plasma on the target. In the magnetron sputtering setup, the magnetic field is situated parallel to the target surface and restrains the secondary electron motion to the proximity of the target. As a result of this, a dense plasma is formed which leads to an increased ion bombardment, higher deposition rate and of lower Ar pressure ($\sim 10^{-3}$ mbar compared to 10^{-2} mbar in basic sputtering) [67]. Figure 2.1 shows the schematic

diagram of a sputtering setup.

Depending on the process of formation of ions, magnetron sputtering is divided into direct current (DC) magnetron sputtering and radio frequency (RF) magnetron sputtering. In the DC sputtering setup, a high DC voltage is connected to the electrodes (high negative voltage to the target and positive or ground to the substrate). In this setup, the target materials must be electrically conductive. Therefore, DC sputtering is mostly used for metal deposition. For insulating targets, the positive charge accumulates on the target and the sputtering rates gradually decrease. In order to solve this problem, a RF sputtering setup with a high-frequency alternating current (AC) can be applied between cathode and anode to sustain the ion production [68, 69].

To synthesize thin film alloys via a sputtering method, the most common practice is to simply deposit the alloy from a homogeneous alloy target or to apply co-deposition from multiple targets. The use of multiple targets is also useful to prepare nanostructured composite thin films and/or exploring different compositions [66].

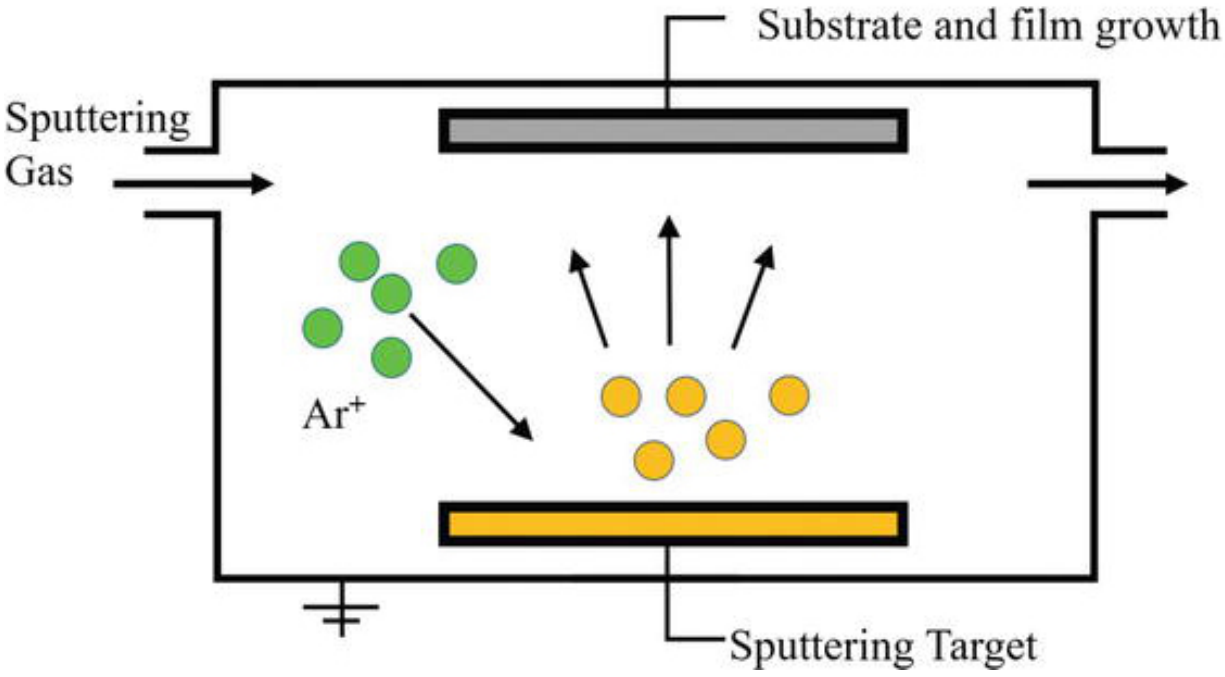

Fig. 2.1: Schematic diagram of sputtering [67].

2.1.1.2 Synthesis of Alnico V Thin Films

Thin film samples of 100 nm thick Alnico V were prepared at different deposition temperatures, ranging from room temperature to 550 °C via a RF sputtering setup at the Physics department of the University of Aveiro, at the CICFANO building. The $\sim$ 0.7 mm thick sputtering targets were made of commercial pure Alnico V alloy and silver with the percentage of total contamination below 0.1 %. Substrates were of 700 μm thick Si(100) single crystal. In order to investigate the effect of the SiO_2 layer on top of the Si substrates, thin films were deposited on substrates with and without a SiO_2 layer. The removal of this SiO_2 layer was performed using a solution of 0.75 ml fluoric acid with 9 ml deionised water and 1 ml of methanol for 120 s in an ultrasonic bath. The RF-sputtering chamber was first evacuated to 4×10^{-10} Bar and then filled with 99.9999 % pure Ar for the deposition with the pressure of 7×10^{-6} Bar. Figure 2.2 shows the RF sputtering setup used to prepare the thin films. In order to prevent surface oxidation during post annealing treatments, the surface of the thin film samples was coated with a thin silver layer of a few nanometres. Samples were then sealed in a quartz tube containing Ar with the pressure of 300 mbar and 1.2 bar and annealed at 600 °C, 800 °C and 900 °C for 60 minutes followed by quenching or slow cooling.

2.1.2 BaM-SrM / Fe_3O_4 Nanocomposite Powder

In order to prepare BaM/Fe_3O_4 or SrM/Fe_3O_4 nanocomposite powders, flake-like BaM and SrM nanoparticles were first prepared via a sol-gel autocombustion method, followed by an optimised annealing process to form single-phased M-type hexaferrite. The prepared powders were then mixed with a solution of Fe^{3+}/Fe^{2+} 2:1 dissolved in deionised water and magnetite nanoparticles were nucleated and grown on the surface of hexaferrite powders via a hydrothermal or coprecipitation method to form the nanocomposite powder.

For this process, Strontium nitrate ($Sr(NO_3)_2$), Barium nitrate ($Ba(NO_3)_2$), Iron nitrate ($Fe(NO_3)_3 \cdot 9H_2O$) and Ammonia 25 wt.% solution were purchased from Chem-Lab NV. Iron(III) chloride hexahydrate ($FeCl_3 \cdot 6H_2O$), Iron(II) lactate hydrate (dried material) ($Fe(lac) \cdot xH_2O$), Citric acid monohydrate ($C_6H_8O_7 \cdot H_2O$) and Sodium

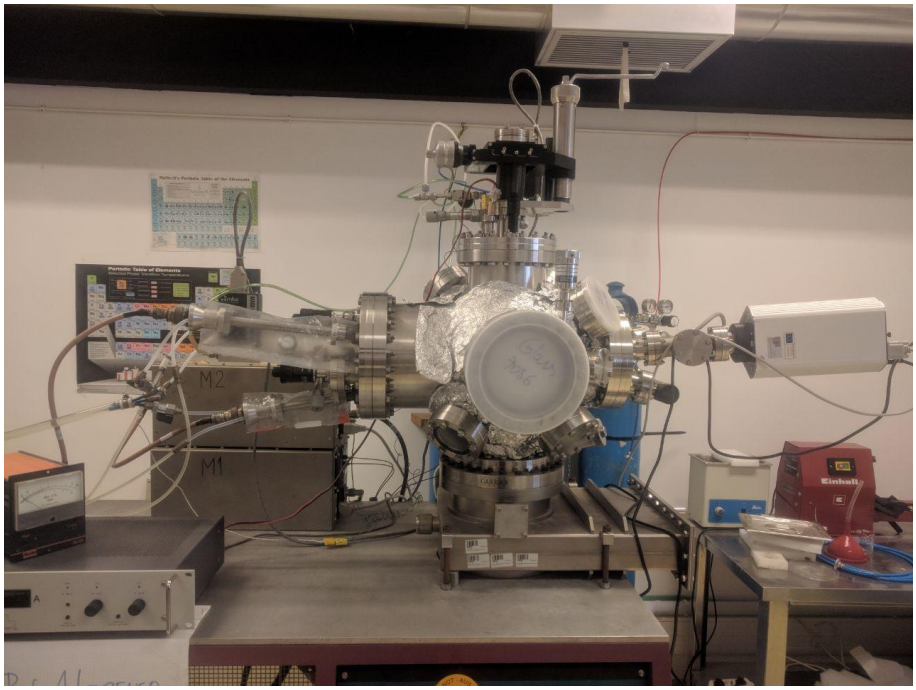

Fig. 2.2: RF sputtering setup used to prepare samples of Alnico V thin film.

hydroxide (NaOH) pellets were purchased from Sigma-Aldrich. All the reagents used in this study were of analytical purity.

2.1.2.1 Sol-gel Autocombustion Synthesis of Barium/Strontium Hexaferrite Powders

In the sol-gel auto-combustion method, flake-like particles of the hexaferrite were produced via the exothermic reaction of a xerogel. A stoichiometric solution of metal nitrates $Ba(NO_3)_2$ or $Sr(NO_3)_2$ and $Fe(NO_3)_3 \cdot 9H_2O$ in distilled water was prepared, and then citric acid was added to the mixture with a molar ratio of 1:1. The nitrate salts are more desirable in the sol-gel auto-combustion method, due to their ability to dissolve in water at low temperatures. A 25% ammonia solution was then added dropwise to the solution to adjust the pH to 7. The mixture was then dried at 80 °C in an oven for 4 days. The dried xerogel was then heated up on a hotplate to a temperature of 320 °C to initiate the combustion process. The rapid exothermic evolution of CO_2 gas during the large mass loss of the organic fuel from the xerogel during combustion generates the barium or strontium containing nanopowders (Figure 2.3). These powders were then calcined at 600 °C, 900 °C and 1000 °C for 1-5 hours in order

to achieve single-phased M-type hexaferrite.

Fig. 2.3: Exothermic reaction during sol-gel autocombustion method.

2.1.2.2 Synthesis of Fe_3O_4 Nanoparticles

In the hydrothermal method, 4 mmol of ferric chloride and 2 mmol of ferrous lactate were used as ferric and ferrous ion sources. The molar ratio of ferric to ferrous ions was kept at 2. The reagents were then dissolved in 80 ml of deionised water and aged for 10 *min*. Calcined single phase BaM or SrM nanoparticles were then mixed with the ferrous/ferric solution. 40 ml of 1.0 kmol/m^3 sodium hydroxide solution was added dropwise into the solution at the rate of 3.0 ml/min under vigorous stirring, using a magnetic stirrer, in an argon atmosphere to precipitate magnetite nanoparticles on the calcined M-type hexaferrite nanoparticles. In the hydrothermal method, the mixture was transferred to an autoclave, sealed and then heated in an oven at 120 °C for 20 h (Figure 2.4(a)) and for the coprecipitation method, the mixture was heated up and kept at 70 °C for 1 h under stirring in an argon atmosphere (Figure 2.4(b)). The achieved nanoparticles, from both methods, were then washed with deionised water 3 times and collected by centrifugation at 3000 rpm, and dried at 40 °C for 10 h.

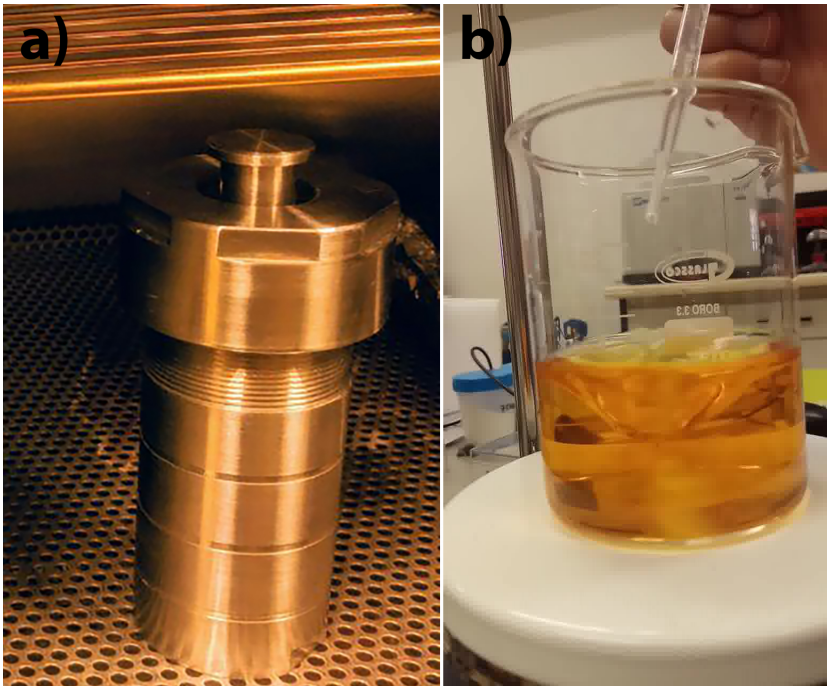

Fig. 2.4: Hydrothermal and coprecipitation synthesizing methods of Fe_3O_4 nanoparticles.

2.1.3 Ferrite Based Exchange-Coupled Bonded Magnets

In order to prepare bulk bonded permanent magnet composites, a thermoset epoxy resin powder was used as the matrix and the exchange-coupled ferrite based nanocomposites of BaM or SrM nanoparticles coated with magnetite nanoparticles, were used as the filler. The 72-PON Epoxy resin powder was purchased form CIN with a median particle size of 60 μm and the curing procedure of 10 *min* at 180 °C. The ferrite powders with 80 wt.%, 85 wt.%, 90 wt.% and 95 wt.% were mixed with the epoxy resin powder in a Turbula 3D shaker mixer for 30 minutes to homogenise the mixture. The mixed powders were then warm pressed in a 10 mm diameter cylindrical shaped die, heated at 180 °C for 10 *min* under 300 MPa, 500 MPa and 700 MPa of pressure. During the warm compaction process, the epoxy resin bonds the magnetic powders and cures. Figure 2.5 shows the warm compaction setup and the cylindrical form of the bonded magnet sample.

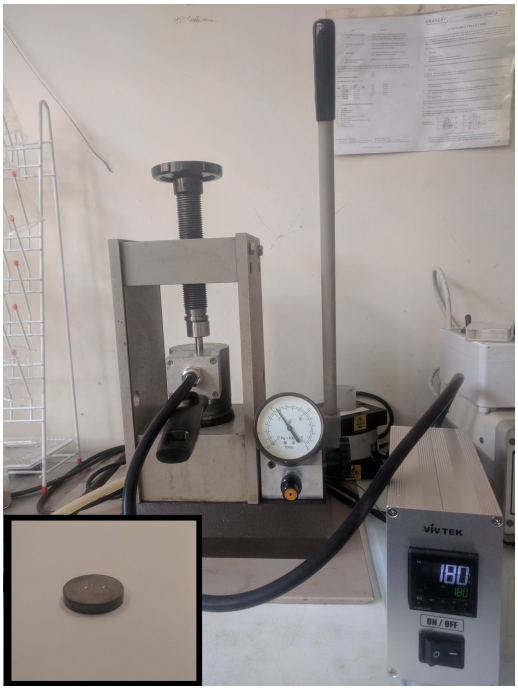

Fig. 2.5: Warm compaction setup and the form bonded magnet sample.

2.2 Characterisation Techniques

2.2.1 X-ray Analysis

2.2.1.1 X-ray Diffraction

X-ray diffraction (XRD) is a non destructive material characterisation technique which is widely used for analysing the crystalline structure of materials. When an X-ray beam with a given wavelength (λ) interacts with a material, the matter either absorbs the x-ray beam or scatters it in elastic and nonelastic ways. In the elastic scattering, the scattered beam conserved energy and its wavelength λ [70–72].

Bragg's law can be expressed as:

$$\lambda = 2d\sin(\theta), \tag{2.1}$$

where λ is the wavelength of the incident X-ray, d is the distance between the lattice planes and θ is the incident glancing angle. Each lattice plane is generally indexed by Miller indices (hkl). In an X-ray powder diffraction experiment, peaks are generated from randomly distributed orientations in different grains. The intensity of peaks from

each plane (I_{hkl}), obtained from the number of photons counted in the XRD detector, is related to their structural factor (F_{hkl}):

$$I_{hkl} \propto |F_{hkl}|^2 \tag{2.2}$$

All planes with identical d-spacing (e.g. (111), (1-1-1), (-1-1-1), etc.) contribute to the same diffraction intensity [72]. X-ray powder diffraction can also be used to calculate the average crystallite size (τ) using Scherrer equation:

$$\tau = \frac{K\lambda}{\beta \cos\theta}, \tag{2.3}$$

where K is a dimensionless shape factor depending on the geometry of the crystallites (~ 0.9 for spherical crystallites) and β is the full width half maximum (FWHM) of the diffraction peaks [72].

In this study, the characterisation of the crystalline structure of the synthesised nanoparticles was performed with Cu Kα radiation ($\lambda = 1.5406$ Å) over a range of $2\theta = (20° < 2\theta < 80°)$ using a Rigaku Geigerflex XRD diffractometer. X'pert software was used for preliminary detection of the phases and Rietveld refinement was performed using FullProf.

2.2.1.2 X-ray Reflectivity

Due to the high frequency of Cu Kα radiation (in the order of 10^{19} Hz), which is ~ 4 orders of magnitude larger than the eigenfrequency of an electron bound to a nucleus of an atom, the interaction of X-ray radiation with matter can be described by the index of refraction. The index of refraction can characterise the change of direction of the X-ray beam when passing from air to the material [73–75]. The complex index of refraction for X-ray radiation (n) can be written in the following way:

$$n = 1 - \delta - i\beta \tag{2.4}$$

$$\delta = \frac{\lambda^2}{2\pi} r_e \rho_e \tag{2.5}$$

$$\beta = \frac{\lambda}{4\pi}\mu_x, \tag{2.6}$$

where δ is the scattering index, β is the absorption index of the material, ρ_e is the electron density of the material, r_e is the classical electron radius ($r_e = 2.818 \times 10^{-15}$ m^{-1}) and μ_x is the absorption coefficient of the material [74].

When the X-ray radiation passes from air, with the refractive index of 1, to a material, with n < 1, the beam can be totally reflected, if the incident angle is smaller than a critical angle (θ_c),

$$\cos\theta_c = n = 1 - \delta \tag{2.7}$$

Since the refractive index in X-ray is very close to 1, θ_c is very small with an approximation:

$$\theta_c^2 = 2\delta \tag{2.8}$$

$$\delta \sim 10^{-5} - 10^{-6} \tag{2.9}$$

$$\theta_c \sim 0.1^\circ - 0.5^\circ \tag{2.10}$$

The reflectivity is described as:

$$\text{Reflectivity } R = \frac{\text{Intensity of the reflected beam}}{\text{Intensity of the primary beam}} \tag{2.11}$$

For $\theta > \theta_c$, a part of the incident beam refracts into the material [74, 75]. This phenomenon is the basis of determining the thickness of thin films on a substrate (Figure 2.6). According to Snell's law:

$$n_1 \cos\theta_1 = n_2 \cos\theta_2 \tag{2.12}$$

$$\cos\theta_2 = \frac{\cos\theta_1}{1 - \delta} \tag{2.13}$$

When θ_1, θ_2 and $\delta << 1$, then:

$$\theta_2 \approx \sqrt{\theta_1^2 - 2\delta} \tag{2.14}$$

For thin film samples a constructive interference occurs when:

$$2t \sin\theta_2 \approx 2t\sqrt{\theta_1^2 - 2\delta} = n\lambda \tag{2.15}$$

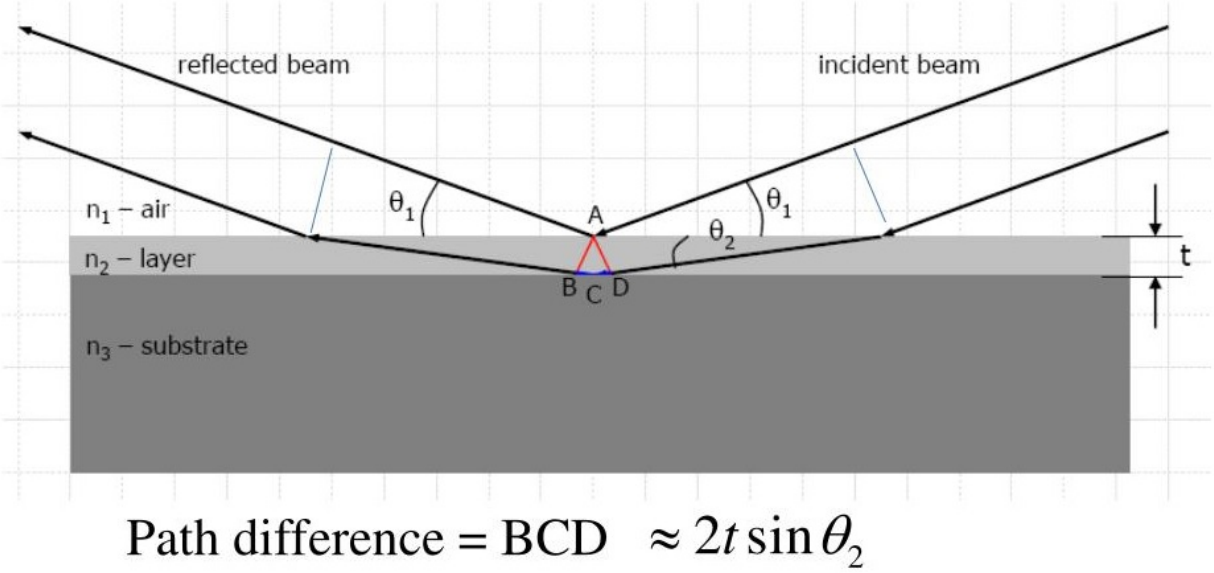

Fig. 2.6: X-ray reflectivity from thin films [76].

As a result, the reflectivity shows oscillations, the Kiessig fringes. The period of fringes is inversely related to the thickness of the film, thinner films showing larger distances between fringes. The amplitude of the fringes is related to the electron density of the material. The surface roughness also affects the reflectivity intensity, the rougher the surface the faster is the intensity decreased [74, 75]. To optimise the deposition rate in the RF sputtering of the Alnico V thin films, X-ray reflectivity measurements were performed on the initial samples, using a Philips Panalytical X'Pert Pro MRD and X'pert Epitaxy software were used to calculate the thickness of the deposited samples. Figure 2.7 shows a result of X-ray reflectivity measurements on one of the Alnico V thin film samples.

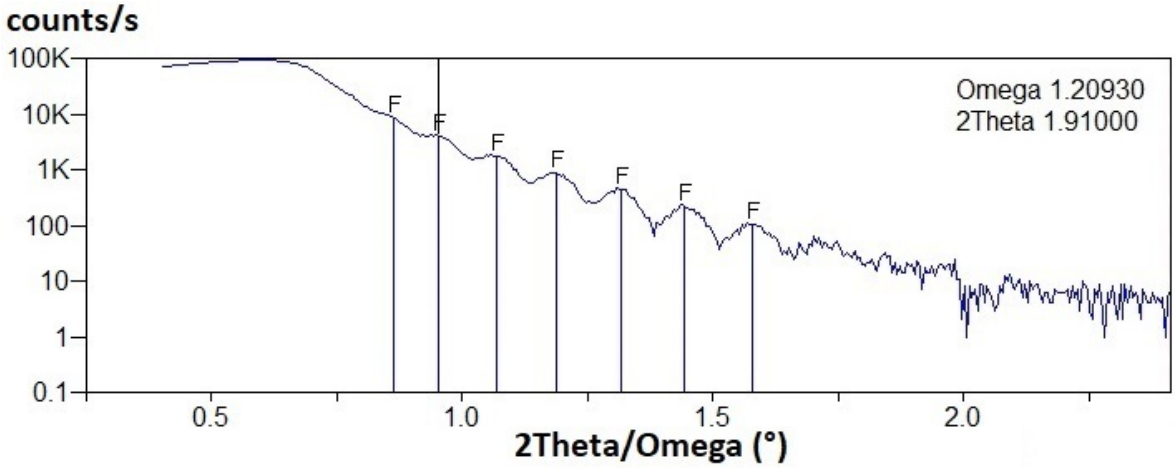

Fig. 2.7: X-ray reflectivity pattern of Alnico V thin film sample deposited for 30 *min* at room temperature.

2.2.2 Electron Microscopy

2.2.2.1 Scanning Electron Microscopy

Scanning electron microscopy (SEM) is a versatile characterisation technique which is employed to analyse the surfaces of materials. In a SEM, the specimen is hit by a high energy electron beam and the outcoming electrons and X-rays are obtained for different analyses. Through the analysis of the outcoming electrons and X-rays, several useful information about the morphology, topography and composition of the specimen can be obtained. The high-quality and detailed image obtained from an SEM can have a spatial resolution of a few nanometres and the magnification can extend up to a few hundred thousand times. The specimen for SEM has to be electrically conductive to avoid the overcharging effect on the surface, which can introduce extreme brightness in the produced image. Therefore, the non-electrically conductive samples are usually coated with a very thin layer of graphite or gold-platinum alloy in a sputtering machine [77, 78].

In a SEM the primary electrons, produced by an electron gun, hit the sample and release secondary electrons (SE) from the specimen surface which then can be collected by a detector to form the image. The ejected electrons from the specimen (SEs) usually have low energy (less than 50 eV) and create vacancies in the specimen's inner shell electrons. The vacancies are then filled with higher level orbital, which then

produces an X-ray characteristic of that energy transition. Energy-Dispersive X-ray Spectroscopy (EDS) is an elemental analysis technique that can take advantage of these emitted X-ray photons for chemical characterisation of the specimen.

In this study, the morphological and compositional characterisations of synthesized nanoparticles and bulk bonded magnets were carried out on a Hitachi S-4100 SEM equipped with EDS operated at 25 kV.

2.2.2.2 Transmission Electron Microscopy

Electron microscopes take advantage of high energy electron beams (20-300 kV) and thus produce accelerated electrons with a very short wavelength (0.859-0.037 Å) compared to the wavelengths used in the optical microscopes (2000-7500 Å). Electron microscopes are then able to produce high resolution images which make it possible to analyse very small features in the specimen [77]. Transmission electron microscopes (TEM) operate at much higher voltages compared to a SEM, which leads to a much higher resolution in the produced images. Unlike SEMs, which analyses the surface of the specimen in the scanning mode, TEM detects the transmitted electron beam, which leads to an in depth analysis of the specimen. In a TEM, several detailed analyses, such as structural, morphological, crystallographic, can be performed. In order to achieve TEM images, the specimen has to be transparent to the electron beam. Therefore, a critical sample preparation is needed to thin down the specimen to thicknesses below 50 nm. For bulk and thin film samples, a precise mechanical or chemical polishing followed by an ion milling, and for powder samples an ultrasonication of the powder is required.

The wavelength of the high energy electrons in the TEM is much smaller than the atomic space in a crystalline structure of a specimen. Therefore, the electron beam diffracts. In a TEM setup, the electron beam can be concentrated on a specific region and by inserting the selected area aperture instead of the objective aperture, the diffraction pattern of that specific region can be produced, which is called selected area electron diffraction (SAED). Similar to the XRD technique, SAED can be used to analyse crystal structures of the specimen but on a specific region of the specimen [79, 80].

A scanning transmission electron microscope (STEM) takes advantage of the strength of both SEM and TEM. The micrograph obtained from a STEM is a result of the scanning of the specimen with a condensed electron beam in a transmission mode. Like TEM, the specimen in the STEM has to be transparent to the electron beam. The advantage of a STEM over a TEM is that it can analyse other signals, such as SEs and elastically scattered beam electrons, which cannot be obtained by a TEM. In STEM, the elastically scattered beam electrons, from the elastic interaction between the electron beam and the nuclei of sample atoms, can be detected using a high angle annular dark field (HAADF) detector. HAADF images are dark field (DF) images which shows the contrast in the compositional differences in a multiphase sample, which can give important information about the analysed sample. In both TEM and STEM the characteristic X-rays can be collected with an X-ray detector for compositional studies. However, STEMs can produce EDS mappings and line scans due to their scanning mode, which leads a detailed and in depth compositional analysis of the sample [81].

In this study, a Hitachi H-9000 TEM operated at 300 kV and a JEOL 2200FS TEM operated at 200 kV and a Hitachi HD-2700 STEM operated at 200 kV, all equipped with EDS, were applied for the structural characterisation and composition analysis of the synthesized nanoparticles of the ferrites as well as Alnico V thin film samples.

2.2.3 Superconducting Quantum Interference Device

The Josephson junction consists of two superconducting (S) electrodes separated by a thin insulating (I) or normal conducting (N) layer. In the SIS junction, the two superconducting electrodes are weakly joint by a thin insulating layer. It is known that the current transport occurs by tunnelling of Cooper pairs through the insulating part without any voltage drop and only causes a phase difference δ in the macroscopic wave functions of the two superconducting electrodes. The supercurrent (I_s) across the junction can be expressed as:

$$I_s = I_0 \sin \delta, \tag{2.16}$$

where I_0 is the critical current (maximum supercurrent). A superconducting quantum interference device (SQUID) is an extremely sensitive magnetometer device which operates on the basis of Josephson junctions. The SQUID magnetometers can operate in DC mode (DC SQUID) or AC mode (RF SQUID). Due to the lower intrinsic flux noise in the DC SQUIDs compared to RF SQUIDs, the DC SQUIDs have more sensitivity.

Figure 2.8 shows a schematic of a DC SQUID. The setup consists of a superconducting loop with a bias current (I) which is divided into I_1 and I_2. An external magnetic field ($H = B/\mu_0$) is applied to the ring and two Josephson junctions are incorporated to the arms which limit the critical current I_C resulted from the critical current of each junction (I_{C1} and I_{C2}). It is known that the flux enclosed in a superconducting loop is quantised into units of flux quantum, described as:

$$\Phi_0 = \frac{h}{2e} \approx 2.07 \times 10^{-15}\text{Wb}, \tag{2.17}$$

where h is the Planck's constant and e is the electronic charge.

First, the magnetic flux, enclosed inside the superconducting ring, modulates the I_C in the ring periodically, with a period of Φ_0, which is caused by the interference of the two wave functions in the two sections of the ring with phases difference of $\Delta\delta$. Then a slightly higher bias current ($I > I_C$) is applied to the ring, which makes it possible to measure the voltage across the junctions directly as a function of the external magnetic field. When I_C reaches its maximum V is minimum and vice versa [82].

In this study, magnetic measurements were performed using a Quantum Design MPMS3 SQUID magnetometer with a maximum field of 7 T, with the advantage of performing the measurements in DC or vibrating sample magnetometer (VSM) modes. However, the accuracy of the measured magnetic moments values in this type of magnetometer is affected by the geometry and the radial offset of the sample, which requires post measurements corrections [84]. The data correction can be performed by the simulation software provided by Quantum Design for both VSM and DC measurements. However, the software needs accurate measurements of sample geometry and radial offset which in most cases, such as powder samples, can be difficult to obtain. In order to overcome this problem, we used a simple method which solely needs a VSM and

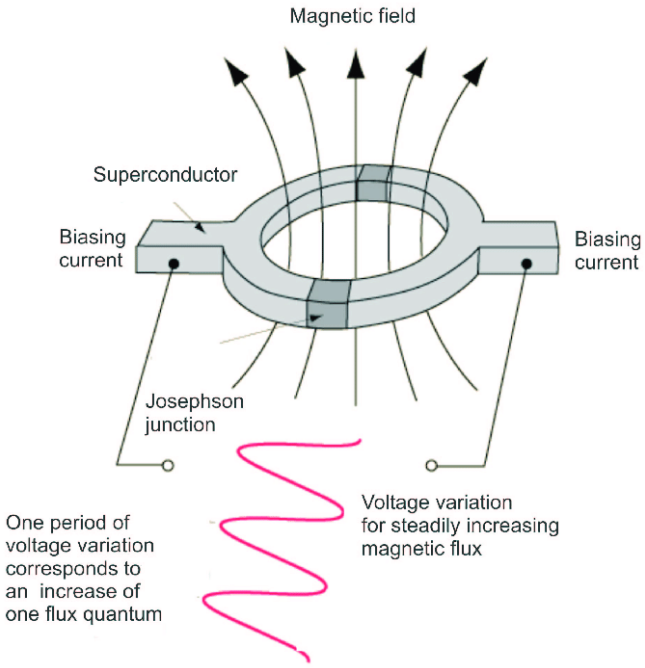

Fig. 2.8: Principle of SQUID magnetometer [83].

a DC measurement at a given external magnetic field. We have found that there is a unique function of correction ($\alpha(x)$), independent of the sample's geometry and/or radial offset, which is a function of the DC scan length and the VSM amplitude [P4]. This correction method can be described as:

$$x = \frac{(M_{VSM} - M_{DC})}{M_{VSM}} \tag{2.18}$$

$$M_{real} = \frac{M_{VSM}}{\alpha(x)}, \tag{2.19}$$

where M_{VSM} and M_{DC} are the magnetic moments measured in the VSM and DC modes and M_{real} is the corrected value of the magnetic moment. By doing a single measurement in both VSM and DC modes for the sample, the measured magnetisation can then be normalized to the corrected values. All magnetic measurements performed in powdered and composite samples in this thesis have been corrected by this method.

2.2.4 Atomic Force Microscopy

Atomic Force Microscope (AFM) is a type of scanning probe microscope in which the surface topographical image, with sub-nanometer accuracy, of a specimen can be achieved. During the scan, a sharp probe runs across the sample surface and moved vertically by a feedback close loop to maintain a constant interaction with the sample. These vertical movements are recorded against XY position of the probe to produce the final surface topography. These XYZ nano positionings are achieved by piezoelectric scanners working in voltages in the range of hundreds of volts. The AFM probes consist of a sharp tip, with a radius ranges from a few nm to 30 nm, and a micro cantilever. The cantilever detects the probe-sample interaction. To measure the bending or twisting of the cantilever, a laser diode is focused onto the end of the cantilever and reflected from the cantilever to a position sensitive photodiode (PSPD). When the cantilever bends or tilts, the direction of the reflected laser beam changes and can be detected on the PSPD [85].

AFMs have several modes of operation, such as contact mode, tapping mode and non contact mode. In the contact mode, the tip moves around the surface of the sample with a constant force and directly scans the surface. When the probe scans across recessed and protruding feature, the cantilever is lowered and pushed up to eliminate the deflection errors. In the tapping mode the probe oscillates nearby its resonance frequency on the surface of the samples and taps the surface. This mode is used to eliminate the frictional forces for less destructive measurements. In the non contact mode, the probe oscillates above the surface. The topography image is produces with the changes in the amplitude of the oscillation due to the van der Waals forces. The non contact mode is used as a non destructive technique mostly for soft samples [85].

In this study, the surface quality of the Alnico V thin films after deposition and the surface roughness after different heat treatments were analysed using a Park XE7 AFM.

2.2.5 Hardness Testing

The hardness test provides qualitative relationships to other mechanical and physical properties such as rigidity, strength and density. However, several publications reported the relationship between hardness and ultimate tensile strength (UTS) of materials [86]. The ASM handbook [87] shows that there is a fairly good relationship between the hardness and metallic alloys over a wide range of strength:

$$HV \approx 3 \times \sigma_{UTS}, \tag{2.20}$$

where HV (expressed in kgf/mm^2) is the Vickers hardness and σ_{UTS} (expressed in MPa) is the UTS of materials.

The basic principle of a hardness test is to form an indentation on the surface of a specimen and measure the ability of the material to resist plastic deformation. Vickers hardness (HV), first developed in 1921, uses a 136° pyramidal diamond indenter to form a square shaped mark (Figure 2.9). In order to cover all testing requirements, the Vickers test can be performed in the force range of micro (10 g to 1000 g) and macro (1 kg to 100 kg). Vickers values are considered test force independent, which means that changing the force does not affect the Vickers hardness values. In order to have a reliable measurement, the difference between the diagonals of the indentation marks (d) should not exceed $\sim$ 5 %. The area of the indentation can be calculated as:

$$A = \frac{(d_1 + d_2)^2}{2 \sin(136°/2)} \tag{2.21}$$

Therefore, the Vickers hardness is:

$$HV = \frac{F}{A} \approx 1.8544 \frac{F}{(d_1 + d_2)^2} \left(kgf/mm^2\right), \tag{2.22}$$

where F is the applied force [88]. The Vickers hardness number is then reported such as 90HV2, where 90 is the hardness number and 2 is the applied load in kgf. In this study, Vickers hardness tests were performed with a Wilson Hardness VH 1102 using 2 kgf.

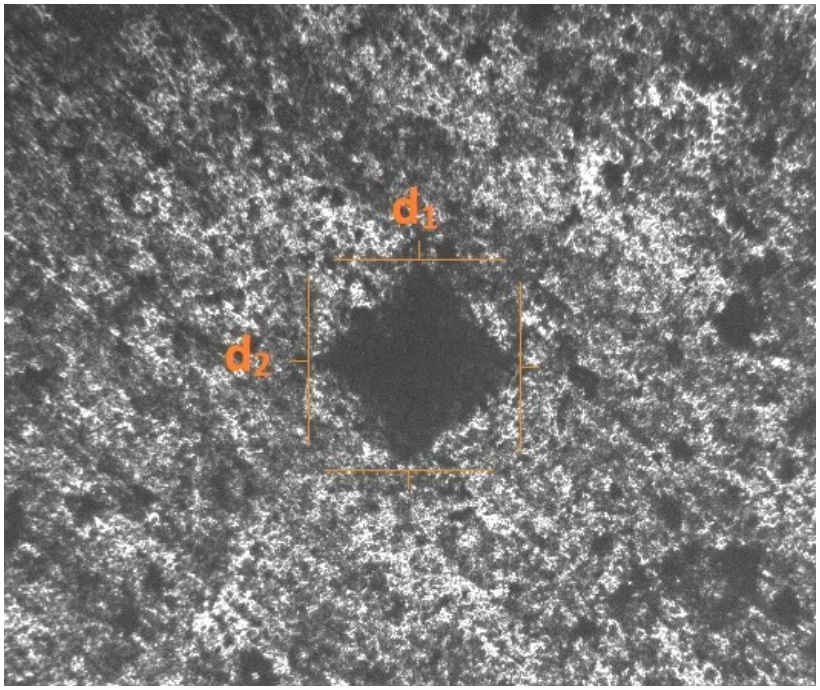

Fig. 2.9: Indentation of Vickers hardness test on the bonded magnets.

2.2.6 Density Measurements

Archimedes' principle states that a fully or partially immersed body in a fluid experiences a buoyant force acting vertically upwards on it and is equal to the weight of the fluid displaced by the body. Using this principle aids to determine the density of materials as such:

$$\rho = \frac{W_a}{W_a - W_l}\rho_l, \tag{2.23}$$

where ρ is the density of the specimen, W_a is the weight of the specimen immersed in air, W_l is the weight of the specimen in the aid liquid and ρ_l is the density of the aid liquid. In the density calculations, the temperature of the liquid must also be considered. The difference of 0.1 °C in the temperature can cause density changes in the third decimal. In this study, an ADAM ADP-110 density determination set was applied to the density measurements. The aid liquid was an analytical reagent grade 99.99 % pure ethanol with a density of $\sim$ 785 kg/m^3 at 25 °C. In order to achieve a more precise measurement, at least 3 different measurements were performed on each sample [89].

Chapter 3

High Coercivity Alnico V Thin Films

Developed in 1931, Alnico alloys were the first advanced hard magnetic materials, and are mainly composed of iron and cobalt, with about 30 % of Al, Ni, Cu, and Ti in some of its forms. They are hard ferromagnets with high magnetisation and Curie temperatures above 400 °C due to a spinodal decomposition of the alloy into two Body Centred Cubic (bcc) phases of elongated Fe-Co rich rod participates ($\alpha 1$) in an Al-Ni rich matrix ($\alpha 2$) [1]. Their main drawback in applications is their relatively low intrinsic coercive field, below 700 Oe (56 kA/m) for the most popular Alnico V, up to 1500 Oe (120 kA/m) for optimised Alnico 8 compositions, which poorly compares to the values up to 26 kOe (2000 kA/m) for Nd-Fe-B and Sm-Co rare-earth magnets. Yet, they present the highest energy product of rare-earth free permanent magnets, at $\sim$ 10 MG.Oe ($\sim$ 80 kJ/m^3) [28].

In 2010, DC-sputtered Alnico V thin films on Si substrates showed unusually high H_c values $\sim$ 6 kOe (480 kA/m) [52], almost one order of magnitude higher than any known bulk samples. A strong dependency of magnetic properties on heat treatment was found, but remained unexplained. In 2012, films grown in different thicknesses and on different substrates [53] were shown to reach values of magnetic coercivity up to 10 kOe (800 kA/m), and Curie temperatures up to 300 °C. The unusually high coercivity value was suggested to be due to Si ions diffusing from the substrate to the thin film, leading to the formation of a novel Body Centred Tetragonal (bct) Fe-Co-Si phase.

Samples with thicknesses above 100 nm showed reduced coercivity, most likely due to the diffusion length of Si and quenching of thin film samples becoming essential to form the metastable phase. Nonetheless, the diffusion mechanism, chemical composition and saturation magnetisation of this novel phase require further studies.

In this chapter, we study the effects of different heat treatment conditions on structural and magnetic properties of RF-sputtered Alnico V thin films on Si substrates. The chapter is organised as follows: in Sec. 3.1, Alnico V preparation procedure and characterisation used to optimise the deposition rate are explained; in Sec. 3.2 the results of magnetic measurements performed on the thin film samples are presented; in Sec. 3.3, the structural studies to investigate the origin of high coercivity in Alnico thin films are presented in detail. Finally, in Sec. 3.4, as a summary, an overall discussion of the results is provided.

3.1 RF-Sputtering of Alnico V Thin Films

In order to optimise the deposition rate of the Alnico V thin films, two sets of Alnico V thin films on Si substrate were prepared using the same deposition power (20 W) with different deposition times. Figure 3.1 shows the X-ray reflectivity patterns of the Alnico V thin film samples deposited for 10 min and 30 min. The distance between the fringes corresponds to the thickness of the thin films. The measurements show that the thin films deposited for 10 min and 30 min have a thickness of $\sim$ 20 nm and $\sim$ 50 nm, respectively.

In order to study the diffusion mechanism of Si into Alnico thin films, as well as the effect of different preparation conditions on the magnetic properties of the Alnico samples, several Alnico V thin film samples deposited at different temperatures and with or without the natural SiO_2 layer were prepared. A few nanometres thick silver layer was applied on the Alnico thin films to prevent the oxidation of the thin film. Figure 3.2 shows illustrations of the thin film samples prepared for this study. In order to study the diffusion of Si atoms, a silver buffer layer was deposited on the Si substrate before depositing the Alnico V thin films in some samples to prevent the diffusion of Si atoms from the substrate to the thin film (Figure 3.2(c)).

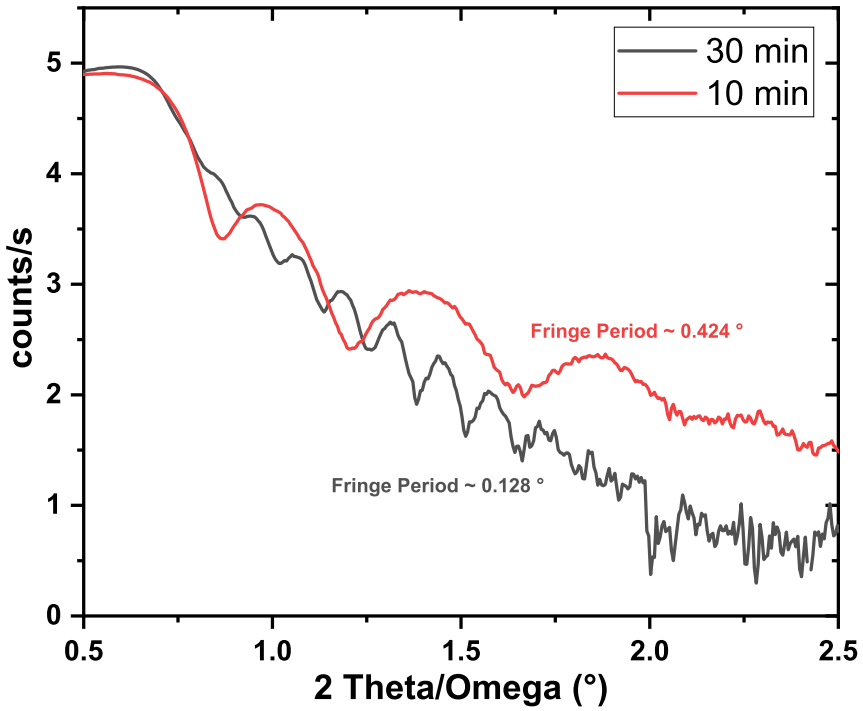

Fig. 3.1: X-ray reflectivity patterns of Alnico V thin films deposited for 10 *min* and 30 *min*.

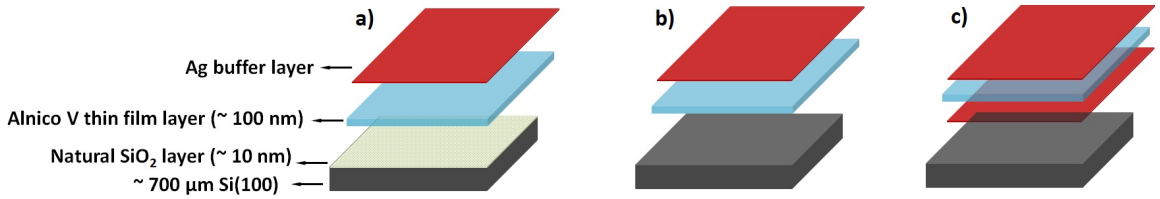

Fig. 3.2: Illustration of Alnico V thin film samples deposited (a) on Si substrate with the natural SiO_2 layer and with an Ag capping layer, (b) on Si substrate without the SiO_2 layer and with an Ag capping layer, and (c) on Si substrate sandwiched between two layers of Ag.

Atomic force microscopy (AFM) was used to investigate the quality and the surface roughness of the prepared thin film samples. Figure 3.3 shows that the as-deposited thin film sample, prepared at room temperature, has a shiny surface with a surface roughness of < 0.5 nm, which confirms the good quality of the film prepared via the sputtering method.

AFM measurements on both the heat treated and the samples prepared at high temperatures show a significant increase in the surface roughness of the samples (Figure

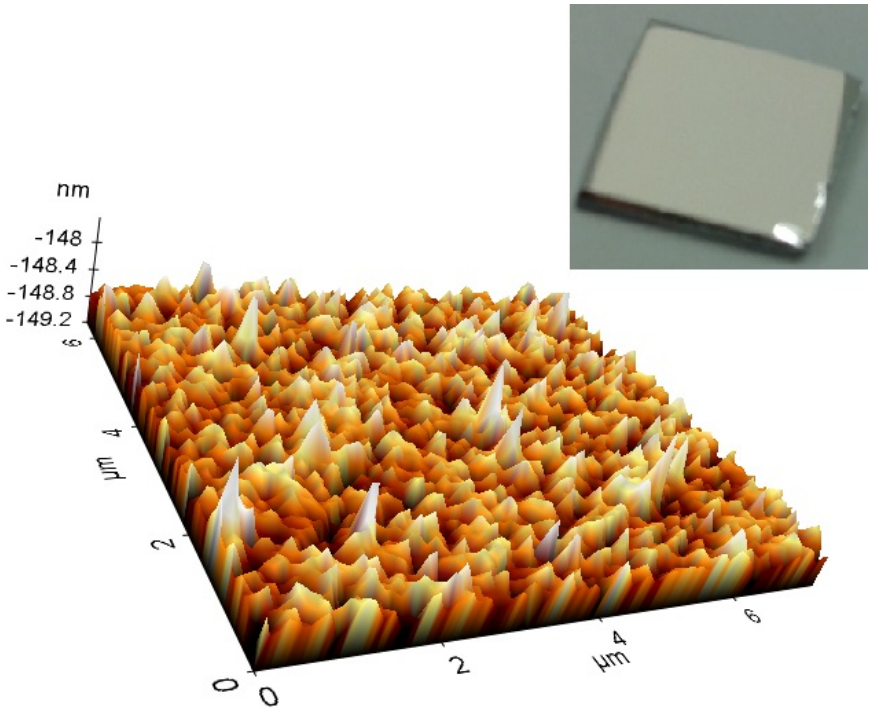

Fig. 3.3: Surface roughness measurements achieved from an AFM on the as-deposited Alnico V thin film sample prepared at room temperature and the prepared thin film sample from RF sputtering.

3.4). The results show no noticeable distinction between the surface roughness of the samples with and without the silver capping layer. The topography, measured with an AFM, shows a surface roughness of $\sim$ 50 nm in both samples.

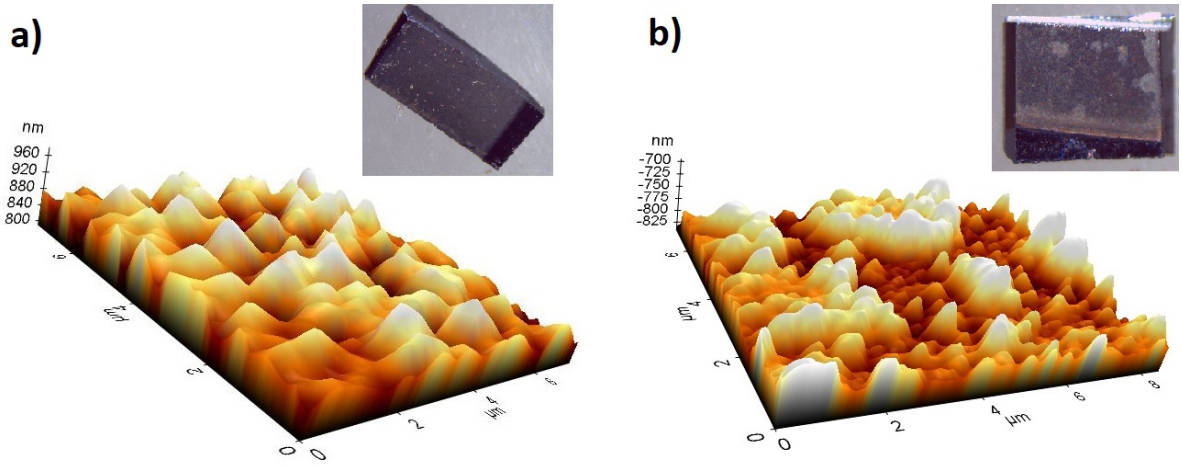

Fig. 3.4: AFM analysis on the (a) Alnico V thin film samples heat treated at 600 °C for 1 h followed by quenching, and (b) Alnico V thin film sample deposited at 500 °C.

3.2 Magnetic Studies of Alnico Thin Films

Room temperature magnetic measurements of the as-deposited thin film samples prepared on Si substrate show a H_{ci} of < 50 Oe (< 4 kA/m) which is considerably smaller than the coercivity of bulk Alnico V magnet (~ 450 Oe (~ 36 kA/m)) used as the target in the sputtering setup (shown in Table 3.1). The as-deposited samples on the Si substrate without the natural SiO_2 layer were then annealed at 600 °C, 800 °C and 900 °C for 1 h in a 300 mbar and 1.2 bar pressure Ar atmosphere followed by quenching. The film annealed at 800 °C in a 300 mbar pressure Ar atmosphere shows an increase in H_{ci} to values up to 400 Oe (32 kA/m), which is slightly smaller than the coercivity of bulk Alnico V magnets. By increasing the Ar pressure to values slightly above atmospheric pressure (1.2 bar), the coercivity of 1 kOe (80 kA/m) was observed in the thin film sample annealed at 600 °C for 1 h followed by quenching. Increasing the annealing temperature to 800 °C maximized the coercivity to 1.8 kOe (145 kA/m), which is 4 times greater than the coercivity of the bulk Alnico V, followed by a rapid decrease to values < 100 Oe (< 8 kA/m) where the sample is annealed at 900 °C (Figure 3.5). This high coercivity was also observed in the samples deposited on Si substrate with the natural SiO_2 layer, following the same heat treatment procedure.

In order to study the effect of quenching or slow cooling processes on the magnetic properties of the thin films, as-deposited thin film samples on Si substrate without the SiO_2 layer were heat-treated at 800 °C followed by slow cooling to room temperature. The magnetic measurements of the sample show a H_{ci} of ~ 1.5 kOe (120 kA/m), which is almost 3 times greater than the H_{ci} of bulk Alnico V magnet. In order to prevent the diffusion between the substrate and the film, samples of Alnico thin film, sandwiched between a thin buffer layer of silver and the silver capping layer, were prepared. These thin film samples were then heat-treated at 800 °C followed by quenching. The magnetic hysteresis loop of the sandwiched sample shows a coercivity of ~ 1.5 kOe (120 kA/m) (Figure 3.6, Table 3.1).

Unlike previous reports by Akdogan et al. [53] on high-coercivity Alnico V thin films, where a direct contact between the Alnico and Si substrate allowed the diffusion process during the heat treatment and quenching was required to form the metastable

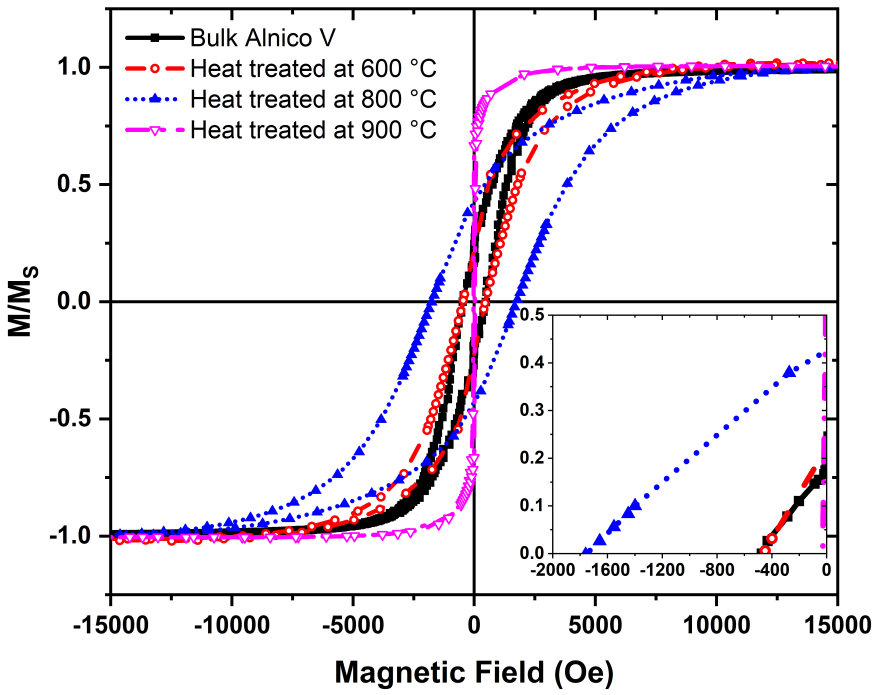

Fig. 3.5: Room temperature hysteresis loops of the commercial bulk Alnico V and RF-sputtered Ag coated thin films deposited on cleaned Si(100) substrates and annealed at 600 °C, 800 °C and 900 °C in above ambient pressure Ar atmosphere followed by quenching.

phase of Fe-Co-Si of high coercivity, our results show no such correlation, pointing to different mechanisms at work.

Even though a large saturation magnetisation is required to achieve high-performance permanent magnets, present results are mostly focused on the increase of coercivity and looking for the origin of this high coercivity in the Alnico V thin films. Compared to the M_s of bulk Alnico V magnet of $\sim$ 1200 emu/cm^3 (kA/m), the results show very low values of M_s for the high coercivity Alnico V thin films with the heat treatments.

Magnetic measurements on the as-deposited samples show that increasing the deposition temperature from room temperature up to 600 °C causes no improvement in the H_{ci} of the samples. The M_s of the Alnico V thin films deposited at high temperatures varies with the deposition temperature. However, no consistent correlation has been observed between the deposition temperature and the M_s of the as-deposited

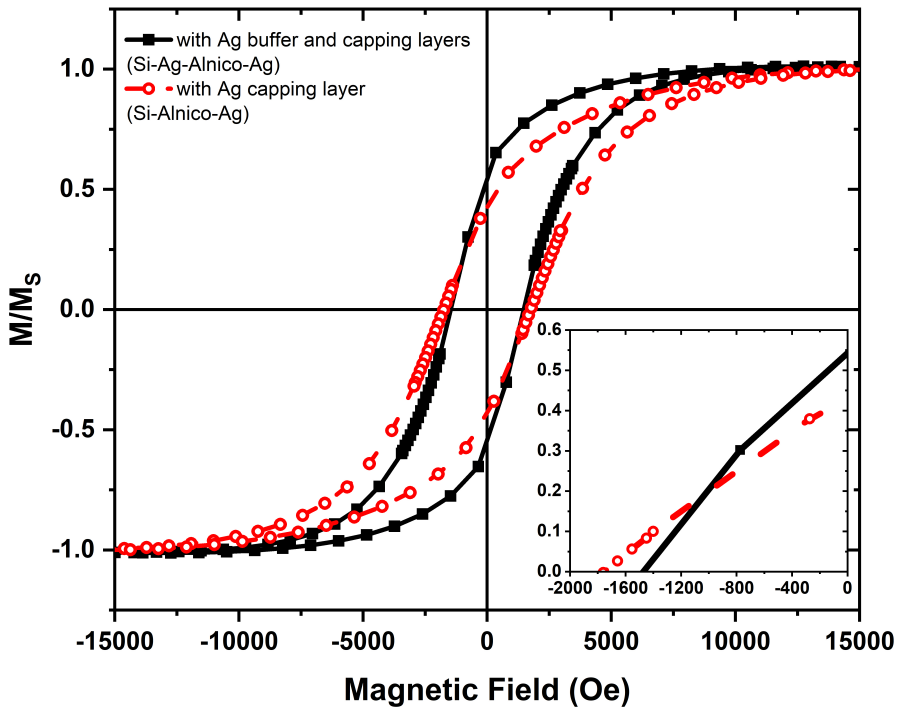

Fig. 3.6: Room temperature hysteresis loop of the sample with capping and buffer layers around Alnico thin film and the sample with only the capping layer, both samples annealed at 800 °C in 1.2 bar pressure Ar atmosphere, followed by quenching.

samples.

3.3 Structural Studies of Alnico Thin Films

In order to investigate the origin of the high coercivity observed in our samples, detailed electron microscopy analyses were performed on the high coercivity thin film samples using a TEM. Figure 3.7 shows the cross-sectional TEM image of the as-deposited Alnico V thin film sample at room temperature. The TEM with EDS analysis confirms an Alnico V layer with a uniform thickness with a silver capping layer RF-sputtered on Si substrate without the natural SiO_2 layer. The TEM image also assists to optimise the deposition rate of the RF sputtering with more accuracy.

Figure 3.8, the cross-sectional TEM image of the heat-treated film with a H_{ci} of 1.8 kOe (145 kA/m), shows the formation of a double layer inside the Alnico V layer with an average grain size of 20 nm in the lower part and of 60 nm in the upper layer. This

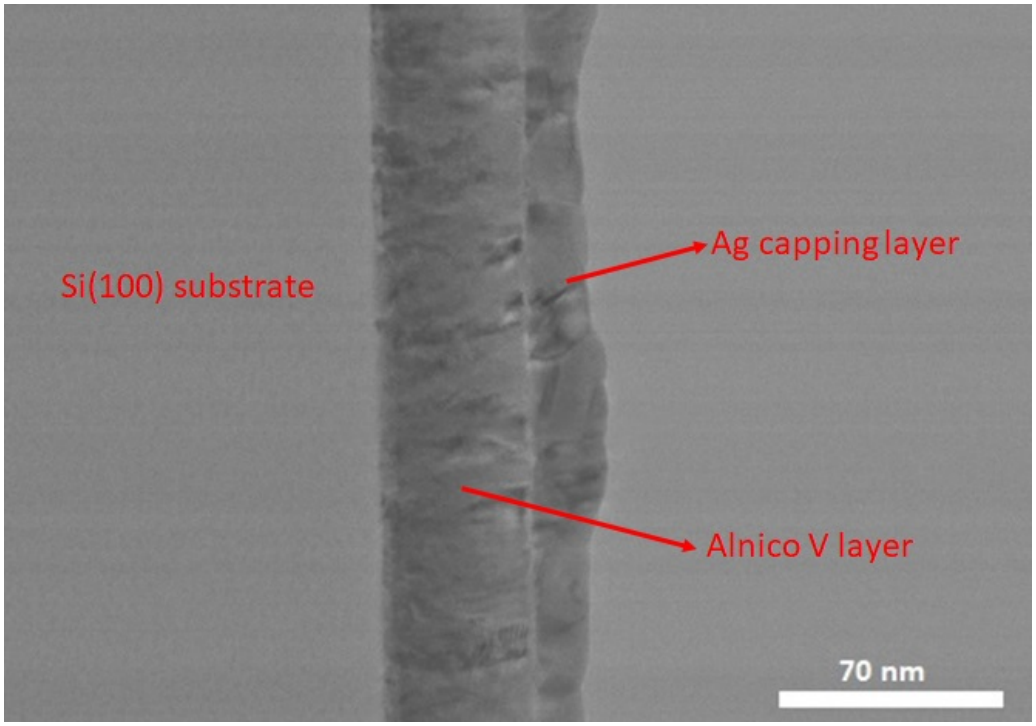

Fig. 3.7: Cross-sectional TEM image of Alnico V thin film sample deposited at room temperature with the silver capping layer.

double-layered structure on annealed Alnico V was previously reported by Akdogan et al. [53]. As no elongated precipitates were found in the thin film, the origin of high coercivity in the heat-treated films is different from the bulk Alnico magnets. The origin of the increase in the coercivity to 1.8 kOe (145 kA/m) could not be justified by the explanation given by Kumar et al. [90], who concluded that the changes in the morphology and grain size of magnetic thin films could cause an increase in the coercivity to values up to 100 Oe (8 kA/m).

TEM images also show some triangular shaped precipitates in the interface of the Alnico film and the substrate. These objects were observed in samples with high coercivity deposited on Si substrates with and without a SiO_2 layer. TEM study of the samples with low coercivity show absence of these triangular shaped precipitates. Figure 3.9 shows the cross-sectional TEM image of the as-deposited thin film sample prepared at 500 °C. The film/substrate interface is flat and free of precipitates. Magnetic measurements show a $H_{ci} < 50$ Oe (< 4 kA/m) for this sample.

Langkau et al. reported similarly shaped Ni-Fe rich features occurred at disloca-

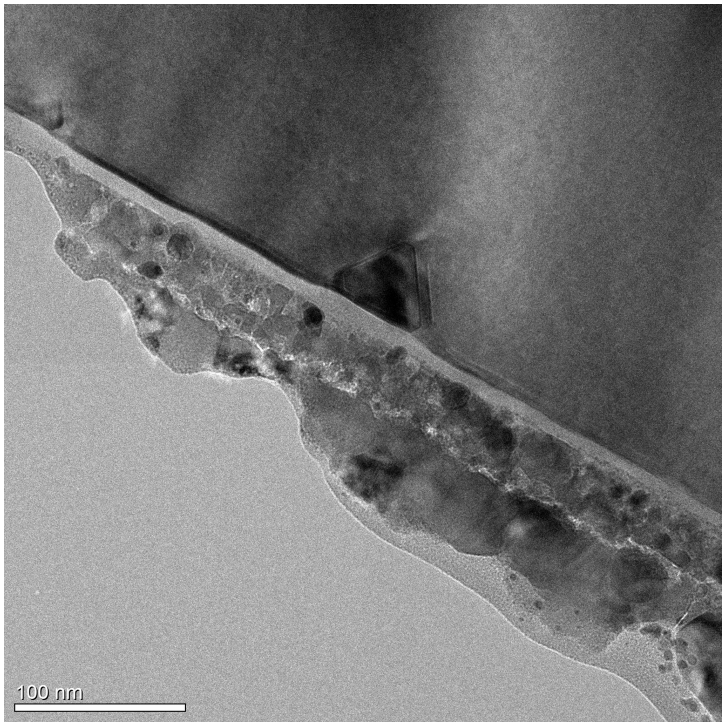

Fig. 3.8: Cross-sectional TEM image of Alnico V film RF-sputtered onto a Si/SiO_2 substrate annealed at 800 °C followed by quenching.

tions of the silicon matrix synthesized by solid-state reactions. These precipitates were identified as a $NiSi_2$-like phase with a cubic structure, space group of Fm-3m (225) and the lattice parameter of a = 5.408 Å [91]. In order to further investigate the possible mechanism behind the observed high coercivity values, a detailed high-resolution TEM (HRTEM) study was made. HRTEM images and fast Fourier transform (FFT) analysis of the triangular shaped precipitates and the Si(100) substrate of the high coercivity Alnico thin film (Figure 3.10(a)) show a similar diffraction pattern, with an equivalent estimate of the lattice parameter within experimental error, a= 5.43 ± 0.04 Å. However, HAADF STEM image (Figure 3.10(b)) reveals that the composition of this area is different from the Si substrate and contains atoms of higher atomic numbers. A linear EDS analysis in the cross-sectional STEM image of the sample from the substrate to the film (Figure 3.11(a)) shows the presence of Ni, Co, and Fe in the triangular shaped precipitates in the interface with Si substrate and confirms the interdiffusion of Si into the film and of film elements into the substrate (Figure 3.11(b)). The concentration of Al in the lower layer of the Alnico film is higher than the upper layer and the concen-

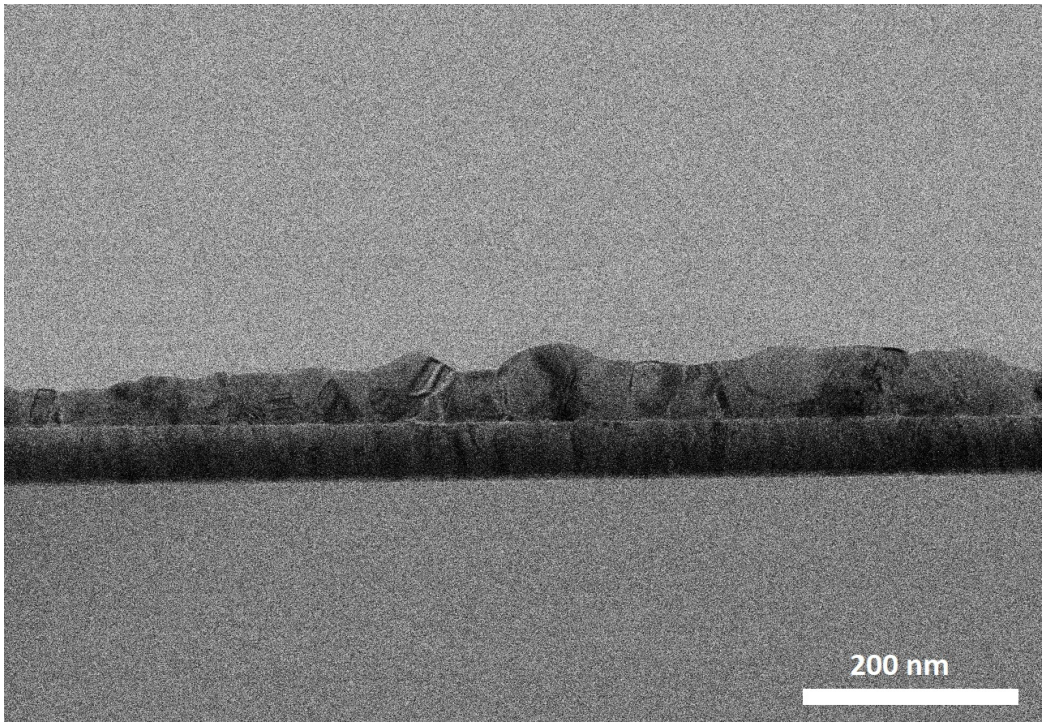

Fig. 3.9: Cross-sectional TEM image of Ag capped Alnico V thin film sample deposited at 500 °C.

tration of Fe, Co and Ni are higher in the upper layer of the film. The formation of an Al rich phase and a Fe-Co-Ni rich phase during the heat treatment might have caused the high coercivity of the heat-treated films. In order to investigate the necessity of the presence of Si substrate, Alnico thin film were deposited on MgO(100), $SrTiO_3$(100), $LaAlO_3$(100) and Al_2O_3(001) substrates and annealed at 800 °C followed by quenching as before. Unlike the samples prepared on Si substrates, these samples showed very low coercivities ($<$ 50 Oe ($<$ 4 kA/m)). This indicates that Si plays a significant role in the formation of the high coercivity phase.

Sharma et al. [92] and Fu et al. [93] reported high coercivity values of $\sim$ 1.5 kOe (120 kA/m) for Fe-Co-Ni nanowires deposited in Anodic Aluminium Oxide (AAO) templates. The higher coercivity values are due to larger shape anisotropy of the nanowires with large aspect ratios. Other studies on microstructural and magnetic properties reported Fe-Co-Ni alloys as soft magnets with coercivities $<$ 100 Oe ($<$ 8 kA/m) and a bcc/fcc structure with the lattice constant a $\sim$ 2.86 Å [94–96]. As it is shown in Figure 3.8, these triangular shaped precipitates were always present

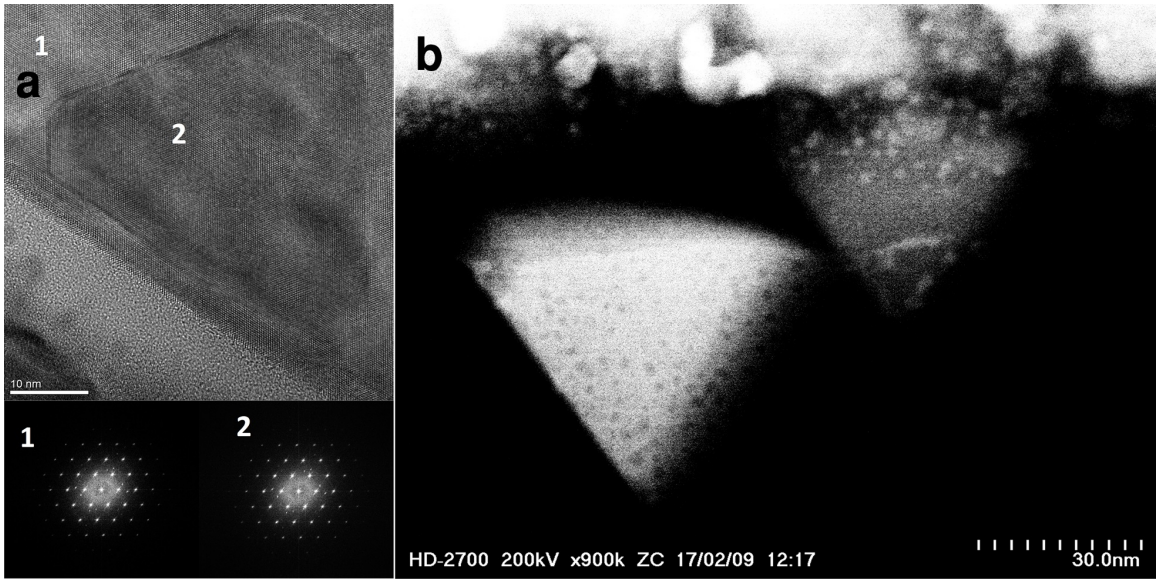

Fig. 3.10: (a) High-resolution TEM image and FFT from the Si substrate (1), a triangular shaped precipitates inside the substrate (2) and (b) HAADF-STEM image of the sample of Alnico V RF-sputtered onto a Si/SiO_2 substrate and annealed at 800 °C sample.

with small aspect ratio. Therefore, the origin of the high coercivity of the annealed samples could not be justified by shape anisotropy. The diffusion of Fe, Co, and Ni inside the Si substrate forms the triangular shaped precipitates with a different lattice constant compared to the bulk Fe-Co-Ni alloy. A possible reason for the observed high coercivity in the annealed samples might be structural deformation. While the interdiffusion of transition metal ions into a Si-like cubic structure would not directly lead to magnetocrystalline anisotropy, one possible mechanism behind the observed increased coercivity of the samples showing these triangular shaped precipitates would be a layering or otherwise structured stacking of ions of different magnetic species.

In order to prevent the diffusion between the substrate and the film, samples of Alnico thin film sandwiched between two thin buffer layers of silver were prepared. Samples were then heat-treated to 800 °C and slow cooled to room temperature. The cross-sectional STEM image and EDS analysis of the samples show the diffusion of Si to the film and formation of two layers inside the film (Figure 3.12(a)). As seen in the EDS analysis, the presence of the Ag buffer layer does not prevent the diffusion of atoms from the Si substrate to the film and vice-versa (Figure 3.12(b)). Triangular

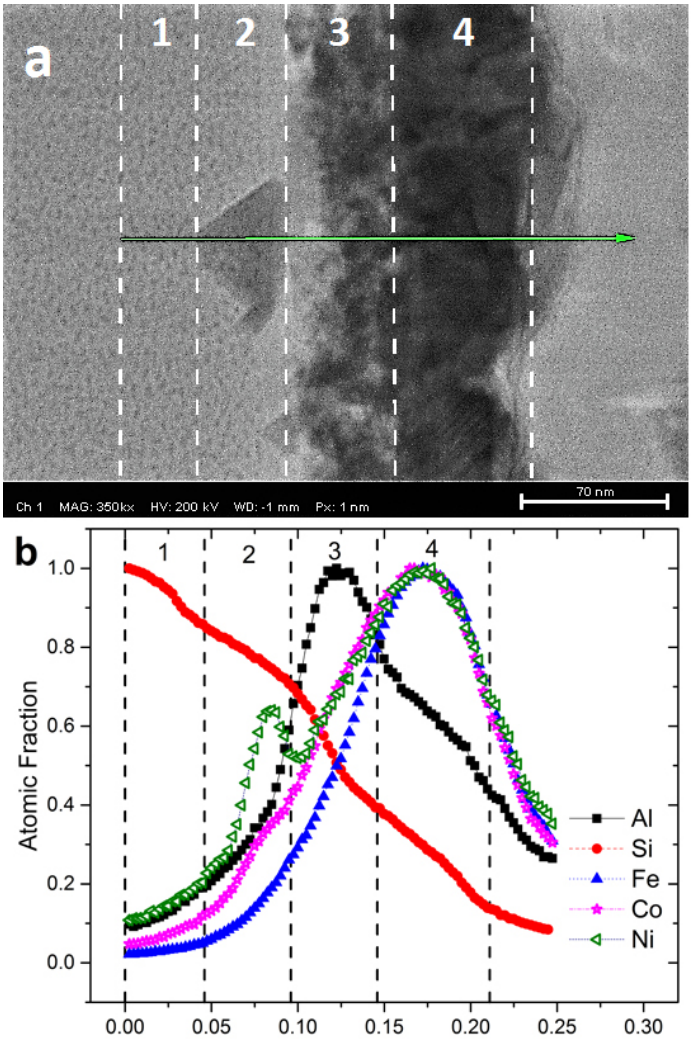

Fig. 3.11: (a) Cross-sectional STEM image of the 800 °C annealed sample with a coercivity of 1.8 kOe (145 kA/m), (b) Linear EDS.

shaped precipitates containing Fe, Ni and Co were also found inside the Si substrate of samples with the Ag buffer layer.

Further evaluation of the EDS and microscopy analyses supports the composition and structure of triangular shaped precipitates as transition metal disilicides. Silicon has a fcc cubic lattice of fd-3m (227) space group and lattice constant a = 5.4286 Å. Lattice mismatch for epitaxial growth of cubic disilicides of the transition metals (Fe, Co, Ni) on Si substrates increases from the $NiSi_2$ to the $CoSi_2$. These disilicides of the cubic lattice have space group fm-3m (225) and values of lattice constant a=5.416 Å for $NiSi_2$, a = 5.389 Å for the metastable γ-$FeSi_2$ and a = 5.364 Å for $CoSi_2$ [91, 97–99].

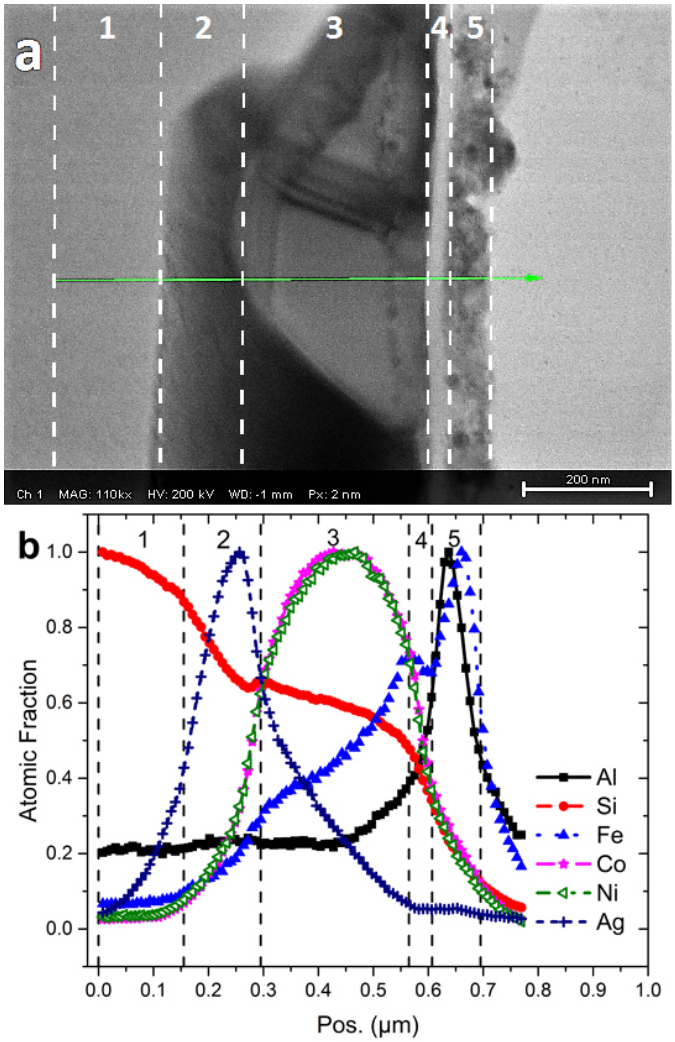

Fig. 3.12: (a) Cross-sectional STEM image of the thin film Alnico sandwiched between two buffer layers then annealed at 800 °C, (b) Linear EDS.

The solid-state solubilities of the transition metals (Fe, Co, Ni) in the Si lattice at the annealing temperatures of the present study are very low [91]. The EDS line, seen in Figure 3.11(b) and Figure 3.12(b), of the disilicides precipitates corresponds to the solid solution of $NiSi_2$ with also cubic phases of $CoSi_2$ and γ-$FeSi_2$ [91, 97]. $NiSi_2$ presents the minimum of lattice mismatch in relation to the Si lattice and $NiSi_2$ nuclei can form early [91] to allow the growth of the (Ni, Co, Fe)Si_2 solid solution. The intensification of lattice mismatch of the solid solution with increasing concentrations of Co and Fe limits the solubility in the MSi_2 solution [91], the observed solubility for Co being higher than for Fe, Figure 3.11(b) and Figure 3.12(b). The Si concentration in the

precipitate is mostly determined by 1:2 stoichiometry of disilicide. The Al substitutes Si in the MSi_2 lattice [91] and present a steep gradient across the particle and alloying of Ag with Si catalysis and accelerates the reaction to form Ni disilicides [100].

Table 3.1 summarises the types of prepared thin films and their magnetic properties, emphasizing the effect of deposition temperature, annealing conditions and silver layer deposition on M_s and H_{ci} of the Alnico V thin films.

Table 3.1: A summary of the effects of deposition temperature, post heat treatment conditions on M_s and H_{ci} of Alnico V thin films deposited on Si substrates without the SiO_2 layer.

Deposition temp. (°C)	Annealing temp. (°C)	Annealing atm. pressure (bar)	Cooling procedure	Ag buffer layer	H_{ci} (kOe)	H_{ci} (kA/m)	M_s (emu/cm^3 = kA/m)
RT	-	-	-	No	< 0.05	< 4	~ 700
200	-	-	-	No	< 0.05	< 4	~ 800
300	-	-	-	No	< 0.05	< 4	~ 1100
400	-	-	-	No	< 0.05	< 4	~ 900
500	-	-	-	No	< 0.05	< 4	~ 800
RT	800	0.3	Quenching	No	0.4	32	< 100
RT	600	1.2	Quenching	No	1	80	~ 50
RT	800	1.2	Quenching	No	1.8	145	~ 150
RT	900	1.2	Quenching	No	< 0.1	< 8	~ 100
RT	800	1.2	Slow cooling	No	1.5	120	~ 200
RT	800	1.2	Quenching	Yes	1.5	120	~ 100

* Magnetic measurements on the bulk Alnico V sample, used as the sputtering target, show a M_s of ~ 1200 emu/cm^3 (kA/m) and a H_{ci} of 450 Oe (36 kA/m).

3.4 Summary

In this chapter, we have studied the effects of different heat treatment processes on the morphology and crystal structure of high coercivity Alnico V thin films on Si substrates. A coercivity of 1 kOe was observed in the heat-treated thin film sample at 600 °C followed by quenching and maximized to 1.8 kOe (4 times greater than the bulk Alnico V value) in the sample annealed at 800 °C. It was seen that the pressure of Ar atmosphere in the quartz tubes for the heat treatment process affects the coercivity of the samples. The structural studies showed that the origin of this high coercivity is different from the formation of Fe-Co rich precipitations in Al-Ni matrix which determines the magnetic properties of the bulk Alnico magnets. Unlike previous studies on Alnico thin films on Si substrates, high coercivity values were also observed in slow-cooled samples and in those with Ag buffer layers. Fe, Co and Ni atoms diffused into the Si substrate and formed triangular shaped precipitates inside the substrate along the interface between the Si substrate and the film. While the presence of these precipitates is directly correlated to the observed high magnetic coercivity in samples, the mechanism behind the magnetocrystalline anisotropy remains unclear. Nonetheless, it could result from an inhomogeneous or layered positioning of atoms inside these features. The aim of this study was to investigate the origin of high coercivity in Alnico V thin film samples and to prepare bulk rare-earth free nanocomposite permanent magnets based on such high-coercivity Fe-Co-Si phase. However, our studies on Alnico thin film samples on Si substrates showed a different and yet novel origin of high coercivity in the prepared films; the diffusion of Fe, Co and Ni to the Si substrates and formation of triangular shaped precipitates associated to the observation of high coercivity. Major difficulties regarding the preparation of more Alnico thin film samples and on understanding the origin of this high coercivity caused to focus on another exciting field of nanostructured rare-earth free permanent magnets by preparing exchange-couple ferrite based nanocomposite magnets.

Chapter 4

Exchange-Coupled BaM/Fe_3O_4 and SrM/Fe_3O_4 Nanocomposites

Ferrite magnets, first discovered in the 1950s, are a type of technologically important material which constitute more than 50% of the global consumption of magnetic materials [31]. However, their lower $BH_{(max)}$ compared to the rare-earth permanent magnets has led to many recent investigations into the preparation of exchange-coupled nanocomposite magnets, using ferrites as both the hard and soft magnetic phases, via different techniques, such as combustion methods [101], ball milling [102], sol-gel [103] and gas aggregation [104].

Hard magnetic hexagonal barium and strontium ferrites ($BaFe_{12}O_{19}$ and $SrFe_{12}O_{19}$), also known as M-type hexaferrites (BaM and SrM), are suitable for numerous applications such as permanent magnets, electronic components, electromagnetic absorbers and also as magnetic recording material, due to their low cost, high electrical resistivity, high oxidation and corrosion resistance, great chemical stability, large H_c, and high T_C, [31, 33]. Many of these applications require controlled particle size and magnetic properties, as well as homogeneous structure. Therefore, a reliable synthesis technique is needed to produce M-type ferrites, such as co-precipitation [37], hydrothermal [38] or sol-gel auto-combustion [39].

Spinel ferrites, of general chemical formula MFe_2O_4, where M is usually a divalent metallic ion or a combination of metallic ions, are also interesting due to their potential applications such as in magnetic devices, hyperthermia and drug delivery

[54]. Among the soft spinel ferrites, Fe_3O_4 nanoparticles have attracted the interest of many investigations for use as the soft magnetic phase in exchange-coupled magnets, due to their low cost, chemical stability, high M_s, and high T_C [55, 56]. These nanoparticles are typically synthesised using chemical methods, such as sol-gel methods, co-precipitation and hydrothermal methods. Organic-solvent-free hydrothermal methods for synthesising Fe_3O_4 nanoparticles are preferable due to their simplicity and good control of particle size [57].

In this chapter, we study the exchange-coupling mechanism and show the correlation between the structural, compositional and microstructural changes and magnetic properties of BaM/Fe_3O_4 and SrM/Fe_3O_4 nanocomposites. The chapter is organised as follows: in Sec. 4.1, BaM and SrM nanoparticles preparation procedures are presented. The characterisation techniques used to optimise the calcination time and temperature to achieve single phase ferrite with optimised hard magnetic properties are presented; in Sec. 4.2 the effect of different synthesising methods on the magnetic and structural properties of Fe_3O_4 nanoparticles are presented; in Sec. 4.3 and 4.4, the exchange coupling mechanism of BaM/Fe_3O_4 and SrM/Fe_3O_4 is investigated to achieve high-performance ferrite based nanocomposite magnet. Finally, in Sec. 4.5, a summary and an overall discussion of the results is provided.

4.1 Single Phase BaM and SrM Nanoparticles

In order to investigate different M-type ferrites as the hard-magnetic phase, flake-like particles of SrM and BaM nanoparticles were produced via a sol-gel autocombustion method followed by an annealing process to form single phase powder.

4.1.1 $BaFe_{12}O_{19}$ Nanoparticles

In order to form single-phase BaM nanoparticles with optimised hard magnetic properties, the as-prepared BaM powders from the sol-gel auto-combustion method were calcined at 600 °C, 800 °C, 900 °C and 1000 °C for 1-5 h. Figure 4.1 shows the XRD patterns of the BaM nanoparticle powder before and after calcination at 600 °C for 1 h and at 1000 °C for 5 h. The XRD analysis indicates the presence of impurity

phases of hematite (Fe_2O_3) and barium carbonate ($BaCO_3$) in the non-calcined sample as well as in those calcined at 600-900 °C. After calcination at 1000 °C for 5 h, these impurity phases disappear, and all the diffraction peaks match with the standard phase of M-type barium ferrite, corresponding to JCPDS card no. 43-0002, with no other impurity phase observed. The Rietveld refinement of the BaM powder calcined at 1000 °C for 5 h using FullProf confirms the hexagonal structure of the powder with the space group of P63/mmc (194), and lattice parameters a = 5.892 Å and c = 23.216 Å. This temperature is typical of that needed to obtain single phase BaM powders [31].

TEM and SEM were used for the structural and compositional characterisation of the calcined BaM nanoparticles. Figure 4.2 shows the TEM and SEM images of the BaM nanoparticles calcined at 1000 °C for 5 h, which exhibit the formation of thin, flake-like hexagonal particles with a wide range particle size distribution and average diameter of $\sim$ 300 nm. The EDS analysis of the BaM nanoparticles, performed in the TEM also confirmed the composition of BaM nanoparticles.

Room temperature M–H hysteresis loops of calcined BaM nanoparticles are shown in Figure 4.3. As can be seen, the BaM nanoparticles calcined at 1000 °C for 5 h present the most desirable hard-magnetic properties with a M_s of 61 emu/g (61 Am^2/kg) and M_r and H_{ci} of 30 emu/g (30 Am^2/kg) and 3.56 kOe (283 kA/m) respectively. This compared well to other reported hydrothermal BaM particles [31]. The M–H hysteresis loops of BaM calcined at a low temperature of 900 °C, or a shorter time at 1000 °C (see Figure 4.3), show a small kink at low magnetic field, while the *MH* curve of the sample calcined at 1000 °C for 5 h is smooth and convex shaped. This indicates that a calcination temperature or period below 1000 °C for 5 h is not sufficient to form a completely single-phase BaM powder, which agrees with the XRD analysis. The $BH_{(max)}$ of the samples was quantified by the calculation of the area of the largest rectangle that can be inscribed under the second quadrant of the B-H hysteresis loop [105]. The BaM nanoparticles calcined at 1000 °C for 5 h also exhibit the largest $BH_{(max)}$ of 0.74 MG.Oe (5.89 kJ/m^3).

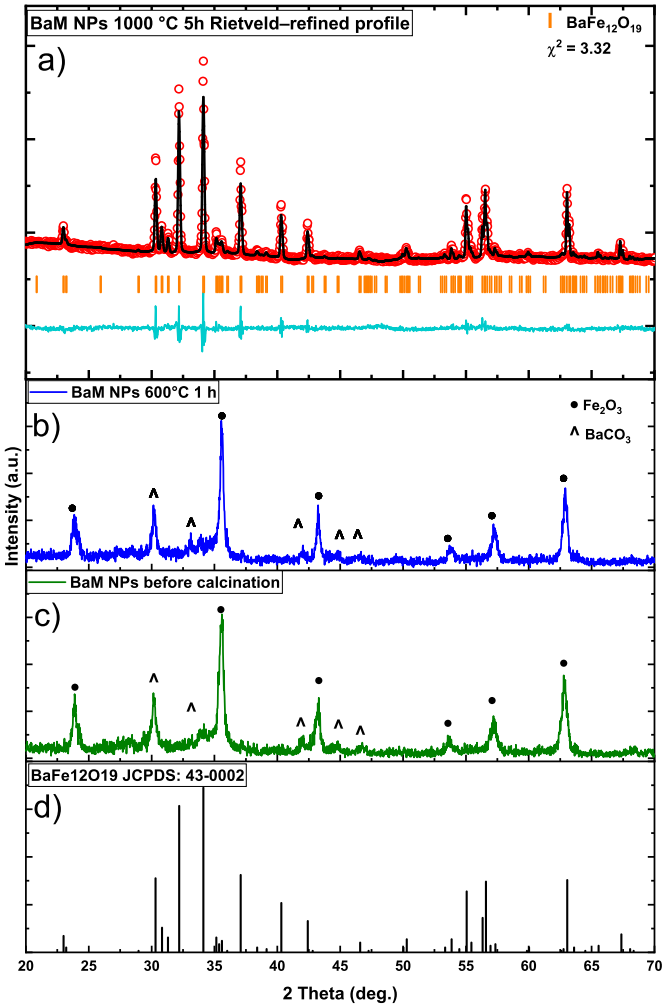

Fig. 4.1: XRD patterns of the BaM nanoparticles powder (a) calcined at 1000 °C for 5 h, (b) calcined at 600 °C for 1 h, (c) before calcination and (d) the peaks corresponding to BaM phase (JCPDS card no. 43-0002). Rietveld refinement data are also included in (a). The symbol (O) and full line represent the observed and calculated x-ray diffraction profiles, respectively. The vertical bars represent the Bragg reflection positions of the observed phase and the difference curve is plotted in the bottom.

4.1.2 $SrFe_{12}O_{19}$ Nanoparticles

In order to form single phase SrM, the as-prepared powders from the sol-gel autocombustion reaction were annealed at 1000 °C for 5 h [106, 107]. Figure 4.4 shows the XRD patterns of the SrM nanoparticle powder after calcination at 1000 °C for 5 h. The XRD analysis indicates that all the diffraction peaks match with the standard

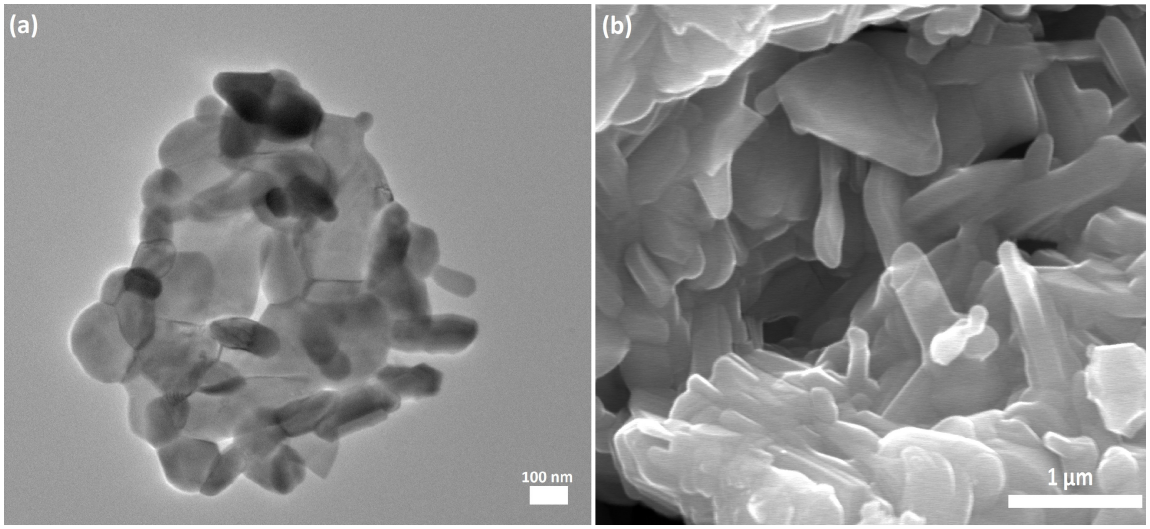

Fig. 4.2: (a) TEM image of the calcined BaM powders at 1000 °C for 5 h and (b) SEM image of the calcined BaM powders at 1000 °C for 5 h.

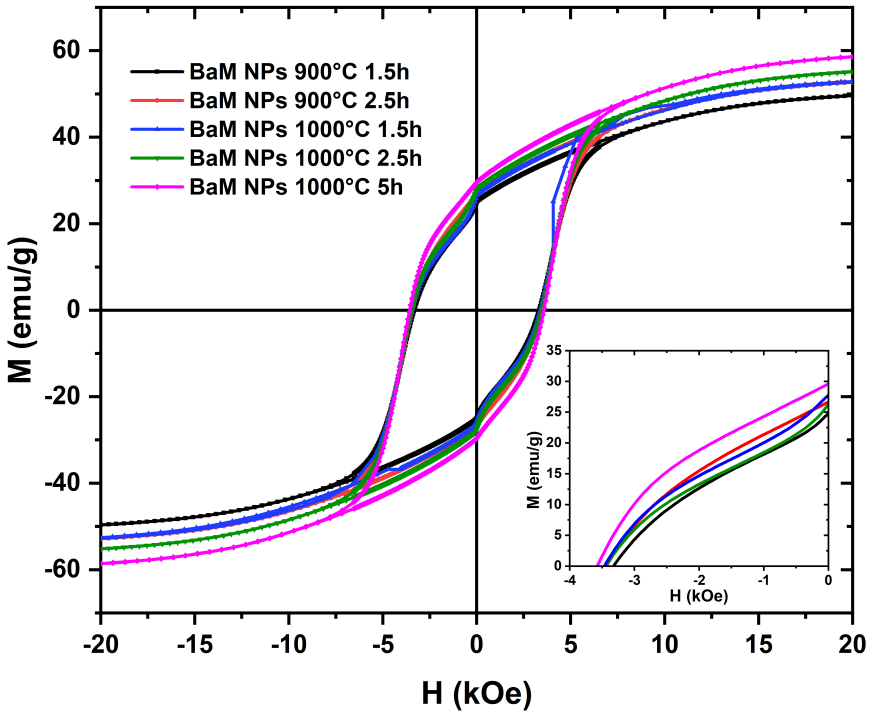

Fig. 4.3: Room temperature magnetic hysteresis (MH) loops of the BaM powders calcined at different temperatures.

phase of M-type strontium ferrite, corresponding to JCPDS card no 43-006-3369, with no other impurity phases observed. The Rietveld refinement of the SrM powder calcined at 1000 °C for 5 h using FullProf confirms the hexagonal structure of the powder

with the space group of P63/mmc (194), and lattice parameters of a = 5.882 Å and c = 23.062 Å.

Figure 4.5 shows the TEM and SEM images of the SrM nanoparticles calcined at 1000 °C for 5 h, which exhibit the formation of thin, flake-like particles with a wide range particle size distribution and an average diameter of $\sim$ 400 nm. The EDS analysis of the SrM nanoparticles, performed in both TEM and SEM also confirmed the composition of SrM nanoparticles.

Room temperature magnetic measurements were performed on the SrM nanoparticles calcined at 1000 °C for 5 h (Figure 4.6). The results show that the heat treated SrM nanoparticles have a M_s of 71 emu/g (71 Am^2/kg), M_r of 35 emu/g (35 Am^2/kg) and H_{ci} of 3.29 kOe (261 kA/m), which are comparable with the hard-magnetic properties of the calcined BaM nanoparticles at 1000 °C for 5 h.

4.2 Synthesis of Fe_3O_4 Nanoparticles

In order to study the effect of different coating methods on structural and magnetic properties of ferrite based exchange-coupled nanocomposites, magnetite nanoparticles were prepared via a hydrothermal and coprecipitation method.

To synthesize the Fe_3O_4 nanoparticles, 1.0 $kmol/m^3$ sodium hydroxide solution was added dropwise into a solution of ferric chloride and ferrous lactate with the molar ratio of 2 under vigorous stirring in an argon atmosphere to precipitate magnetite nanoparticles. In the hydrothermal method, the mixture was then transferred to an autoclave, sealed and then heated in an oven at 120 °C for 20 h. In the coprecipitation method, the mixture was heated up and kept at 70 °C for 1 h under stirring in an argon atmosphere. The prepared nanoparticles were then washed with deionised water and dried in an oven.

Figure 4.7 shows the crystalline structure analysis of the magnetite nanoparticles prepared via a hydrothermal and coprecipitation method. The XRD patterns confirm that all the diffraction peaks match those of the standard phases of magnetite, corresponding to JCPDS card no. 01-086-1336, and no impurity phases were observed. The Rietveld refinement of the Fe_3O_4 nanoparticles using FullProf confirms the cu-

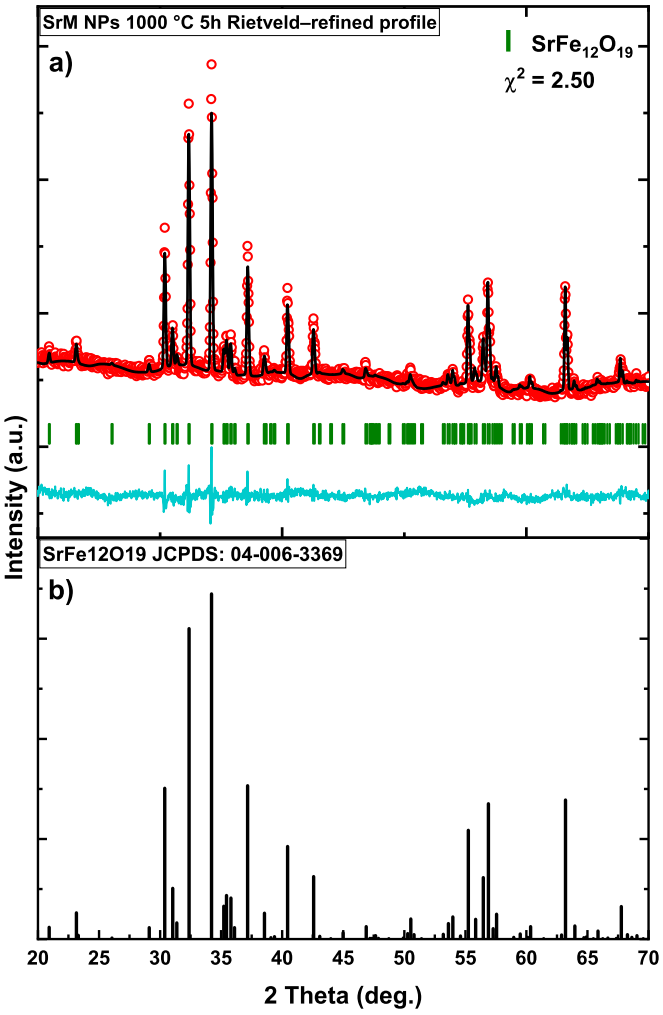

Fig. 4.4: XRD patterns of the SrM nanoparticles powder (a) calcined at 1000 °C for 5 h and (b) the peaks corresponding to SrM phase (JCPDS card no. 43-006-3369). Rietveld refinement data are also included in (a). The symbol (O) and full line represent the observed and calculated x-ray diffraction profiles, respectively. The vertical bars represent the Bragg reflection positions of the observed phase and the difference curve is plotted in the bottom.

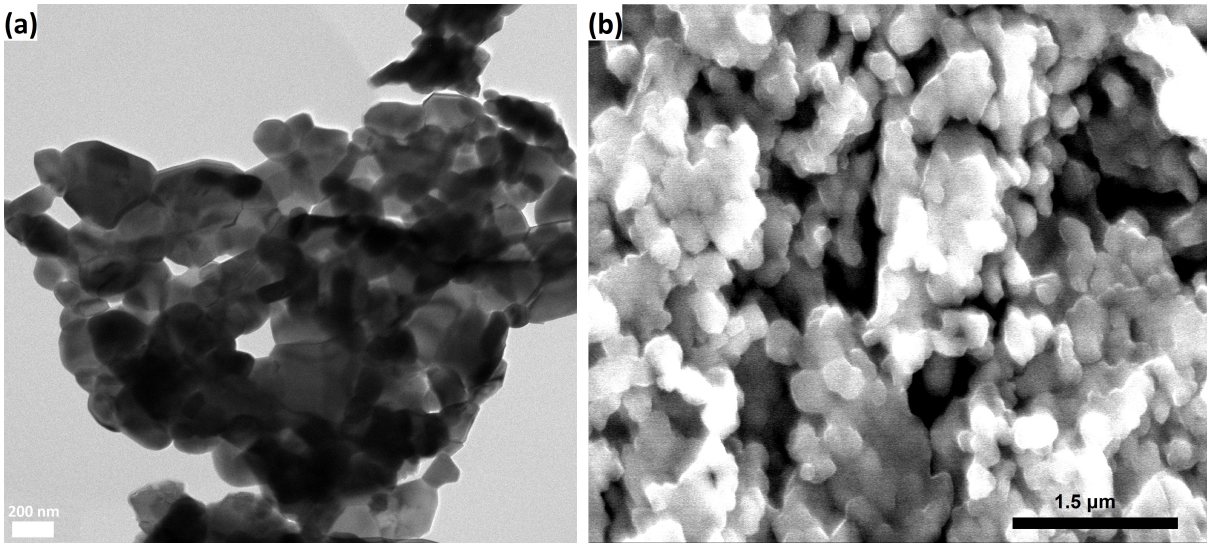

Fig. 4.5: (a) TEM image of the calcined SrM powders at 1000 °C for 5 h and (b) SEM image of the calcined SrM powders at 1000 °C for 5 h.

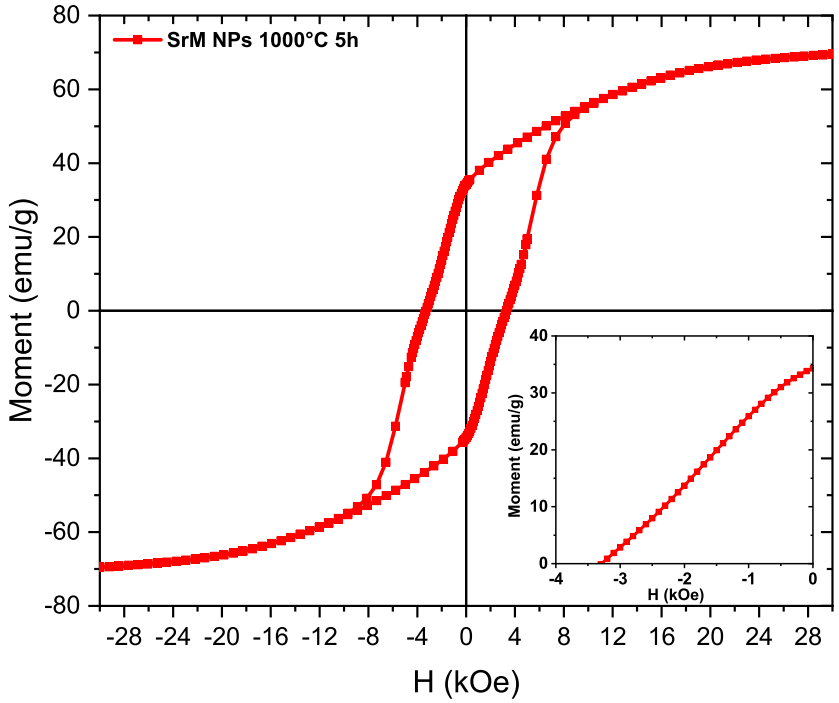

Fig. 4.6: Room temperature magnetic hysteresis (M–H) loop of the SrM powders calcined at 1000 °C for 5 h.

bic structure of the nanoparticles with the space group of Fd-3m (227), and lattice parameters of a = 8.382 Å and a = 8.364 Å for the samples prepared via a coprecipitation and hydrothermal method respectively. The average crystallite size of the

Fe_3O_4 nanoparticles, calculated from the full width at half maximum (FWHM) using the Scherrer formula, is found to be $\sim$ 148.9 Å and $\sim$ 96.5 Å for the samples prepared via a coprecipitation and hydrothermal method respectively.

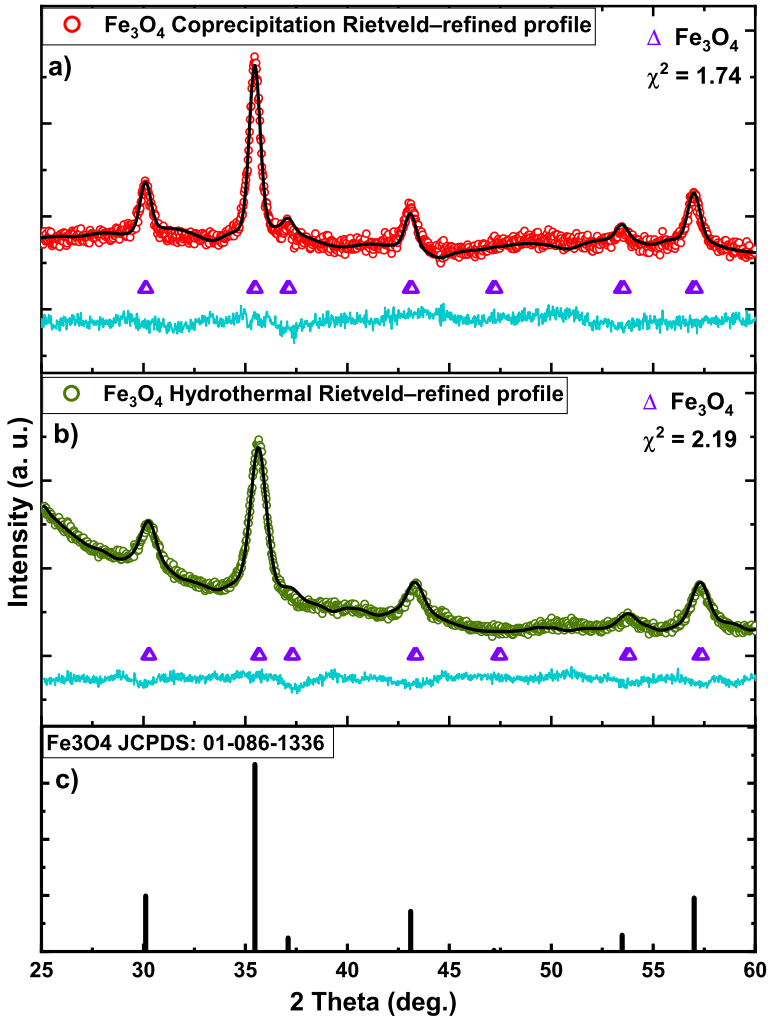

Fig. 4.7: XRD patterns of the Fe_3O_4 nanoparticles synthesised via (a) a coprecipitation and (b) a hydrothermal method; and the peaks corresponding to Fe_3O_4 phase (JCPDS card no. 01-086-1336). Rietveld refinement data are also included in (a) and (b). The symbol (O) and full line represent the observed and calculated x-ray diffraction profiles, respectively. The triangles represent the Bragg reflection positions of the observed phase and the difference curve is plotted in the bottom.

Figure 4.8 shows the TEM micrograph of Fe_3O_4 nanoparticles synthesised via a hydrothermal and coprecipitation method. The TEM images show Fe_3O_4 nanoparticles

with an average size of $\sim$ 10nm and $\sim$ 15 nm for the nanoparticles prepared by a hydrothermal and coprecipitation method respectively. The results agree with the crystallite size values calculated from the XRD patterns. This indicates that they are single nanocrystals, consisting of only one crystalline or magnetic domain.

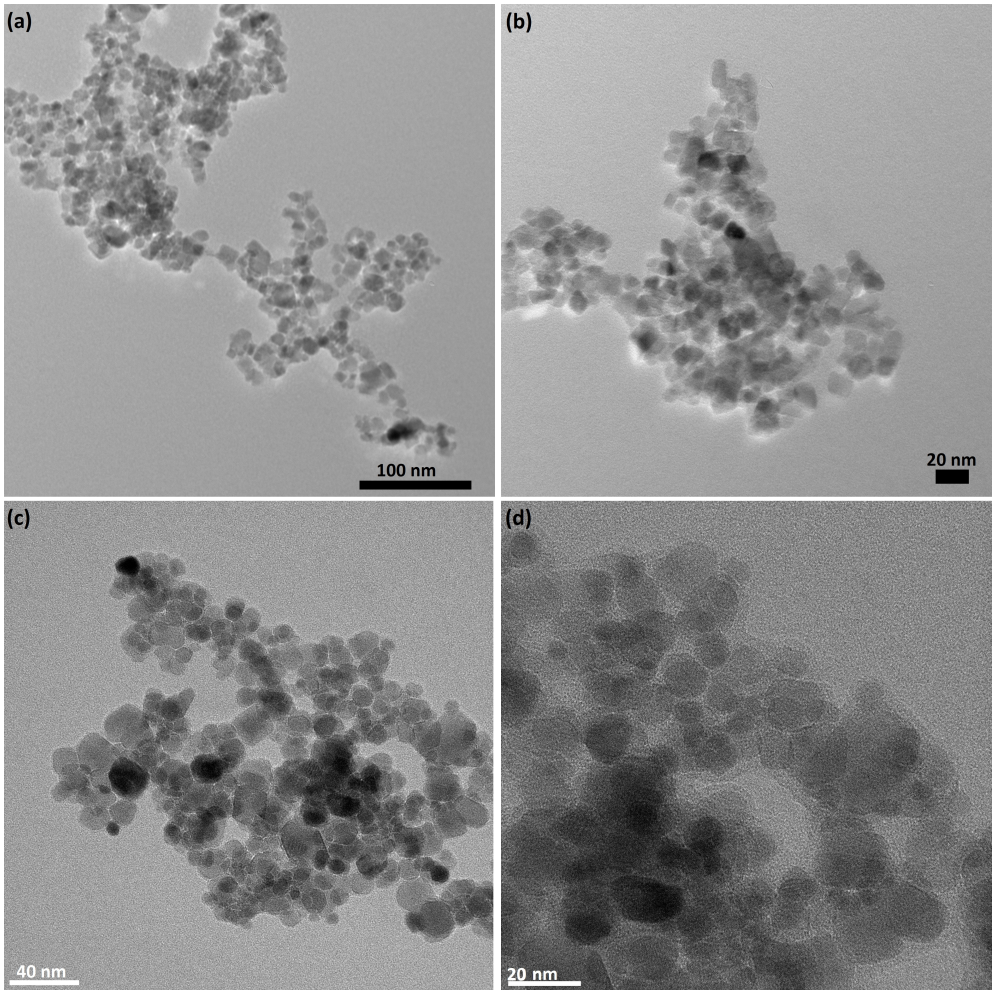

Fig. 4.8: TEM image of the Fe_3O_4 nanoparticles synthesised via (a)-(b) a hydrothermal and (c)-(d) a coprecipitation method.

In order to achieve a complete exchange coupling between the hard and the soft magnetic phases, the particle size of the soft magnetic phase should not exceed twice the domain wall thickness of the hard phase. The critical exchange length (d_{cr}) can be described by $d_{cr} = \pi\sqrt{\frac{A_S}{K_H}}$ [42]. Where, A_S is the exchange stiffness of the soft phase ($A_S = 1.32 \times 10^{-11}$ J/m for Fe_3O_4 [108]) and K_H is the magnetocrystalline anisotropy of the hard phase ($K_H = 330$ kJ/m^3 for BaM [109] and $K_H = 360$ kJ/m^3 for SrM

[110]). Therefore, for BaM/Fe_3O_4 and SrM/Fe_3O_4 exchange-coupling systems $d_{cr} \approx$ 20 nm. Figure 4.9 shows the particle size distribution of the magnetite nanoparticles, prepared via a hydrothermal and coprecipitation method. Unlike the Fe_3O_4 nanoparticles, prepared via a hydrothermal method, which obtained an average particle size of $\sim$ 10 nm and a narrow size distribution (σ = 2.92 nm), the Fe_3O_v4 nanoparticles synthesised via a coprecipitation method exhibit a noticeably wider size distribution (σ = 6.11 nm) with an average particle size of $\sim$ 15 nm. The cumulative percent graph in Figure 4.9 shows that all the Fe_3O_4 nanoparticles prepared via a hydrothermal method have diameters below d_{cr}. However, in the coprecipitation method, 85% of the Fe_3O_4 nanoparticles have diameters below d_{cr} which could lead to an incomplete exchange coupling. A complimentary Brunauer-Emmett-Teller (BET) analysis was performed on the magnetite nanoparticles to determine the surface area of the powders. The results show that Fe_3O_4 nanoparticles, prepared via a hydrothermal method have larger value of surface area (77.74 m^2/g) compared to the nanoparticles prepared via a coprecipitation method (58.99 m^2/g). The results confirm the smaller value of the average particle size for the particles prepared by a hydrothermal method. The BET analysis on the calcined BaM and SrM nanoparticles shows a surface area of 2.73 m^2/g and 2.12 m^2/g, respectively. This confirms the larger average particle size of the annealed SrM nanoparticles compared to BaM nanoparticles.

Room temperature M–H hysteresis loops of Fe_3O_4 nanoparticles are shown in Figure 4.10. The as-prepared Fe_3O_4 nanoparticles via a hydrothermal method exhibit a M_s of 91 emu/g (91 Am^2/kg) and the coprecipitated Fe_3O_4 nanoparticles exhibit a M_s of 85 emu/g (85 Am^2/kg). Both samples show H_{ci} values $<$ 50 Oe ($<$ 4 kA/m). The magnetic parameters confirm their applicability as the soft magnetic phase in this nanocomposite. Such high M_s values are typical for single domain Fe_3O_4 NPs, with very small, virtually superparamagnetic, H_{ci} values [111].

4.3 BaM/Fe_3O_4 Nanocomposite

The BaM/Fe_3O_4 nanocomposites with mass ratios of 1:1, 3:1 and 9:1 were prepared via coating the single phase BaM nanoparticles calcined at 1000 °C for 5 h with mag-

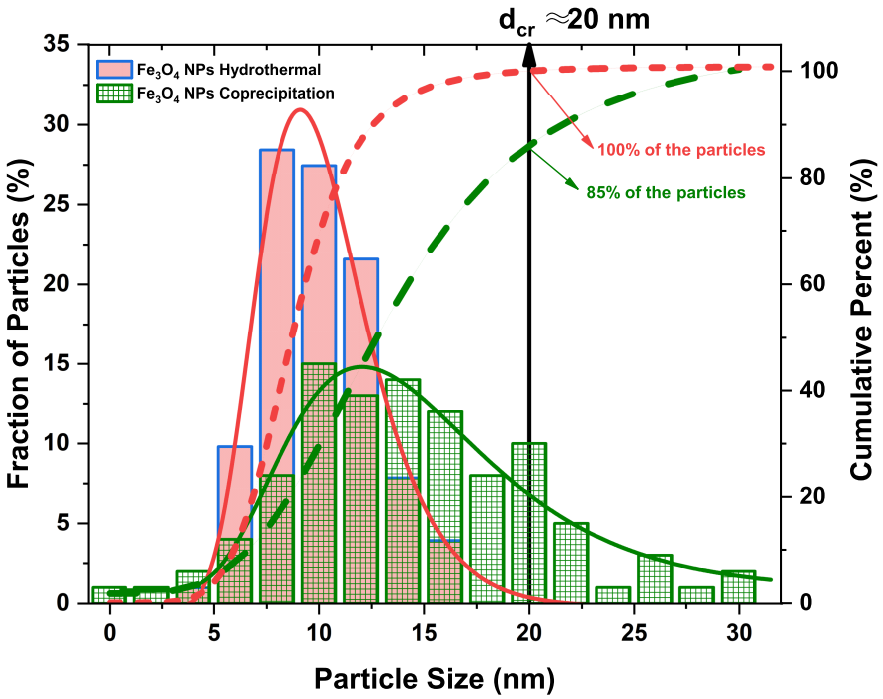

Fig. 4.9: Particle size distribution of Fe_3O_4 nanoparticles prepared via a hydrothermal and a coprecipitation method.

netite nanoparticles by mixing different amounts of calcined BaM powder to the ferrous/ferric solution in the hydrothermal process. Figure 4.11 shows the XRD patterns of the BaM/Fe_3O_4 nanocomposite with the mass ratio of 1:1. The diffraction pattern clearly shows the characteristic diffraction peaks of both BaM and Fe_3O_4 with no other impurity peaks. The peaks corresponding to the soft spinel ferrite phase are broader due to their smaller size. The Rietveld refinement of the nanocomposite samples (included in Figure 4.11(a)), with the χ^2 (goodness-of-fit quality factor) of 1.98, shows no significant changes in the lattice parameters of each phase in the as-coated samples.

Figure 4.12 shows the TEM images of the BaM/Fe_3O_4 nanocomposite with the mass ratio of 9:1, which clearly shows that following the hydrothermal synthesizing method, the magnetite nanoparticles coat the flake-like hexagonal BaM nanoparticles. Figure 4.12(c) exhibits a homogeneous precipitation of the Fe_3O_4 nanoparticles on the surface of the calcined BaM, which can lead to a maximisation of the exchange-coupling between the hard and soft magnetic phases. As seen in Figure 4.12(c) the coated surface of the BaM nanoparticles appears flat, which indicates that a low amount of

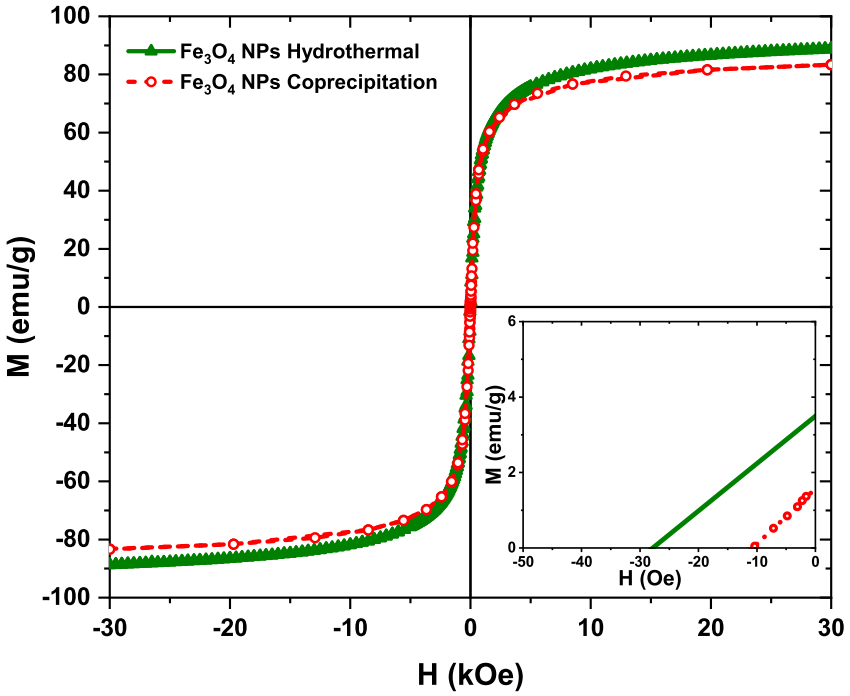

Fig. 4.10: Room temperature magnetic hysteresis loops of the as-prepared Fe_3O_4 nanoparticles.

interdiffusion and reaction between them.

To confirm the crystallinity of both magnetite and BaM nanoparticles, together with the interface between them, a high resolution TEM (HRTEM) analysis was performed. Figure 4.13 shows HRTEM image of the interface between the Fe_3O_4 nanoparticles on flake-like BaM powders in the nanocomposite with the mass ratio of 9:1. The HRTEM of the BaM powder, obtained from region I (Figure 4.13(b)), shows a lattice spacing of 0.42 nm, which corresponds to the (103) plane of the $BaFe_{12}O_{19}$ phase, in good agreement with the XRD results. The HRTEM image and the diffraction pattern obtained from fast Fourier transform (FFT) analysis confirm the high crystallinity of the BaM powder. Figure 4.13(c) shows the HRTEM micrograph and FFT analysis of Fe_3O_4 nanoparticles (region II). It can be seen that the as-synthesised Fe_3O_4 nanoparticles have high crystallinity with a lattice spacing of 0.23 nm, which corresponds to the (222) plane of the spinel magnetite phase and agrees well with the XRD results.

Figure 4.14 shows the room temperature magnetic hysteresis loops of the as-prepared Fe_3O_4 nanoparticles, the BaM nanoparticles calcined at 1000 °C for 5 h

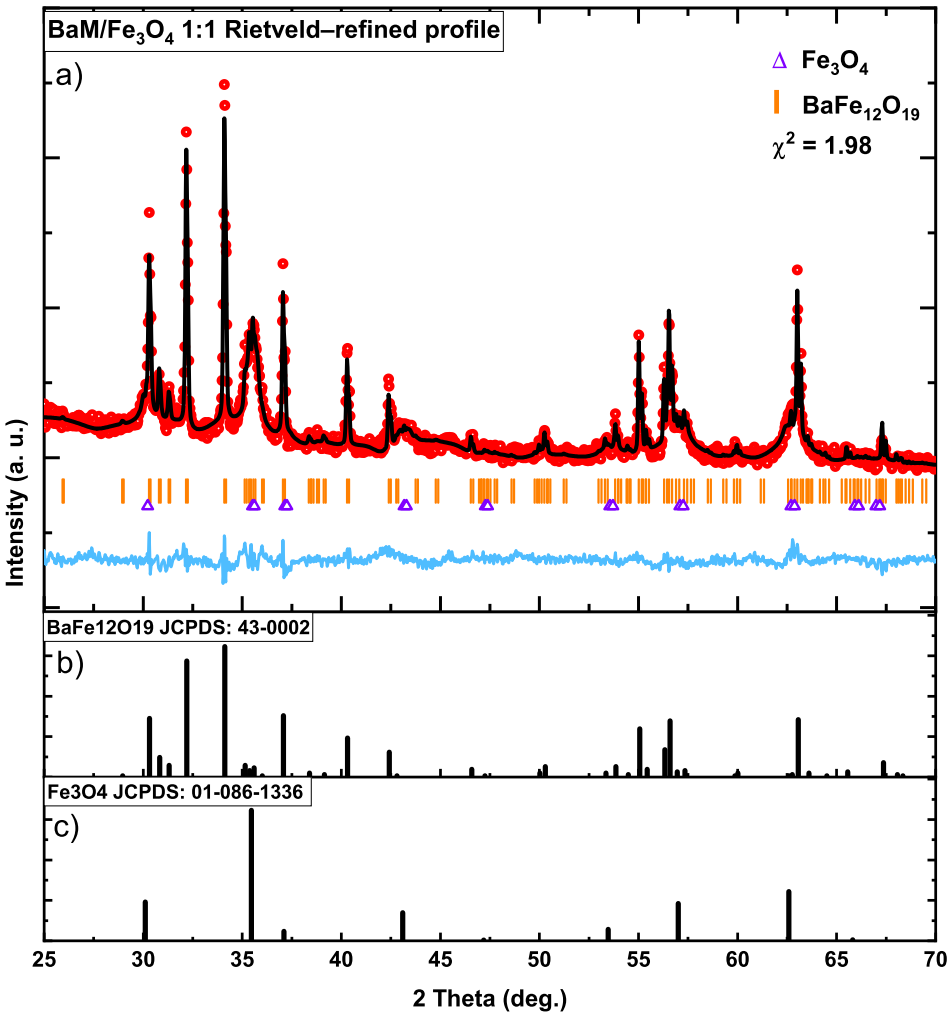

Fig. 4.11: XRD patterns of (a) BaM/Fe_3O_4 1:1 nanocomposite powder, (b) the peaks corresponding to BaM phase (JCPDS card no. 43-002), and (c) the peaks corresponding to Fe_3O_4 phase (JCPDS card no. 01-086-1336). Rietveld refinement data are also included in (a) for the BaM/Fe_3O_4 1:1 nanocomposite powder. The symbol (O) and full line represent the observed and calculated x-ray diffraction profiles, respectively. The vertical bars and the triangles represent the Bragg reflection positions of the observed phases and the difference curve is plotted in the bottom.

and the as-coated calcined BaM nanoparticles with Fe_3O_4 nanoparticles with the mass ratios of 1:1, 3:1 and 9:1. The hysteresis loops of the as-coated BaM/Fe_3O_4 nanocomposite samples with different mass ratios, show an increase of up to 40% in M_s value, up to 89 emu/g (89 Am^2/kg) in the nanocomposites compared to the calcined BaM

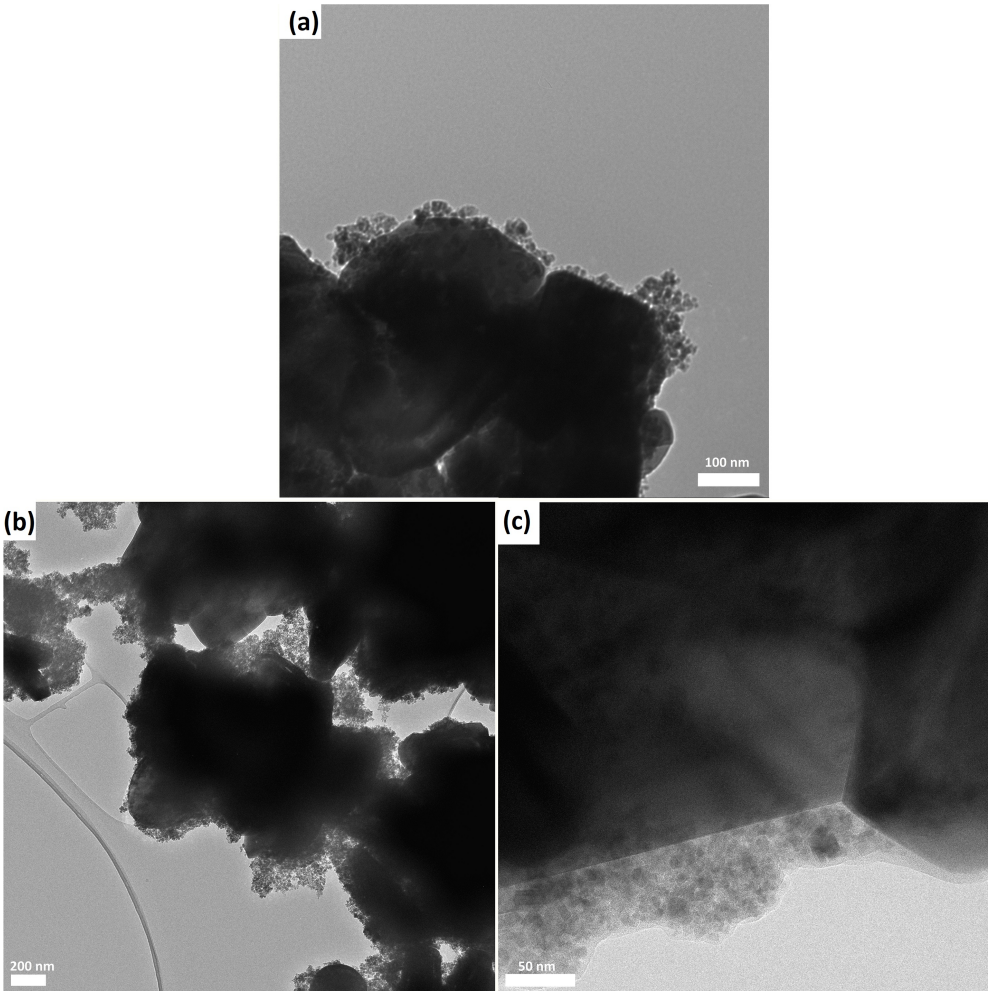

Fig. 4.12: TEM image of the as-coated BaM/Fe_3O_4 9:1 nanocomposite powder with different magnifications.

powder (values in Table4.1). The mass ratio of the soft magnetic phase does not have any significant effect on the value of the M_s in the nanocomposite samples. However, the value H_{ci} varies greatly with the hard magnetic phase content, and is maximised in the nanocomposite sample with the mass ratio of 9:1 (Table 4.1). The nanocomposites with the mass ratios of 1:1 and 3:1 do not exhibit a smooth hysteresis loop due to an incomplete exchange-coupling between the soft and the hard magnetic phases. However, the hysteresis loop of the as-coated nanocomposite with the mass ratio of 9:1 shows a smooth hysteresis loop without the dual magnetic phase behaviour, which confirms the formation of a fully-coupled exchange-coupled hard magnetic powder. This 9:1 nanocomposite sample also shows the largest H_{ci} of 3.58 kOe (285 kA/m), which leads

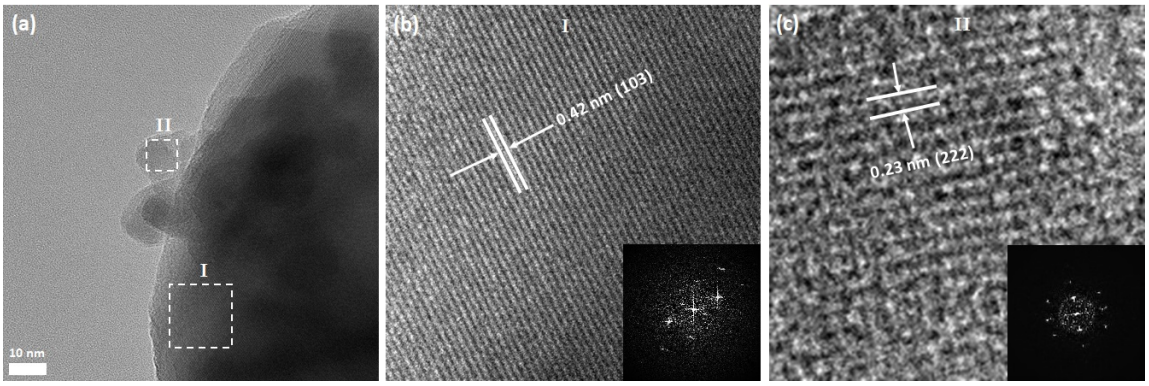

Fig. 4.13: (a) HRTEM of the interface between Fe_3O_4 and BaM nanoparticles in the as-coated 9:1 nanocomposite (b) zoomed in HRTEM image and FFT of the region I, corresponds to BaM nanoparticle, and (c) zoomed in HRTEM image and FFT of the region II, corresponds to Fe_3O_4 nanoparticle.

to a significant enhancement of 75% of $BH_{(max)}$, with the value of 1.14 MG.Oe (9.07 kJ/m^3), compared with the parent hard magnetic phase (Table 4.1).

In order to investigate the effect of post-heat treatment on the magnetic properties of the nanocomposites, which has been reported as an essential step to form the exchange coupling between the soft and the hard magnetic phases in previous studies [55, 56], as-coated nanocomposite samples were annealed at 300 °C, 400 °C, 500 °C and 600 °C for 1 h. A post-heat treatment process improves the coercivity of the samples with mass ratios of 1:1 and 3:1. However, the magnetic measurements exhibit no significant improvement in the sample with the mass ratio of 9:1, which has the most promising hard magnetic properties (Figure 4.14). Not requiring a post-heat treatment leads to a reduction of cost, and simplifies the preparation of this high-performance BaM/Fe_3O_4 nanocomposite hard magnetic powder.

In order to further evaluate the exchange coupling behaviour of the nanocomposite samples, the switching field distribution (SFD) curves were plotted by taking the 1st derivative of the demagnetisation curve (dM/dH of the demagnetisation curve), as shown in Figure 4.15. The presence of a single peak in the SFD plot of the calcined BaM confirms the formation of a single-phase hard phase after calcination at 1000 °C for 5 h. As for the nanocomposite samples, the dM/dH curves of the nanocomposites with the mass ratios of 1:1 and 3:1 exhibit two distinct peaks, which is due to the

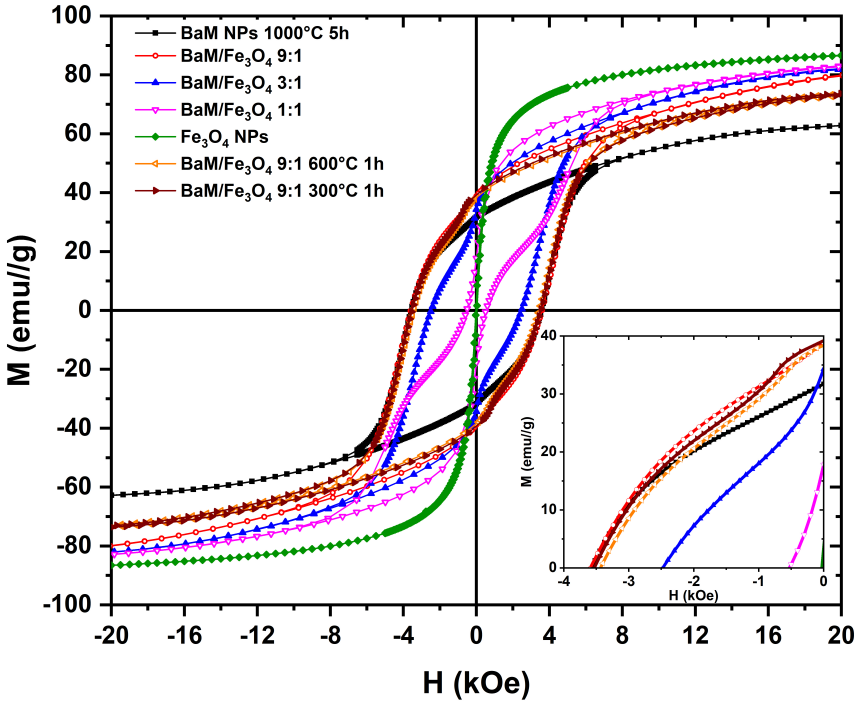

Fig. 4.14: Room temperature magnetic hysteresis (MH) loops of the BaM powders calcined at 1000°C for 5 h, as-prepared Fe_3O_4 nanoparticles, as-coated BaM/Fe_3O_4 nanocomposite powder with different mass ratios and BaM/Fe_3O_4 9:1 nanocomposite annealed at 300 °C and 600 °C for 1 h.

uncoupled or weak coupling between the soft and the hard magnetic phases [112]. For the BaM/Fe_3O_4 nanocomposite with the mass ratio of 9:1 a broad single peak is observed which confirms the fully coupled exchange between the two magnetic phases. The reduction of the intensity of the peak of the soft phase from the nanocomposite with the mass content of 1:1 to 9:1, together with the increasing of the peak due to the hard phase also confirms the improvement of the exchange-coupling by increasing the percentage of the hard magnetic phase in the nanocomposite.

4.4 SrM/Fe_3O_4 Nanocomposite

To form the exchange-coupled SrM/Fe_3O_4 nanocomposite, calcined SrM powders were coated with magnetite nanoparticles via the coprecipitation method with the SrM/Fe_3O_4 mass ratio of 9:1. Figure 4.16 shows the crystalline structure of the coated

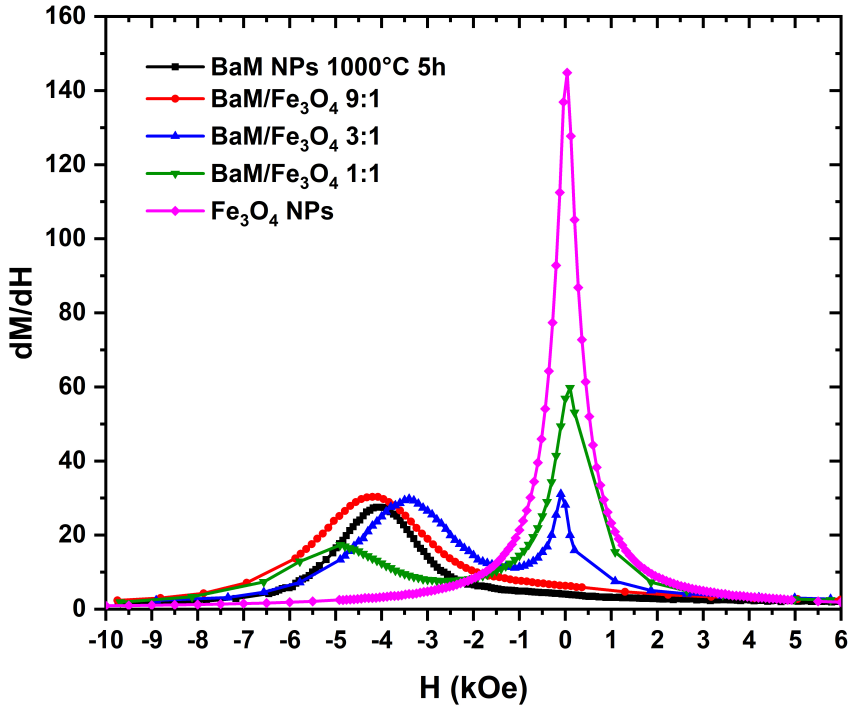

Fig. 4.15: Switching field distribution curves (dM/dH of demagnetisation curves) of the BaM nanoparticles calcined at 1000 °C for 5 h, as-prepared Fe_3O_4 nanoparticles and BaM/Fe_3O_4 nanocomposite powder with different mass ratios.

powder. The XRD pattern confirms that all the diffraction peaks match with the standard phases of strontium hexaferrite phase, corresponding to JCPDS card no. 04-006-3369, and magnetite phase, corresponding to JCPDS card no. 01-086-1336, and no impurity phases were observed. The Rietveld refinement of the nanocomposite sample, with the $\chi^2 = 2.47$, shows no significant changes in the lattice parameters of each phase in the as-coated samples.

Figure 4.17 shows the TEM images of SrM/Fe_3O_4 nanocomposite with the mass ratio of 9:1. The TEM images confirm that via a coprecipitation method, magnetite nanoparticles coat the surface of the annealed flake-like SrM nanoparticles, also allowing exchange coupling between the hard and the soft magnetic phases.

A HRTEM study was performed on the SrM/Fe_3O_4 nanocomposite to confirm the crystallinity of both magnetite and SrM nanoparticles, and to expose the interface between them (Figure 4.18). The flat interface between the two phases confirms a low amount of interdiffusion and reaction between them. The HRTEM of the SrM powder,

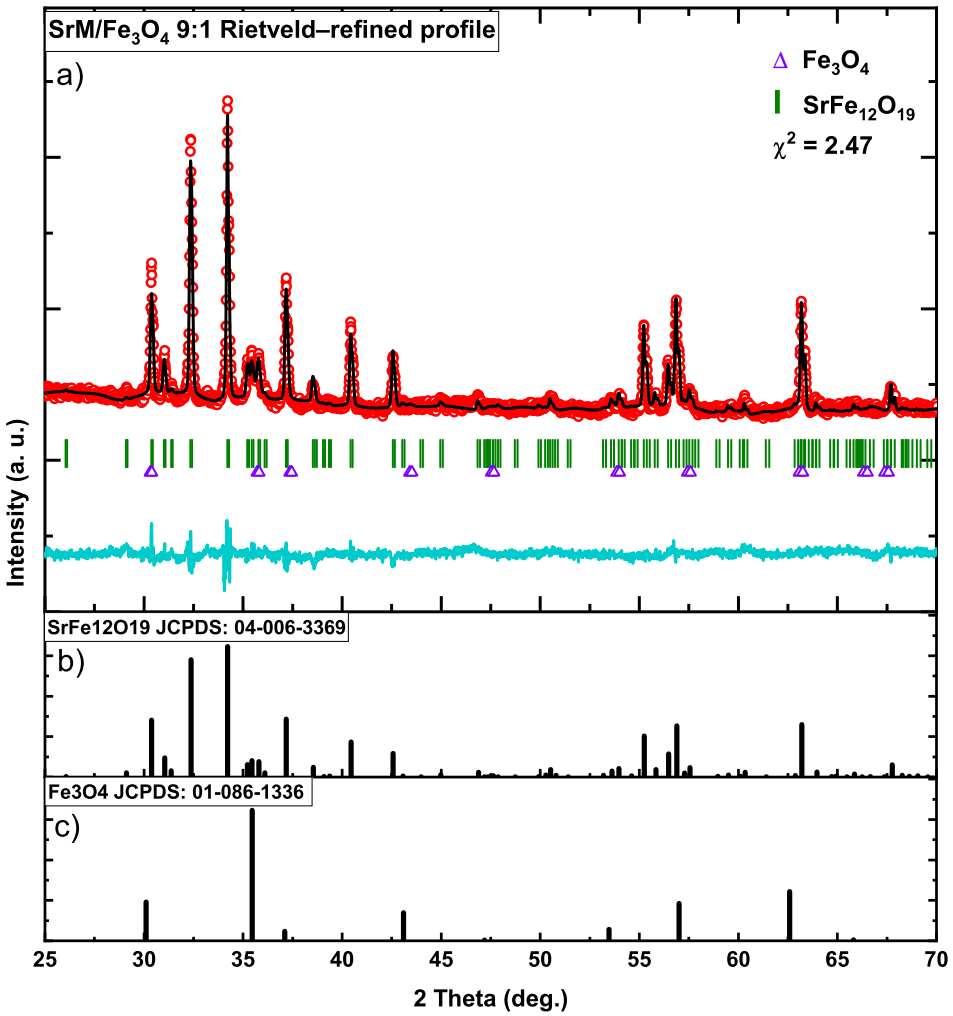

Fig. 4.16: XRD patterns of SrM/Fe_3O_4 9:1 nanocomposite powder. The corresponding peaks of SrM phase (JCPDS card no. 04-006-3369), and Fe_3O_4 phase (JCPDS card no. 01-086-1336) are marked. Rietveld refinement data are also included in (a) for the SrM/Fe_3O_4 9:1 nanocomposite powder. The symbol (O) and full line represent the observed and calculated x-ray diffraction profiles, respectively. The vertical bars and the triangles represent the Bragg reflection positions of the observed phases and the difference curve is plotted in the bottom.

obtained from region I (Figure 4.18(b)), shows a lattice spacing of 0.39 nm, which corresponds to the (006) plane of the $SrFe_{12}O_{19}$ phase, in agreement with the XRD results. The HRTEM image and the diffraction pattern obtained from fast Fourier transform (FFT) analysis confirm the high crystallinity of SrM powder. Figure 4.18(c)

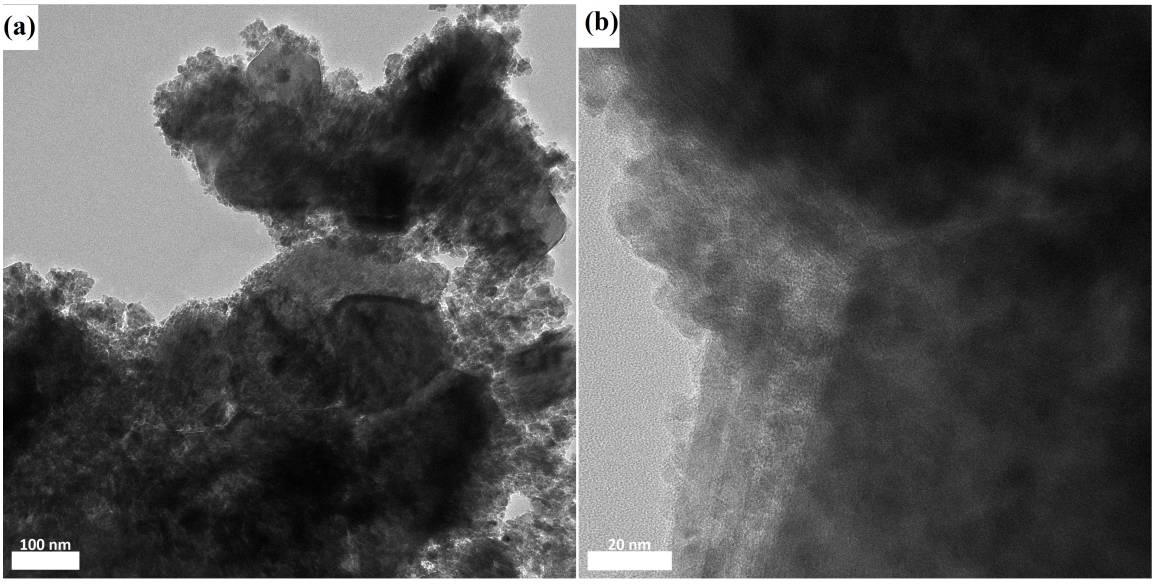

Fig. 4.17: TEM image of the as-coated SrM/Fe_3O_4 9:1 nanocomposite powder with different magnifications.

shows the HRTEM micrograph and FFT analysis of Fe_3O_4 nanoparticles (region II). It can be seen that the as-synthesised Fe_3O_4 nanoparticles have high crystallinity with a lattice spacing of 0.21 nm, which corresponds to the (400) plane of the spinel magnetite phase and agrees with the XRD results.

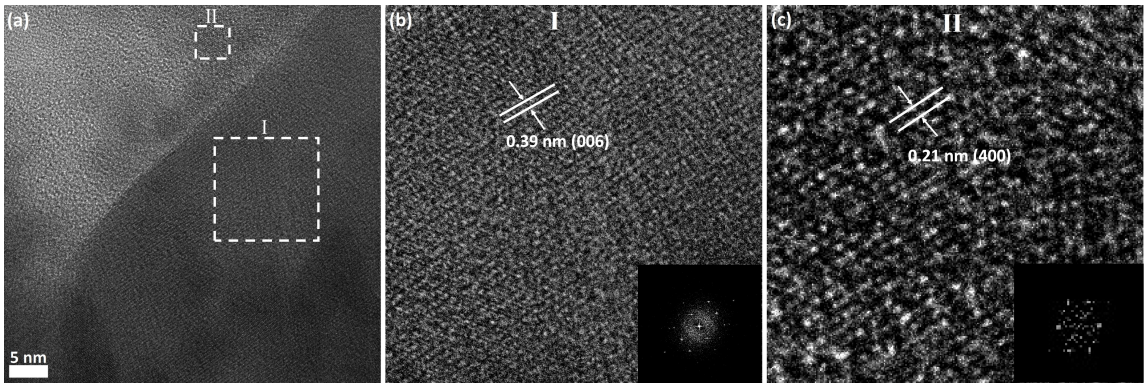

Fig. 4.18: (a) HRTEM of the interface between Fe_3O_4 and SrM nanoparticles in the as-coated 9:1 nanocomposite (b) zoomed in HRTEM image and FFT of the region I, corresponds to SrM nanoparticle, and (c) zoomed in HRTEM image and FFT of the region II, corresponds to Fe_3O_4 nanoparticle.

Figure 4.19 shows the room temperature magnetic hysteresis loops of the SrM nanoparticles annealed at 1000 °C for 5 h, the as-prepared Fe_3O_4 nanoparticles synthe-

sised by a coprecipitation method and the as-coated annealed SrM nanoparticles with magnetite nanoparticles with the mass ratio of 9:1. The magnetic measurements on the SrM/Fe_3O_4 nanocomposite show a H_{ci} of 2.64 kOe (210 kA/m), M_s of 80 emu/g (80 Am^2/kg) and $BH_{(max)}$ of 0.84 MG.Oe (6.68 kJ/m^3) (Table 4.1). The incomplete exchange-coupling between the hard and the soft magnetic phases leads to a decrease in the H_{ci} in the nanocomposite powder compared to the parent hard magnetic phase.

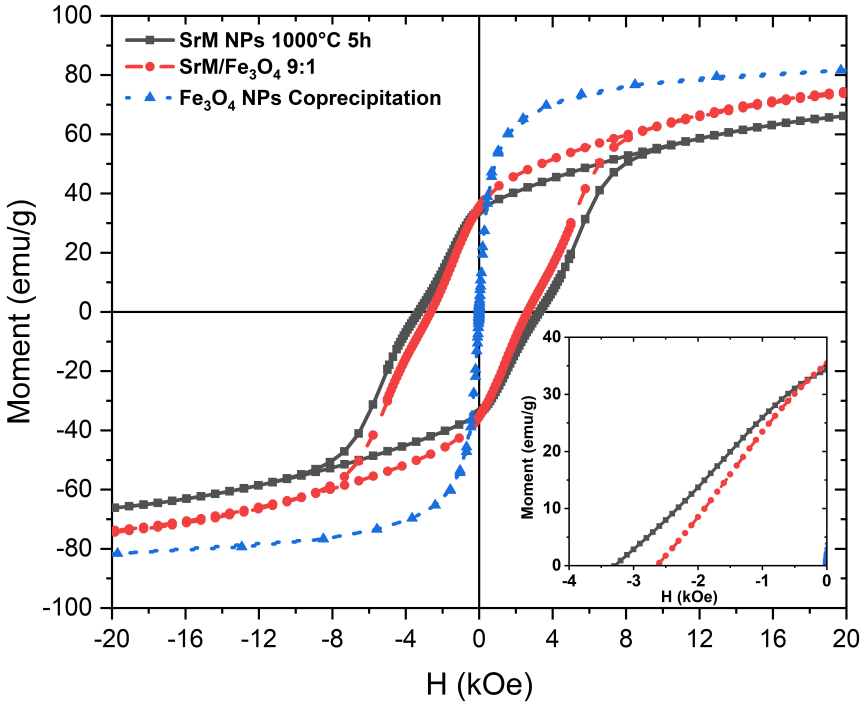

Fig. 4.19: Room temperature magnetic hysteresis (M–H) loops of the SrM powders calcined at 1000°C for 5 h, as-prepared Fe_3O_4 nanoparticles prepared via a coprecipitation method and as-coated SrM/Fe_3O_4 9:1 nanocomposite powder.

Figure 4.20 shows the SFD curves of the calcined SrM nanoparticles at 1000 °C for 5 h, the SrM/Fe_3O_4 9:1 nanocomposite and the Fe_3O_4 nanoparticles prepared by a coprecipitation method. The presence of a hump in the SFD peak of the calcined SrM (at high coercivity) is due to the shape anisotropy distribution of the nanoparticles which has also been observed in previous studies [112]. As for the nanocomposite sample, the dM/dH curve exhibits a distinct peak at $\sim$ 0 Oe, which is due to the uncoupled or weak coupling between the soft and the hard magnetic phases.

Table 4.1 summarises the magnetic properties of the investigated samples, com-

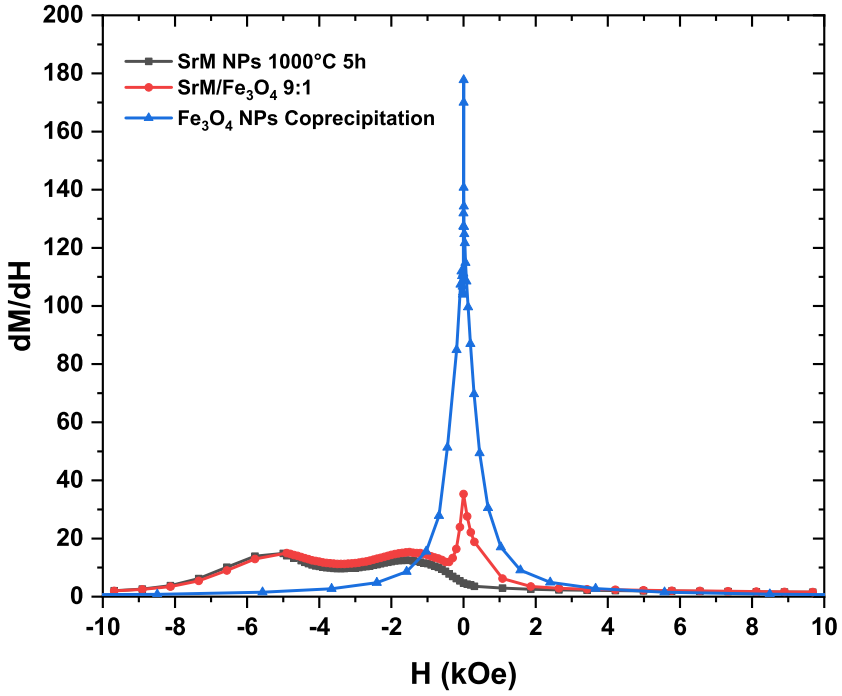

Fig. 4.20: Switching field distribution curves (dM/dH of demagnetisation curves) of the SrM nanoparticles calcined at 1000 °C for 5 h, as-prepared Fe_3O_4 nanoparticles via a coprecipitation method and SrM/Fe_3O_4 9:1 nanocomposite powder.

paring also our results with a commercial BaM powder and previous studies on the BaM/Fe_3O_4 exchange-coupled nanocomposite magnets [55, 56].

4.5 Summary

Flake-like single phase BaM and SrM nanoparticles were synthesised using a sol-gel auto-combustion method followed by a heat treatment process. X-ray diffraction analysis and magnetic measurements guided the optimisation of the annealing conditions. BaM/Fe_3O_4 and SrM/Fe_3O_4 core-shell-like nanocomposite powders were successfully prepared by coating the BaM and SrM nanoparticles with magnetite nanoparticles via a hydrothermal and a coprecipitation method respectively. The structural analysis confirms the presence of both phases. Exchange-coupling behaviour was observed between the hard/soft magnetic phases which leads to an increase in M_s and $BH_{(max)}$ of the nanocomposite samples compared to their parent hard magnetic phase. Unlike

Table 4.1: The magnetic properties of the investigated nanoparticles and nanocomposite samples and the commercial BaM powder, as well as data from Refs [55, 56].

	M_s (emu/g = A m^2/kg)	H_{ci} (kOe)	H_{ci} (kA/m)	M_r/M_s	$BH_{(max)}$ (MG.Oe)	$BH_{(max)}$ (kJ/m^3)
Fe_3O_4 Hydrothermal	91	< 0.05	< 4	0.04	0.002	0.02
BaM 1000 °C 5 h	61	3.56	283	0.49	0.74	5.89
BaM/Fe_3O_4 9:1	86	3.58	285	0.45	1.1	9.07
BaM/Fe_3O_4 3:1	87	2.47	197	0.39	0.54	4.30
BaM/Fe_3O_4 1:1	89	0.52	41	0.20	0.08	0.64
Commercial BaM	68	2.82	224	0.67	0.96	7.64
[55] Hydrothermal BaM/Fe_3O_4 nanocomposite	~ 60	~ 0.2	~ 16	-	-	-
[56] Mixed powder BaM/Fe_3O_4 nanocomposite	37	3.17	252	0.33	-	-
Fe_3O_4 Coprecipitation	85	< 0.05	< 4	0.04	0.002	0.02
SrM 1000 °C 5 h	71	3.29	261	0.49	0.77	6.12
SrM/Fe_3O_4 9:1	80	2.63	210	0.45	0.84	6.68

previous studies on the exchange-coupling of BaM and Fe_3O_4 nanoparticles [55, 56], the results demonstrate that an additional post-heat treatment is not required, which reduces the cost and simplifies the preparation process. These low cost core-shell-like nanocomposite powders with improved permanent magnetic properties, high resistivity and chemical stability could potentially be densified and used as bulk permanent magnets in a variety of applications.

Chapter 5

Bonded Ferrite-Based Exchange-Coupled Nanocomposite Magnets

Resin bonded magnets are among the most commercially fabricated permanent magnets due to their low cost of preparation, lightweight structure and their low processing temperatures. They are produced from different types of polymers such as thermoplastic (e.g. polycarbonate, nylon, polyethylene) or thermoset materials (e.g. epoxy, phenolic or polyester resins), as the "matrix" can be mixed with a wide range of different hard magnetic powders and by different manufacturing techniques [58–61]. These polymer matrix composite magnets exhibit interesting thermal, electrical, magnetic and mechanical properties, which make them suitable for a variety of applications [62–64]. In order to form complex geometries in sintered permanent magnets, several manufacturing processes, such as cutting, machining and grinding steps are needed, which leads to the waste of magnetic materials and have limitations in the geometric complexity of final products [64]. On the other hand, bonded magnets can be fabricated in different shapes and sizes through injection moulding, extrusion moulding or compaction moulding processes.

Resin bonded exchange-coupled BaM/Fe_3O_4 and SrM/Fe_3O_4 composite magnets were prepared via a warm compaction procedure with an epoxy resin. The effects of compaction conditions, as well as the ferrite concentration in the bonded magnets on

their mechanical, magnetic and structural properties are investigated. Results show an enhancement of $BH_{(max)}$ in the exchange-coupled ferrite-based bonded magnets compared to a commercial magnet, with optimised mechanical properties.

The chapter is organised as follows: in Sec. 5.1, the preparation procedures of ferrite-based bonded composite magnets together with the morphological characterisation of the prepared magnets are presented; in Sec. 5.2 the effect of compaction pressure and the ferrite concentration on the density of the bonded magnets is presented; in Sec. 5.3, the mechanical stability of the bonded magnets is explored; in Sec. 5.4, the effect of ferrite concentrations and warm compaction parameters on the magnetic properties of the bonded magnets are presented. Finally, in Sec. 5.5, a summary of the results is provided.

5.1 Morphological characterisation of the Bonded Magnets

The prepared composite powders of BaM/Fe_3O_4 (magnetite from hydrothermal process) and SrM/Fe_3O_4 (magnetite from coprecipitation process), with mass ratios of 9:1, were mixed with epoxy resin powder to obtain 80 % to 95 % mass ratios, and warm pressed in the range of 300-700 MPa. During the warm compaction process, the epoxy resin forms a thin layer around the powder and bonds the magnet after the curing process. Epoxy powders are used as the bonding agent due to their excellent adhesion, flexibility, hardness and chemical resistance [113]. SEM was used for morphological characterisation of the bonded magnets. Figure 5.1 shows the SEM images of epoxy bonded SrM/Fe_3O_4 composite magnets pressed at 300 MPa with the ferrite components of 80 wt.% and 95 wt.%. The SEM images confirm that the epoxy resin was uniformly distributed in the composite. However, increasing the ferrite powder component from 80 wt.% to 95 wt.% in the composite, causes the formation of microcracks (Figure 5.1(b-d)). The cross section SEM (Figure 5.1(d)) shows in-depth propagation of these microcracks, which can affect the mechanical properties of the bulk magnet. Figure 5.2 shows the SEM images of the surfaces of epoxy bonded BaM/Fe_3O_4 composite magnets pressed at 300 MPa with the ferrite powder components of 80 wt.% and 95

wt.%. The presence of microcracks in the epoxy bonded BaM/Fe_3O_4 composite with the ferrite concentration of 95 wt.% confirms the presence of an excessive amount of ferrite volume (95 wt.% in the composite magnet) in both BaM/Fe_3O_4 and SrM/Fe_3O_4 -based magnets.

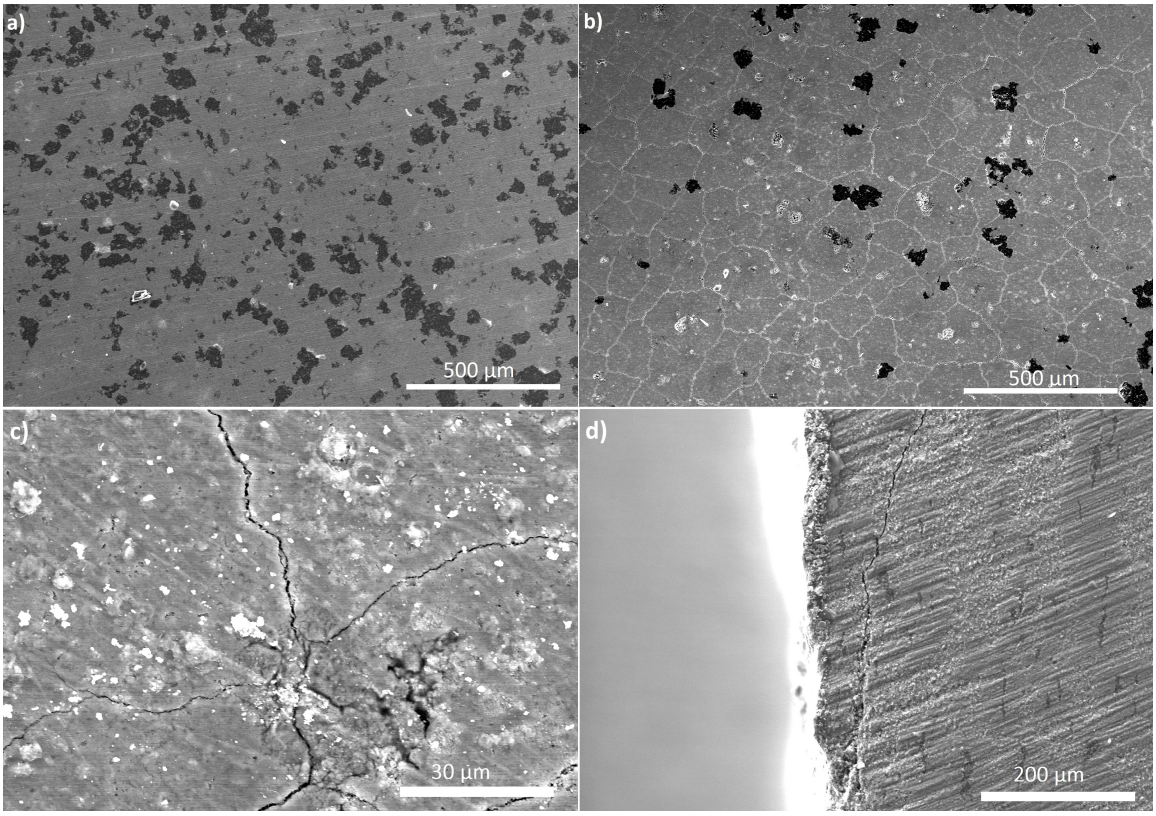

Fig. 5.1: SEM images of the epoxy bonded SrM/Fe_3O_4 composite warm pressed at 300 MPa with a ferrite powder component of (a) 80 wt.%, (b-c) 95 wt.% and (d) cross section SEM image of SrM/Fe_3O_4 composite with 95 wt.% ferrite content.

5.2 Density of the Bonded Magnet

Figure 5.3 shows the effect of compaction pressure and the ferrite powder component on the density of the bonded magnet. Due to the higher density of BaM over SrM, the density of BaM/Fe_3O_4 bonded magnets are slightly higher than those of the SrM based magnets. Also, the increase in the ferrite powder component in the bonded magnets causes an increase in the density of the bonded magnet. The density of the solid constituent of the bonded magnets are 5.28 g/cm^3 for BaM, 5.18 g/cm^3 for SrM, 5.18

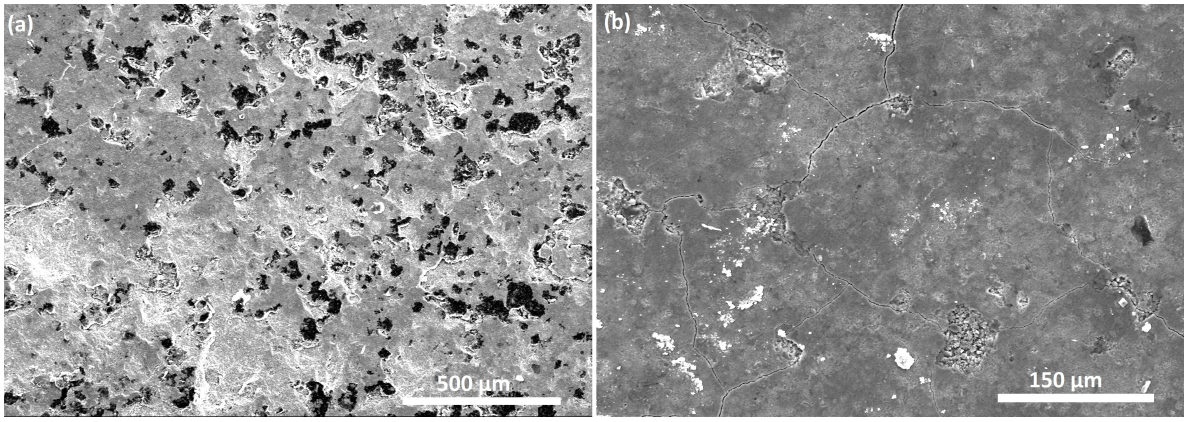

Fig. 5.2: SEM images of the epoxy bonded BaM/Fe_3O_4 composite warm pressed at 300 MPa with a ferrite powder component of (a) 80 wt.% and (b) 95 wt.%.

g/cm^3 for the soft ferrite Fe_3O_4 [109] and 1.29 g/cm^3 for the cured epoxy. The values of density of the bonded magnets in Figure 5.3(a) and (b) corresponds to porosities of 24-30 vol% in the BaM/Fe_3O_4 magnets and 27-30 vol% in SrM/Fe_3O_4 magnets respectively. Porosity is caused by closed bubbles of air in the epoxy and voids in the ferrite nanoparticle packing. The density values show no significant improvement in the density of the bonded magnets by increasing the compaction pressure from 300 MPa up to 700 MPa. However, the excessive compaction pressure might cause a slight decrease in the density due to the formation of cracks in the samples prepared at high pressures.

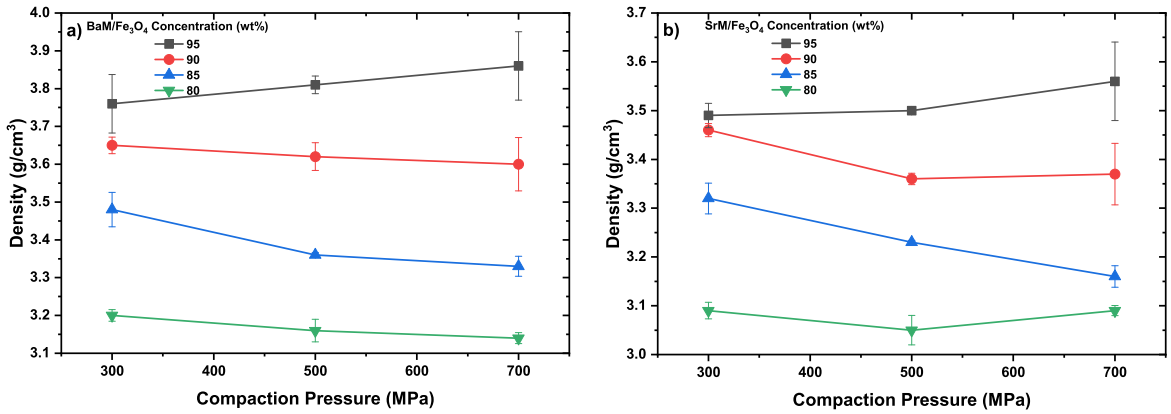

Fig. 5.3: Variation of density with compaction pressure and powder to resin ratio of (a) the epoxy bonded BaM/Fe_3O_4 composite magnet and (b) the epoxy bonded SrM/Fe_3O_4 composite magnet.

5.3 Mechanical Stability of the Bonded Magnets

In order to compare the mechanical stability of the prepared bonded magnets, Vickers hardness tests with 2 kgf were performed on the bulk samples. Figure 5.4 shows the variation of Vickers hardness with the compaction pressure and the ferrite concentration in bulk samples for both exchange-coupled BaM/Fe_3O_4 and SrM/Fe_3O_4 based magnets. At least 3 different measurements were performed on each sample with the average shown in Figure 5.4. The results indicate that in general, the SrM/Fe_3O_4 based bonded magnets are harder than BaM/Fe_3O_4 based bonded magnets, and the samples with ferrite concentration of 90 wt.% prepared at 500 MPa for BaM/Fe_3O_4 and 700 MPa for SrM/Fe_3O_4 ferrites have maximised mechanical stability with the hardness of $\sim$ 75 HV2 and $\sim$ 90 HV2, respectively. The hardness test could not be performed on some of the samples with 95 wt.% ferrite content due to microfracture and loss of mechanical stability (dark regions in Figure 5.4).

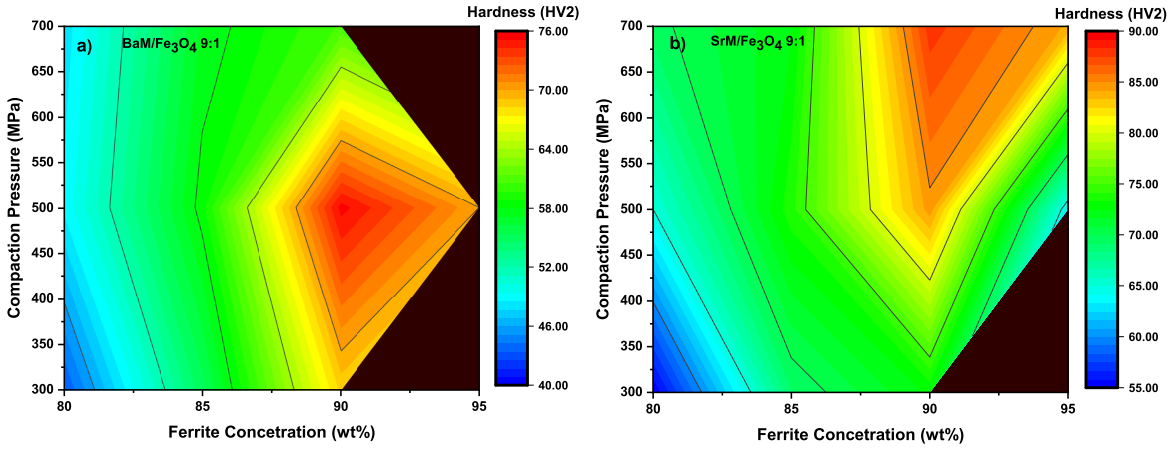

Fig. 5.4: Variation of Vickers hardness with compaction pressure and powder to resin ratio of (a) the epoxy bonded BaM/Fe_3O_4 composite magnet and (b) the epoxy bonded SrM/Fe_3O_4 composite magnet.

5.4 Magnetic Properties of the Bonded Magnets

Figure 5.5 shows the room temperature magnetic hysteresis curves of the BaM/Fe_3O_4-based bonded magnets with different ferrite concentrations and warm compaction pres-

sures compared to their parent exchange-coupled BaM/Fe_3O_4 nanocomposite phase. It is shown that the values of intrinsic coercivity of the bonded magnets are slightly smaller than their parent nanocomposite phase and the compaction pressure and ferrite concentration has a small effect on the coercivity of the bonded magnets.

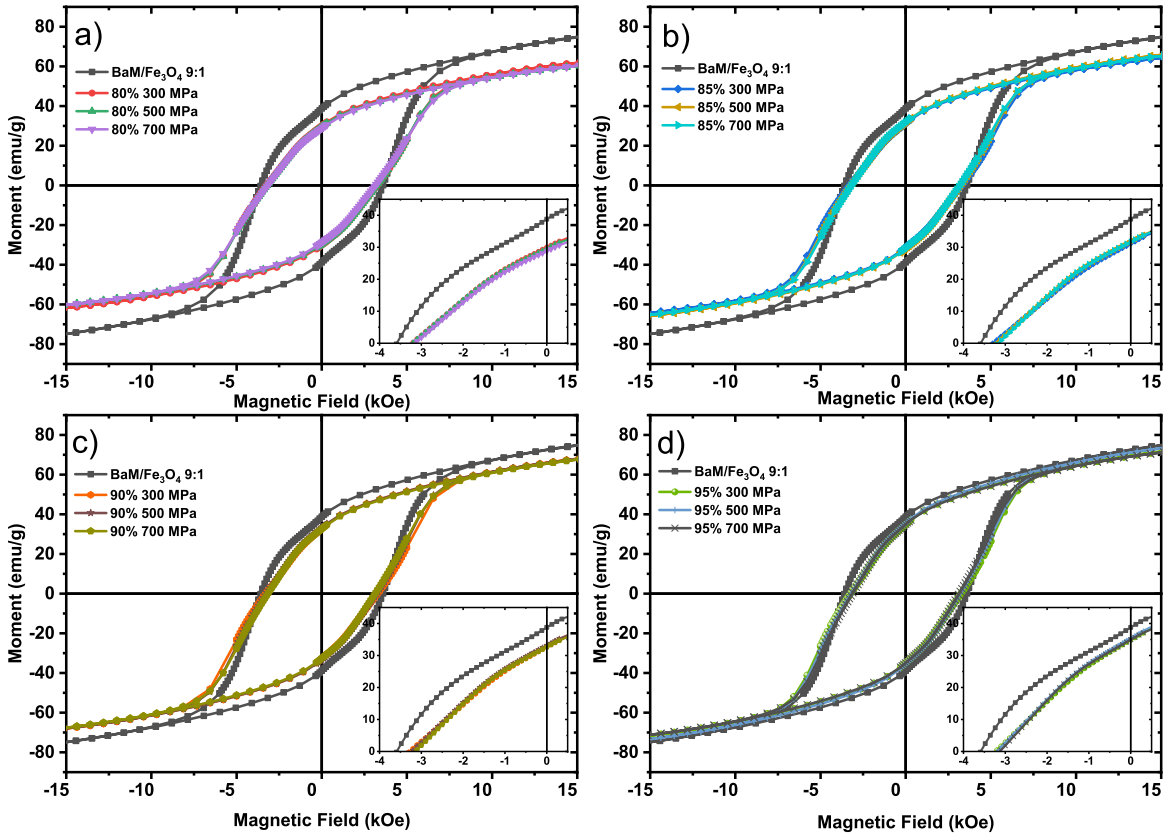

Fig. 5.5: Room temperature *MH* curves of the BaM/Fe_3O_4-based bonded magnets with different ferrite concentrations and warm compaction pressures compared to the parent exchange-coupled BaM/Fe_3O_4 nanocomposite powder. The inset shows the demagnetisation curve of the BaM/Fe_3O_4-based bonded magnets with different concentrations all prepared at 300 MPa.

Figure 5.6 shows the room temperature magnetic hysteresis curves of the SrM/Fe_3O_4-based bonded magnets with different ferrite concentrations and warm compaction pressures compared to their parent exchange-coupled SrM/Fe_3O_4 nanocomposite phase and a commercial SrM-based bonded magnet. The *MH* curves show that the intrinsic coercivity of the bonded magnets are slightly larger than their parent nanocomposite phase and the commercial SrM-based bonded magnet. It is shown that

the compaction pressure and ferrite concentration have a small effect on the coercivity of the bonded magnets.

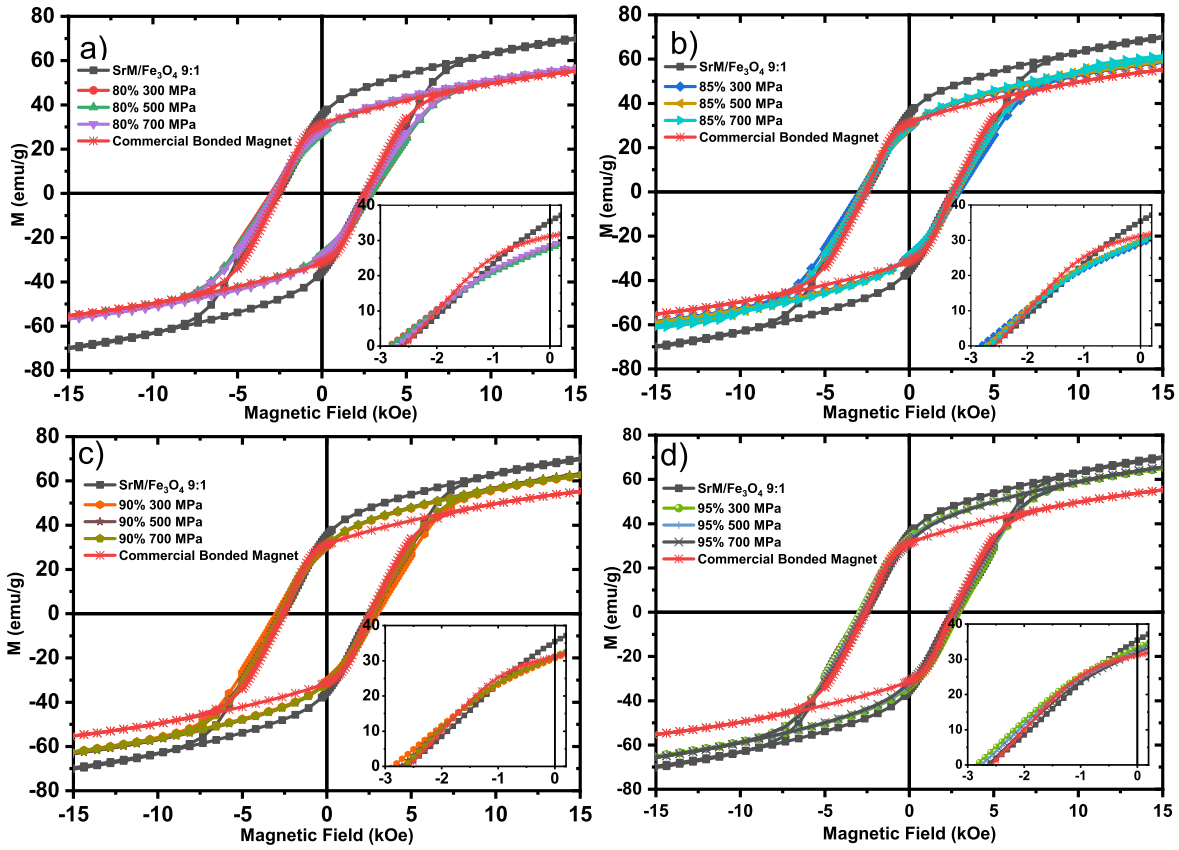

Fig. 5.6: Room temperature *MH* curves of the BaM/Fe_3O_4-based bonded magnets with different ferrite concentrations and warm compaction pressures compared to the parent exchange-coupled SrM/Fe_3O_4 nanocomposite powder. The inset shows the demagnetisation curve of the SrM/Fe_3O_4-based bonded magnets with different concentrations all prepared at 300 MPa.

Figure 5.7 gives a detailed magnetic characterisation of the bonded magnets for more in-depth investigation of the effect of compaction pressure and ferrite concentration on the hard magnetic properties of the bonded magnets. The magnetic measurements on the bonded magnets indicate that the warm compaction pressure has little effect on the $BH_{(max)}$ of the bonded magnets (Figure 5.7 (a)). However, the $BH_{(max)}$ of the exchange-coupled bonded magnet could be improved by up to $\sim$ 60 % (up to 0.8 MG.Oe (6.36 kJ/m^3)) for BaM/Fe_3O_4 and up to $\sim$ 50 % (up to 0.55 MG.Oe (4.38 kJ/m^3)) for SrM/Fe_3O_4 by increasing the ferrite concentration from 80 wt.% to

95 wt.%. BaM/Fe_3O_4 based bonded magnets show larger M_s and H_{ci} values than the SrM/Fe_3O_4 based bonded magnets. In both types of the bonded magnets, M_s increases with the increase of ferrite concentration (Figure 5.7(b-c)). Figure 5.7(b) shows that the ferrite concentration has no significant effect on the H_{ci} of the bonded magnets. The samples prepared at higher warm compaction pressure show smaller H_{ci} than those prepared at lower pressure. Magnetic measurements on a commercial bonded SrM magnet with $\sim$ 85 wt% SrM content show an H_{ci} of 2.85 kOe (227 kA/m), M_s of 63 emu/g (63 Am^2/kg) and $BH_{(max)}$ of 0.38 MG.Oe (3.0 kJ/m^3). Present magnetic measurements show that the $BH_{(max)}$ of the exchange coupled BaM/Fe_3O_4 and SrM/Fe_3O_4 bonded magnets are up to 120% and 45% larger than those of the commercial bonded SrM magnet, respectively.

Table 5.1 summarises the magnetic properties of the exchange-coupled SrM/Fe_3O_4 and BaM/Fe_3O_4 nanocomposite powders and their parent hard and soft magnetic phases, as well as a comparison between our investigated exchange-coupled ferrite based bonded magnets with a commercial SrM based bonded magnet.

5.5 Summary

Bonded ferrite-based composite magnets were prepared via a warm compaction process at 180°C for 10 *min* at different compaction pressures. The exchange-coupled magnetite coated BaM and SrM nanocomposites were used as the magnetic filler. Epoxy powder was used as the matrix in the composite magnet.

The density measurements on the bonded composite magnets show an increase in the density with the increase of the ferrite concentration in the composite. No significant improvement in the density by increasing the compaction pressure from 300 MPa up to 700 MPa was observed. The excessive compaction pressure actually causes a slight decrease in the density due to the formation of cracks in the samples prepared at high pressures, which could be observed in the SEM images. Vickers hardness tests indicate that the samples with ferrite concentration of 90 wt.% prepared at 500 MPa for BaM/Fe_3O_4 and 700 MPa for SrM/Fe_3O_4 ferrites have maximised mechanical stability. Magnetic measurements on the bonded magnets show that $BH_{(max)}$ of the exchange

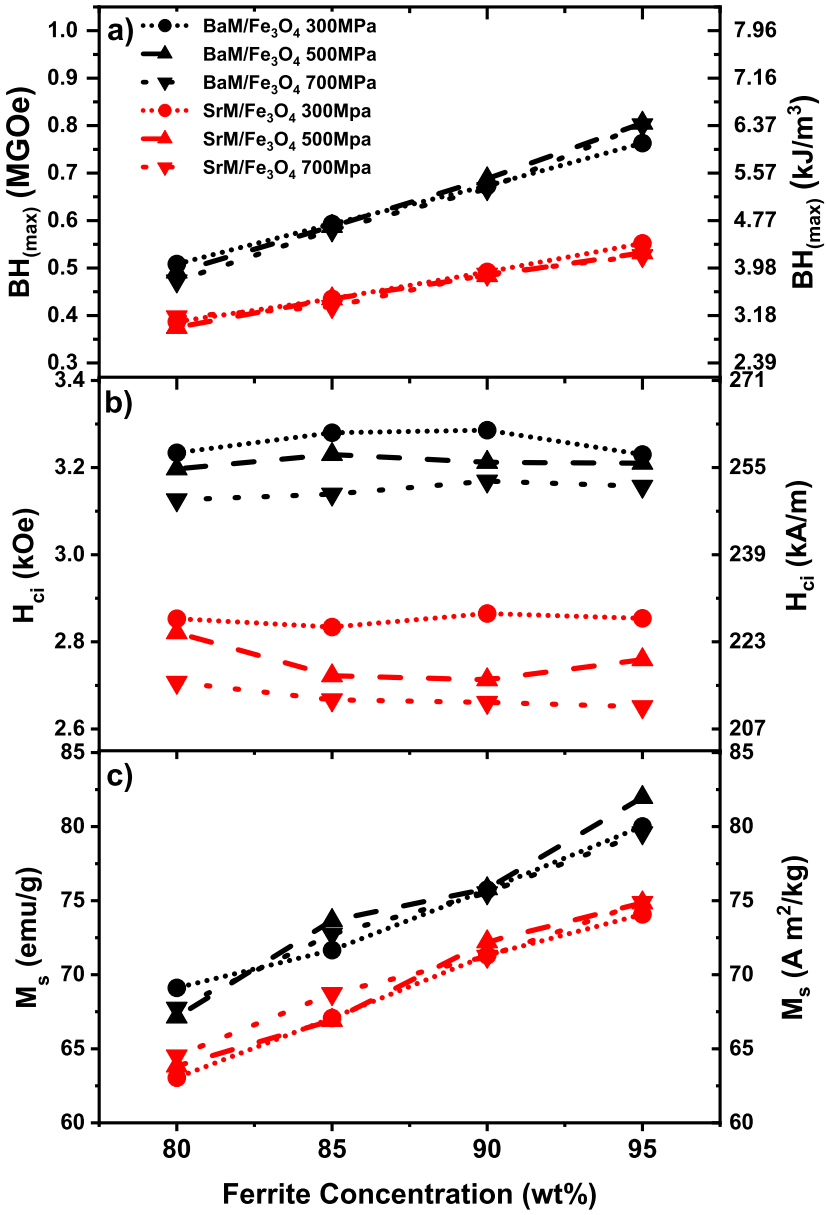

Fig. 5.7: Variations of (a) $BH_{(max)}$, (b) H_{ci} and (c) M_s, with compaction pressure and powder to resin ratio of the epoxy bonded BaM/Fe_3O_4 and SrM/Fe_3O_4 composite magnet.

coupled BaM/Fe_3O_4 and SrM/Fe_3O_4 bonded magnets is up to 120% and 45% greater than the values in a commercial bonded SrM magnet of comparable powder to polymer ratio, respectively. We observed that the increase in the SrM/Fe_3O_4 concentration from 80 to 95 wt.% in the composite magnet causes an improvement in the maximum energy product. In the BaM/Fe_3O_4 magnets, the $BH_{(max)}$ increases significantly with

Table 5.1: A comparison between magnetic properties of our investigated samples with a commercial SrM based bonded magnet.

	M_s (emu/g = A m^2/kg)	H_{ci} (kOe)	H_{ci} (kA/m)	M_r/M_s	$BH_{(max)}$ (MG.Oe)	$BH_{(max)}$ (kJ/m^3)
Fe_3O_4 Hydrothermal *	91	< 0.05	< 4	0.04	0.002	0.02
BaM 1000 °C 5 h *	61	3.56	283	0.49	0.74	5.89
BaM/Fe_3O_4 9:1 *	86	3.58	285	0.45	1.1	9.07
Fe_3O_4 Coprecipitation *	85	< 0.05	< 4	0.04	0.002	0.02
SrM 1000 °C 5 h *	71	3.29	261	0.49	0.77	6.12
SrM/Fe_3O_4 9:1 *	80	2.63	210	0.45	0.84	6.68
SrM/Fe_3O_4 bonded magnet (85 wt% 300 MPa)	68	2.83	225	0.44	0.44	3.50
SrM/Fe_3O_4 bonded magnet (95 wt% 300 MPa)	75	2.85	227	0.44	0.55	4.38
BaM/Fe_3O_4 bonded magnet (85 wt% 300 MPa)	74	3.28	261	0.43	0.59	4.69
BaM/Fe_3O_4 bonded magnet (95 wt% 300 MPa)	82	3.23	257	0.43	0.80	6.37
Commercial SrM bonded magnet (85 wt%)	63	2.85	227	0.49	0.38	3.02

* data shown in Table 4.1 is here repeated for convenience.

the increase in the ferrite concentration. This might be due to the larger increase in the density of BaM/Fe_3O_4 compared to the SrM/Fe_3O_4 bonded magnets with the increase in the ferrite concentration. Our results show that the epoxy-bonded exchange-coupled SrM/Fe_3O_4 with the ferrite concentration of 95 wt.% compressed at 700 MPa and the BaM/Fe_3O_4 with the ferrite concentration of 90 wt.% compressed at 500 MPa have optimised magnetic and mechanical properties.

Chapter 6

Micromagnetic Simulations on the Ferrite Based Nanocomposites

To better understand and support the experimental data of the magnetic properties of the nanocomposite powders, computational simulations of the exchange coupling behaviour of the BaM/Fe_3O_4 hard-soft magnetic nanocomposites and the response of these nanocomposites to an external magnetic field to obtain their hysteresis curves were carried out. The simulations were performed with a graphics processing unit (GPU)-accelerated micromagnetic simulation software MuMax^3 [114], which employs finite-difference discretisation.

6.1 Theory of Micromagnetism

Ferromagnetic materials show a hysteresis behaviour in the presence of an external magnetic field which is a consequence of short- and long-range spatial scale (ranging from nm to μm) interactions between the magnetic moments. These short-range interactions (anisotropy and exchange interactions) and long-range interaction (magnetostatic interactions) are described in terms of the free energy of the system.

6.1.1 Exchange Energy

The exchange interaction, which is a quantum mechanical phenomenon, takes into account the spin-spin interactions on a scale of atomic distances and tends to interact

with the neighbour spins which favours parallel alignment to each other [115]. The Heisenberg Hamiltonian [116] can be written as:

$$\hat{\mathrm{H}}_{spin} = -2JS_i \cdot S_j, \tag{6.1}$$

where S_i and S_j are the localized spins and J is the exchange constant between the spins i and j. For $J > 0$, the spins tend to a parallel state and the material shows ferromagnetic ordering. On the other hand, for negative values of J, the material would have an antiferromagnetic behaviour [117]. In a solid material, an exchange interaction exists between all the neighbouring atoms. By defining a unit vector m in the direction of $-S_i$, then $S_i = -Sm_i$, where S is the spin magnitude. By ignoring the discrete nature of the lattice of spins the Heisenberg Model can be written as:

$$\hat{\mathrm{H}} = -\sum_j JS \cdot S_j, \tag{6.2}$$

where the summation is over the nearest neighbours. Assuming the angle between the two neighbouring spins is very small, $\phi_{ij} << 1$ for all i and j, the energy of the system can be written as:

$$E_{exch} = -JS^2 \sum_{<ij>} \cos\phi_{ij} = \text{constant} + \frac{JS^2}{2} \sum_{<ij>} \emptyset_{ij}^2, \tag{6.3}$$

where the constant term can be ignored when all the spins are parallel. Considering m as the reduced magnetic moment, $m = \frac{M}{M_s}$, where M is the magnetisation and M_s is the saturation magnetisation we get $|\phi_{ij}| \approx |m_i - m_j|$ (Figure 6.1).

Given that reduced magnetisation does not vary from point to point,

$$|m_i - m_j| \approx| \, (r_{ij} \cdot \nabla)\, m \tag{6.4}$$

And the energy of the system can be written as:

$$E_{exch} = JS^2 \sum_{<ij>} \left[(r_{ij} \cdot \nabla)\, m\right]^2 \tag{6.5}$$

In a continuum limit, the summation can be replaced by an integral over the volume of the sample V,

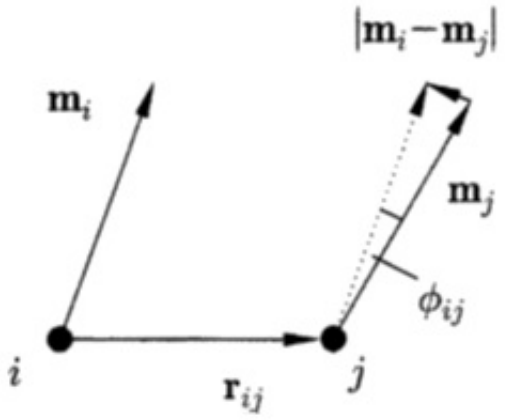

Fig. 6.1: The reduced magnetisation unit vectors at neighbouring sites i and j [117].

$$E_{exch} = A_s \int_V \left[(\nabla m_x)^2 + (\nabla m_y)^2 + (\nabla m_z)^2 \right] d^3r \tag{6.6}$$

By combining all the constant into a single material dependent term, A,

$$A_s = JS^2 c/a, \tag{6.7}$$

where A_s is the exchange stiffness of the material, a is the distance between the neighbouring spins and c is a constant depending on the crystalline structure. For example, $c = 1$, 2 and 4 for simple cubic and bcc and face centred cubic (fcc) systems respectively and $c = 4\sqrt{2}$ for hexagonal close packed (hcp) systems [118].

6.1.2 Anisotropy Energy

Due to the lattice structure and crystal symmetry, ferromagnetic materials tend to magnetise along a certain energy favoured direction when there is no external magnetic field, which is called the easy direction. It can be assumed that there is a force that tends to align the magnetisation along the easy direction. In micromagnetics this force is an important part of the total free energy. Considering a volume ΔV with uniform magnetisation M and m as the reduced magnetic moment:

$$m_x = \sin\theta \cos\phi \tag{6.8}$$

$$m_y = \sin\theta \sin\phi \tag{6.9}$$

$$m_z = \cos\phi, \tag{6.10}$$

where θ and ϕ are the polar and azimuthal angles, respectively. Then the free energy density can be expressed as:

$$E_{\text{anis}} = e_{\text{anis}}(m) \cdot \Delta V \tag{6.11}$$

We assume that $e_{\text{anis}}(m)$ is independent of m and defined as a constant. Different energy surfaces with different quantitative details can be obtained by choosing different values of this constant. The energy surfaces show some depressions which are energetically favoured and are called easy magnetisation axes. The solution of

$$\frac{\partial e_{anis}(m)}{\partial m} = 0 \tag{6.12}$$

gives local minima and maxima in the energy surface which are called easy and hard axes. Depending on the symmetry, there could be multiple easy axes in the system. However, most of the metallic systems have either uniaxial or cubic anisotropy [115, 117].

6.1.2.1 Uniaxial Anisotropy

In the case of uniaxial anisotropy, there is only one easy axis which is along the z-axis. The anisotropy energy is also rotationally symmetric. Therefore:

$$m_x^2 + m_y^2 = 1 - m_z^2 = \sin^2\theta \tag{6.13}$$

And the energy density is expressed as:

$$E_{\text{anis}} = K_0 + K_1 \sin^2\theta + K_2 \sin^4\theta, \tag{6.14}$$

where K_0, K_1, and K_2 are the anisotropy constants with the unit of J/m^3. Figure 6.2 shows the uniaxial anisotropy energy density when $K_1 > 0$ and $K_1 < 0$.

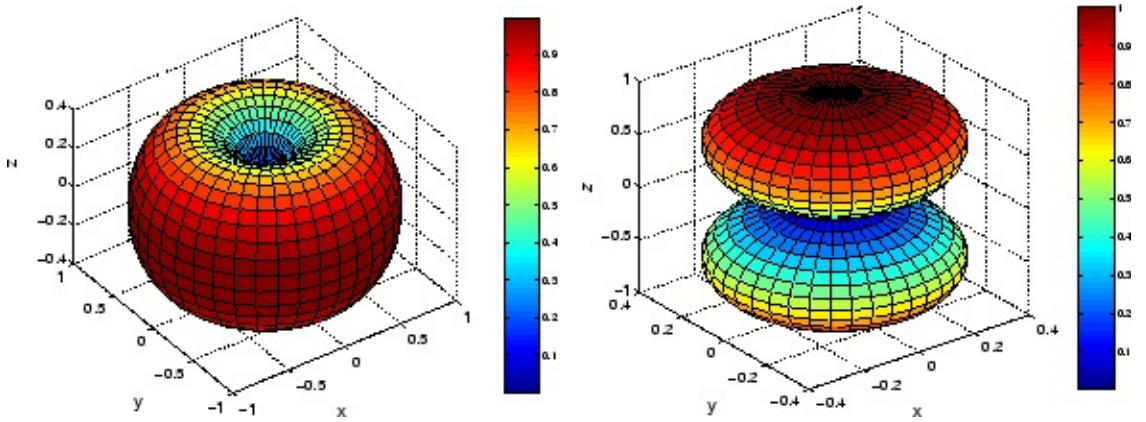

Fig. 6.2: Uniaxial anisotropy energy density when $K_1 > 0$ (right) and $K_1 < 0$ (left) [119].

6.1.2.2 Cubic Anisotropy

Due to spin-lattice coupling in cubic crystals, there are 3 easy axes in a cubic anisotropy which are along x, y, and z -axes. The anisotropy energy density can be expressed as:

$$E_{\text{anis}} = K_0 + K_1(m_x^2 m_y^2 + m_y^2 m_z^2 + m_z^2 m_x^2) + K_2 m_x^2 m_y^2 m_z^2 \tag{6.15}$$

Figure 6.3 shows the cubic anisotropy energy density when $K_1 > 0$ and $K_1 < 0$.

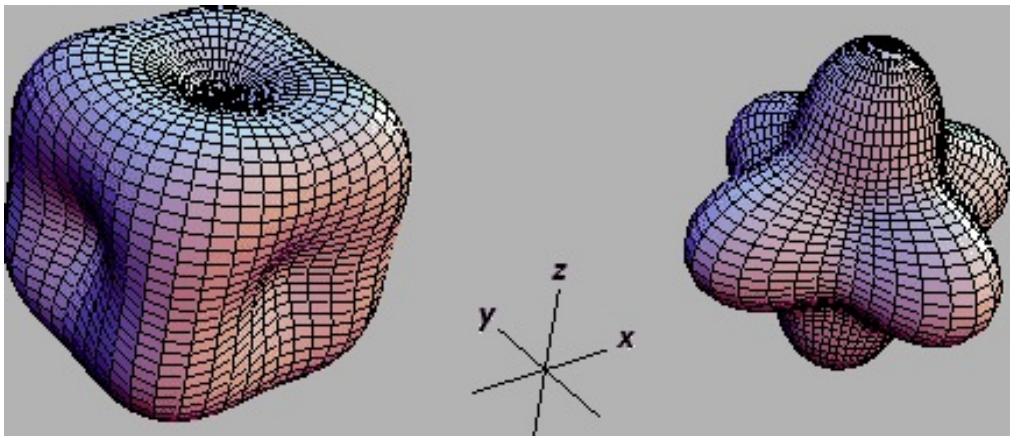

Fig. 6.3: Cubic anisotropy energy density when $K_1 > 0$ (right) and $K_1 < 0$ (left) [120].

6.1.3 External Field (Zeeman) Energy

The term external field energy represents the energy cost of misalignment between the magnetic moment of the sample and an applied magnetic field H. By considering a

single spin with magnetic moment μ in an external field, the Hamiltonian would be:

$$\hat{\mathrm{H}} = -\mu_0 \mu \cdot H \tag{6.16}$$

In the continuum approximation, the total Zeeman energy for a sample in a magnetic field is [117]:

$$E_{\text{Zeeman}} = -\mu_0 \int H \cdot M dV = -\mu_0 M_s \int H \cdot m dV \tag{6.17}$$

6.1.4 Stray (Demagnetising, Magnetostatic) Field Energy

The magnetic moments of the sample create a magnetic field inside the bulk which opposes the external field. This energy term is called demagnetising energy and can be calculated by replacing the demagnetising field (H_d) in Zeeman energy formula (equation 6.17). According to Maxwell's equation:

$$\nabla \cdot H_d = -\nabla \cdot M \tag{6.18}$$

$$\nabla \times H_d = 0 \tag{6.19}$$

Then the demagnetising energy can be expressed as [117]:

$$E_{\text{demag}} = \frac{1}{2}\mu_0 \int_{\text{all space}} H_d \cdot M dV = -\frac{1}{2} M_s \int_{\text{sample}} H_d \cdot m dV \tag{6.20}$$

6.1.5 Micromagnetic Equations

By summing up all the energy contribution terms mentioned before the total energy of a ferromagnetic body can be obtained. Considering $M = M_s \cdot m$ then

$$E_{\text{total}} = E_{\text{exch}} + E_{\text{anis}} + E_{\text{demag}} + E_{\text{Zeeman}} \tag{6.21}$$

$$E_{total} = \int_V \left[A_s (\nabla m)^2 + F_{anis}(m) - H_{ext} \cdot M + \frac{1}{2} H_d \cdot M \right] dV, \tag{6.22}$$

where F_{anis} is the energy term summing up all the contributions of magnetocrystalline anisotropy. The energy terms of magnetorestrictive effects and external stress in the sample have been omitted, due to the fact that they are incompatible with the simulation software [114]. Many variations of the total energy term with many constraints can be derived from this equation [121].

$$f_L \cdot m = -2A\Delta m + \nabla_m F_{anis}(m) - (H_{ext} + H_d)\, M_s \tag{6.23}$$

$$\nabla \cdot (\mu_0 H_d + M) = 0 \tag{6.24}$$

$$\nabla \times H_d = 0 \tag{6.25}$$

The term $f_L \cdot m$ can be written as -$M_s H_{eff}$, therefore:

$$H_{eff} = H_{ext} + H_d + \frac{1}{M_s}\left[2A_s\Delta m - \nabla_m F_{anis}(m)\right], \tag{6.26}$$

where H_{eff} is the effective field containing all the various magnetic components. In a static equilibrium

$$M \times H_{eff} = 0, \tag{6.27}$$

which shows that the torque on the magnetisation is zero at equilibrium. In a dynamic magnetisation equation, proposed by Landau and Lifshitz (LL) [122], the statement can be written as:

$$\frac{dm}{dt} = -\gamma m \times H_{eff}, \tag{6.28}$$

where γ is the gyromagnetic ratio of the electron. In this statement, no energy losses have been taken into account. By including an additional term that describes local dissipative phenomena, the Landau-Lifshitz-Gilbert (LLG) equation [123] is obtained:

$$\frac{dm}{dt} = -\gamma_{LL} m \times H_{eff} + \alpha_{LL} m \times (m \times H_{eff}) \tag{6.29}$$

$$\gamma_{LL} = \frac{\gamma}{1 + \alpha_G^2} \tag{6.30}$$

$$\alpha_{LL} = \frac{\gamma \alpha_G}{1 + \alpha_G^2}, \tag{6.31}$$

where α_G is the Gilbert damping coefficient. Using this expression in a micromagnetic simulation, it is possible to obtain the equilibrium state of a magnetic system and evaluate the magnetic body under several time-dependent perturbations.

6.2 MuMax^3: Numerical Method, Features and Capabilities

The open source micromagnetic simulation program MuMax^3, written in Go [124] and using Cuda platform [125], allows the computation of magnetisation response to an applied magnetic field as well as magnetisation dynamics. The software employs the GPU, due to its excellent capability for parallelisation which leads to much faster simulations compared to CPU-based programs (i.e. OOMMF [126]). MuMax^3 uses a finite difference (FD) discretisation of space and a 2D or 3D grid of orthorhombic cells (Figure 6.4) and uses the following form of the Landau-Lifshitz-Gilbert equation [123]:

$$\tau_{LL} = \gamma_{LL} \frac{1}{1 + \alpha^2} \left(m \times H_{eff} + \alpha \left(m \times \left(m \times H_{eff} \right) \right) \right), \tag{6.32}$$

where $\tau_{LL} = \frac{dm}{dt}$ is the torque, γ_{LL} the gyromagnetic ratio and α is the dimensionless damping parameter.

In MuMax^3 the components of the effective field are calculated as follows:

1. Magnetostatic Field

$$H_{\text{demag}}^{(i)} = K_{ij} \cdot M_i \tag{6.33}$$

Then,

$$E_{\text{demag}} = -\frac{1}{2} M \cdot H_{\text{demag}} \tag{6.34}$$

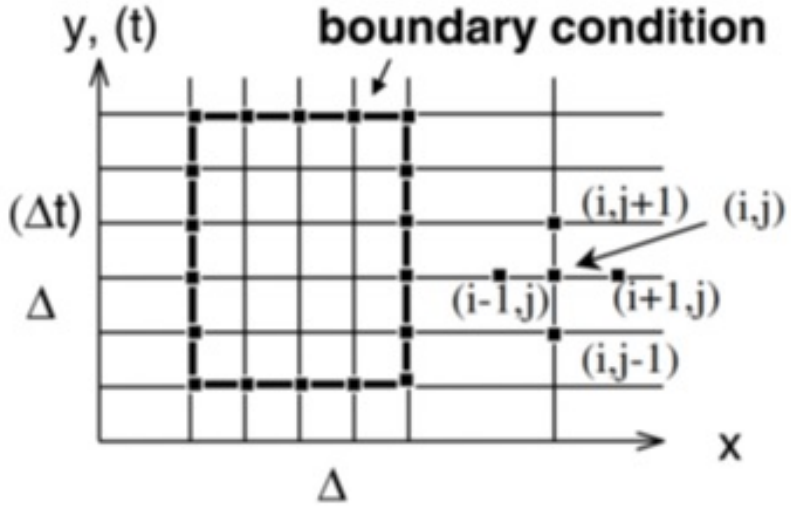

Fig. 6.4: Schematic of a 2D FD discretisation of space [127].

with the possibility of using periodic boundary conditions (PBC), which allows the magnetisation to wrap around in 3 directions.

2. Exchange Interaction Energy

$$H_{exch} = 2\frac{A_s}{M_{sat}} \sum_i \frac{(m_i - m)}{\Delta x_i}, \tag{6.35}$$

where index i is between the 6 nearest neighbours and Δx_i is the spatial separation between m_i and m then the exchange interaction energy becomes,

$$E_{exch} = -\frac{1}{2} M \cdot H_{exch} \tag{6.36}$$

3. Magnetocrystalline Anisotropy

In the uniaxial anisotropy,

$$H_{\text{anis}} = \frac{2K_{u1}}{H_{\text{sat}}}(u \cdot m)u + \frac{4K_{u2}}{H_{\text{sat}}}(u \cdot m)^3 u, \tag{6.37}$$

where u is the anisotropy vector. Then,

$$E_{\text{anis}} = -\frac{1}{2} H_{\text{anis}}\left(K_{u1}\right) - \frac{1}{4} H_{\text{anis}}\left(K_{u2}\right) M \tag{6.38}$$

In the cubic anisotropy the term K_{u2} is omitted.

6.3 Model Description

6.3.1 Barium Hexaferrite Grain Model

In order to produce the hysteresis curve of the BaM powder, the MuMax^3 extension, "ext_makegrains", was applied in the simulation code. The extension helps to produce grains with a controlled average size, which represent particles of BaM in the simulation model. Figure 6.5 shows an illustration of using 300 nm sized grains in XY plane and with various thicknesses. The model had a length of 1000 nm in both x and y directions and the thickness varied from 10 to 100 nm with grains having a random magnetocrystalline anisotropy direction resembling different particles. The magnetic field was applied in z direction (Hz) with the initial magnetisation set to random. The material parameters, magnetocrystalline anisotropy constant, $K_1 = 3.3 \times 10^5$ J/m^3, saturation magnetisation, $M_s = 3.82 \times 10^5$ A/m, and exchange stiffness constant, $A_s = 6.3 \times 10^{-12}$ J/m, were used in this simulation [109].

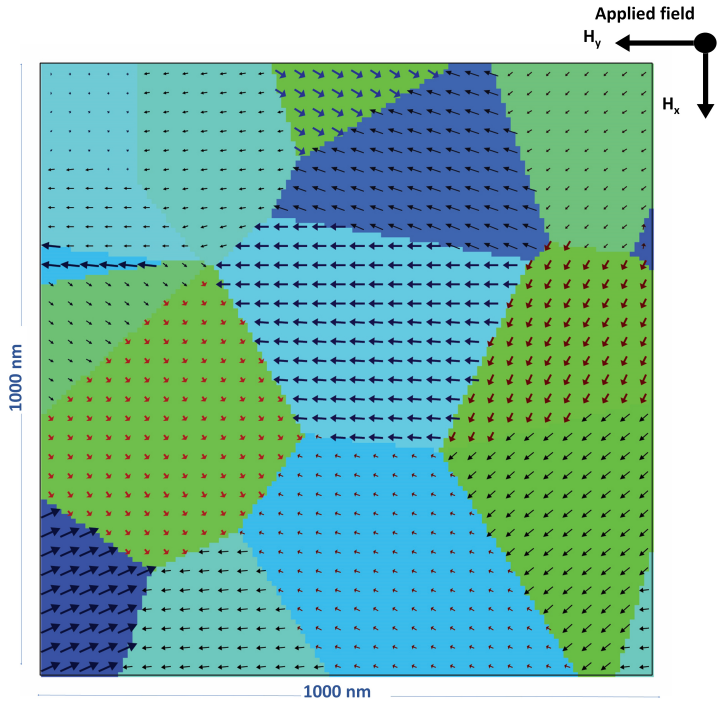

Fig. 6.5: BaM model with 300 nm grain size, which the magnetic field was applied in z direction (Hz). The initial magnetisation set to random. The arrows represent the magnetocrystalline anisotropy of each grain.

6.3.2 Magnetite Model

The magnetite part in the nanocomposite powder was simulated using two different approaches. In the first approach, 10 nm sized films of Fe_3O_4 with random magnetocrystalline anisotropy directions were simulated and in the second approach, the MuMax^3 extension, "ext_make3dgrains", was applied in the simulation code to produce 10 nm sized grains. This extension, made recently available in the MuMax^3 version 3.9C, helps to produce grains with an average size in 3 directions. As a result of this more uniformly sized particles, such as cubic and spherical particles, can be simulated. Figure 6.6 shows an illustration of using 10 nm sized films (Figure 6.6(a)) and 10 nm sized grains (Figure 6.6(b)). The material parameters, magnetocrystalline anisotropy constant, K_1 = -1.36 $\times$ 10^4 J/m^3, saturation magnetisation, M_s = 4.85 $\times$ 10^5 A/m, and exchange stiffness constant, A_s = 1.32 $\times$ 10^{-11} J/m, were used in this simulation [109].

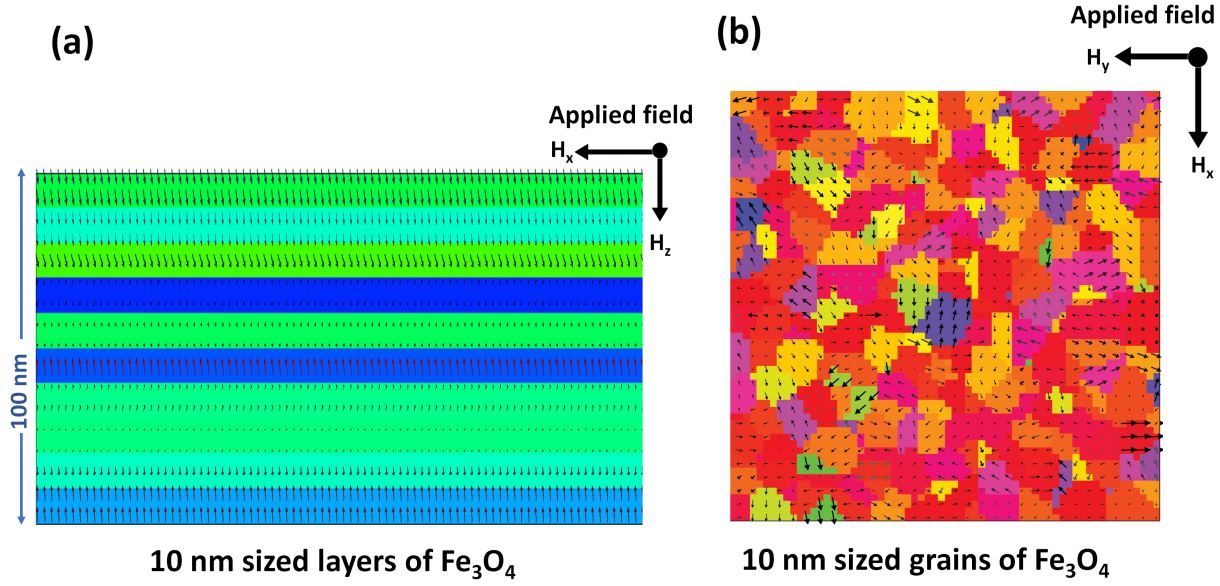

Fig. 6.6: Fe_3O_4 Model with (a) 10 nm sized layers and (b) 10 nm grain sized, to which the magnetic field was applied in z direction (Hz). The initial magnetisation set to random. The arrows represent the magnetocrystalline anisotropy of each grain.

6.3.3 Nanocomposite Model

In order to investigate the exchange-coupling effect in the BaM/Fe_3O_4 nanocomposites with MuMax^3, a model of multilayers of Fe_3O_4 coated BaM was simulated (Figure 6.7). The BaM part contains 300 nm sized grains with a 90 nm thickness and coated with 1, 2, or 3 layers of Fe_3O_4 films or nanoparticles. The exchange length (l_{ex}) is an important parameter in micromagnetic simulations, which defines the length of transition between the magnetic domains [128].

$$l_{ex} = \sqrt{\frac{2A}{\mu_0 M_s^2}} \tag{6.39}$$

The cell size was 2.5 × 2.5 × 2.5 nm^3 taking into consideration that the exchange length of BaM was around 5.8 nm and of Fe_3O_4 was around 4.9 nm [109]. The periodic boundary condition (PBC) of (3, 3, 10) in (x, y, z) direction was used in the simulation models.

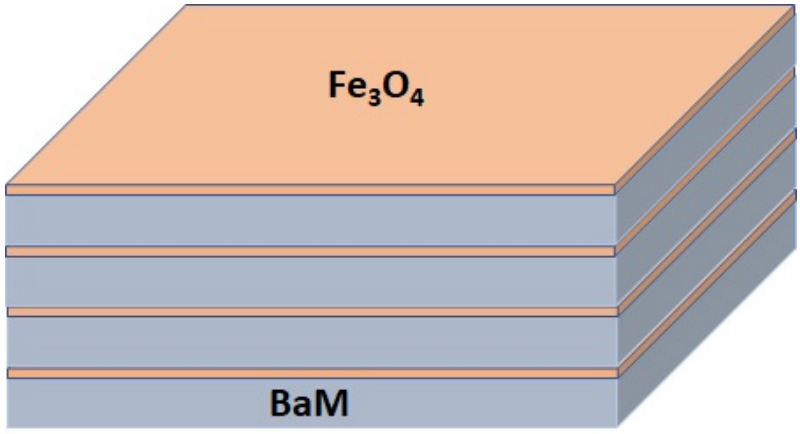

Fig. 6.7: Schematic of the model used for coated BaM with Fe_3O_4 layers. Each layer of BaM nanoparticles is coated with 1, 2, or 3 layers of Fe_3O_4 films or nanoparticles.

6.4 Simulation Results

6.4.1 Effect of Thickness on the Magnetic Properties of BaM

In order to investigate the the effect of the thickness of the flake-like BaM nanoparticles on their magnetic properties, and better describe their magnetic properties, compared

to experimental results, 300 nm sized grains BaM with various thicknesses, from 10 nm to 100 nm, were simulated. Figure 6.8 shows the simulated *MH* curves of the BaM grains. We previously reported that the BaM nanoparticles, prepared by a sol-gel autocombustion method and annealed at 1000 °C for 5 h, show an H_{ci} of $\sim$ 3.5 kOe and have an average particle size of $\sim$ 300 nm. The simulation results show that increasing the thickness of the BaM grains from 10 nm to 100 nm causes an increase in the H_{ci} from $\sim$ 3.25 kOe to $\sim$ 3.7 kOe, and the ones with 50 nm and 60 nm thicknesses have an H_{ci} of $\sim$ 3.5 kOe which is comparable to our experimental results (Figure 6.9).

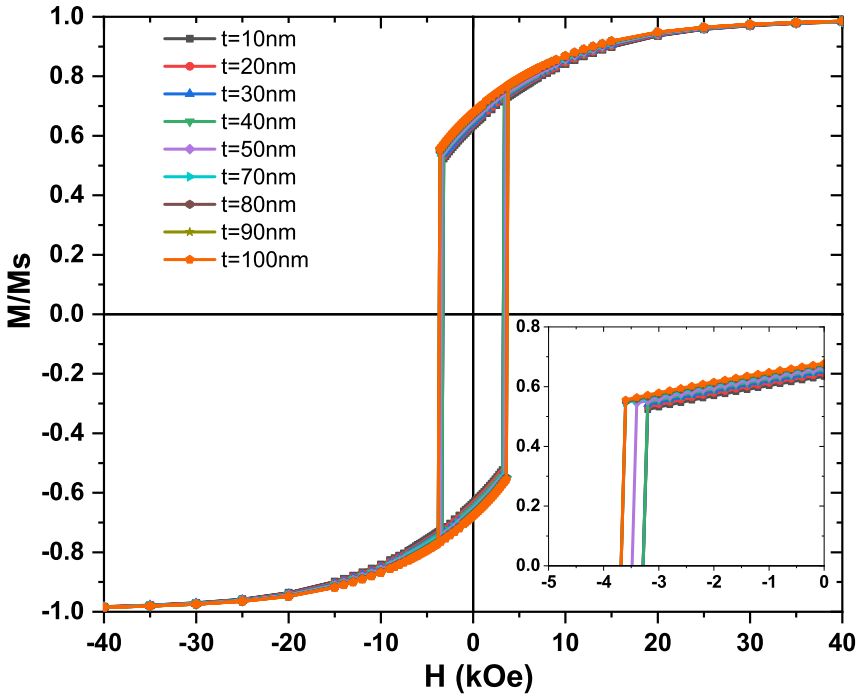

Fig. 6.8: *MH* curves of 300nm sized BaM grains with different thicknesses.

6.4.2 Fe_3O_4: Film vs Grains

In order to simulate the magnetite part of the exchange-coupled BaM/Fe_3O_4 nanocomposite, different approaches were examined, including 10 nm sized Fe_3O_4 films and 10 nm sized Fe_3O_4 grains. Figure 6.10 shows the simulated *MH* curves of both magnetite films and grains. Using the magnetite films, the hysteresis curves show a soft magnetic behaviour with an $H_{ci} < 0.4$ kOe. However, our previous experimental results show a superparamagnetic-like behaviour for the magnetite nanoparticles (Figure

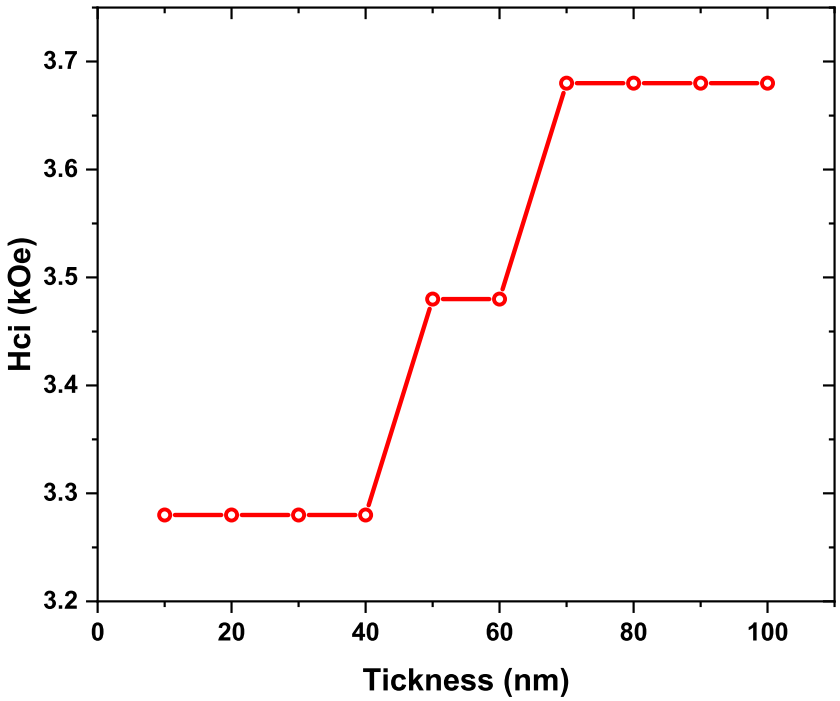

Fig. 6.9: Dependence of intrinsic coercivity on thickness of simulated 300 nm sized BaM grains.

4.10). In order to achieve the superparamagnetic behaviour in the magnetite part of the nanocomposite, 10 nm sized grains with negligible exchange interaction between grains [129] were simulated. The hysteresis curve confirms the superparamagnetic behaviour with $H_{ci} \approx 0$ kOe.

6.4.3 Nanocomposite Simulation

Taking into account the density values of BaM and Fe_3O_4, (5.28 g/cm^3 and 5.18 g/cm^3, respectively), and to simplify the simulations of composite with the same volume fraction as the produced samples, 1, 2 and 3 layers of 10 nm sized Fe_3O_4 are coated on a 90 nm thick layer of BaM with a PBC of (3, 3, 10) in (x, y, z) directions. This leads to simulation of BaM/Fe_3O_4 nanocomposites with 9:1, 9:2, and 9:3 volume ratios which are comparable with the weight ratios due to the proximity of the density of both magnetic phases. Even though the results of 10 nm thick magnetite films did not represent the experimental work, BaM/Fe_3O_4 nanocomposites with a continuous film of Fe_3O_4 were simulated. Figure 6.11 shows the hysteresis curves of up to 3 layers

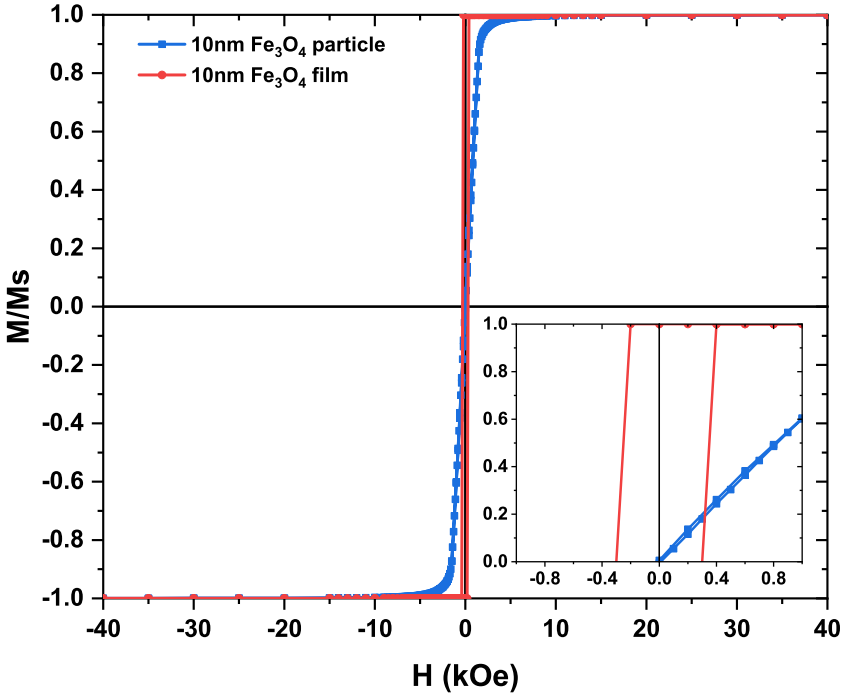

Fig. 6.10: *MH* curves of 10 nm sized Fe_3O_4 grains and 10 nm sized Fe_3O_4 film.

of 10 nm sized Fe_3O_4 films coated on 90 nm sized BaM layer. The *MH* curves show oddly shaped curves for the BaM/Fe_3O_4 nanocomposite with the volume ratio of 9:3 and 9:2 with noticeable separate coercivities and a smooth curve for the BaM/Fe_3O_4 nanocomposite with the volume ratio of 9:1. This smooth curve indicates a complete exchange-coupling between BaM and Fe_3O_4 films.

Figure 6.12 shows the hysteresis curves of up to 3 layers of 10 nm sized Fe_3O_4 grains, with superparamagnetic behaviour, coated on 90 nm sized BaM layer. The *MH* curves clearly show that the BaM/Fe_3O_4 nanocomposite with the volume ratio of 9:1 has a complete exchange-coupling between BaM and Fe_3O_4 grains while the curves, which represent the nanocomposites with volume ratios of 9:3 and 9:2, show two separate coercivities due to an incomplete exchange-coupling between the magnetic phases.

Figure 6.13 gives a more detailed magnetic characterisation comparing the simulation and experimental values. Both the experimental and simulated results are adjusted to the BaM volume fraction for better comparison. In both simulated and experimental results, the H_{ci} increases with the increase of BaM in the nanocompos-

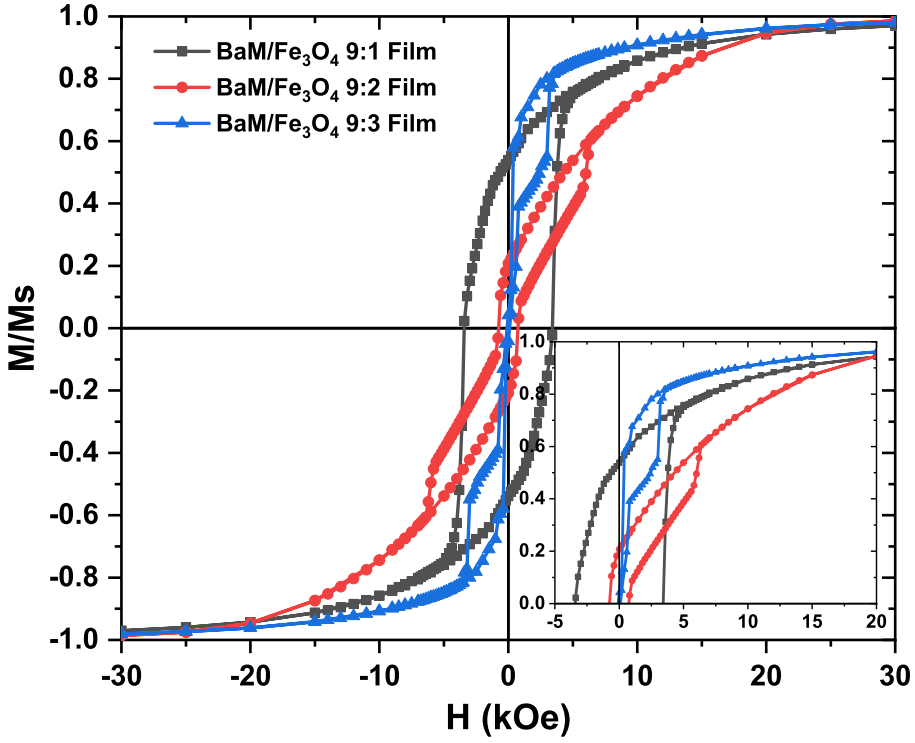

Fig. 6.11: *MH* curves of up to 3 layers of 10 nm sized Fe_3O_4 films coated on 90 nm sized BaM layer.

ite and reaches values in close proximity to the nanocomposites with $\sim$ 0.9 volume BaM (Figure 6.13(a)). However, the results show different values for the other volume fractions, namely $\sim$ 0.75 volume fraction of BaM. In the simulation, magnetite nanoparticles were sandwiched in between flat BaM layers and no soft magnetite particles were left in between of the BaM grains. However, TEM analysis of the prepared nanocomposites showed that each particle of BaM is coated with magnetite nanoparticles (Figure 4.12), which leads to a more complete interface for exchange coupling between the phases with an increase in the H_{ci}. In order to achieve more accurate comparison of $BH_{(max)}$ calculations, the M_s of the simulated phases were adjusted to the experimental values (Figure 6.13(b)). The results show comparable $BH_{(max)}$ values for the nanocomposite with $\sim$ 0.9 volume BaM between simulated model and experimental analysis. However, as a result of the reduced exchange coupling in the simulations for the $\sim$ 0.75 volume BaM, the calculated values of $BH_{(max)}$ are smaller in the simulated model.

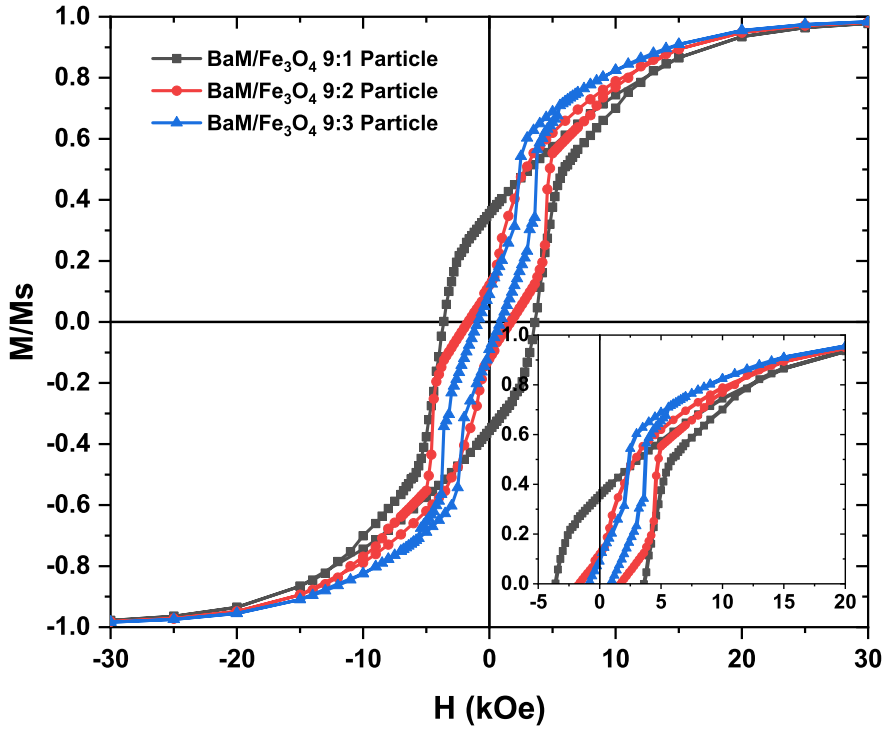

Fig. 6.12: *MH* curves of up to 3 layers of 10 nm sized Fe_3O_4 particles coated on 90 nm sized BaM layer.

While the data shown in Figure 6.13 present a comparison between the simulation and experimental results, we need to keep in mind that exchange-coupling behaviour is an interface dependent phenomenon and the geometry of the phase distribution plays an important role along with the volumetric phase fraction. To have a more realistic comparison, the contact surface of the hard and the soft phase should be considered. In the flat-slab geometry of the simulation model the thickness of the hard ferrite slabs, t_h, and the area of contact of hard and soft ferrites, S_{hs}, are held constant. In the geometry of experimental study with hard ferrite powder coated by the soft ferrite grains, the area of contact, S_{hs}, changes in proportion to the volume fraction of the hard ferrite phase, f_{vh}:

$$S_{hs} = S_{vh} \times f_{vh}, \tag{6.40}$$

where S_{vh} is the volumetric specific surface area of the BaM hard ferrite. Taking into account the analysed surface area from BET measurements (2.73 m^2/g for BaM) and

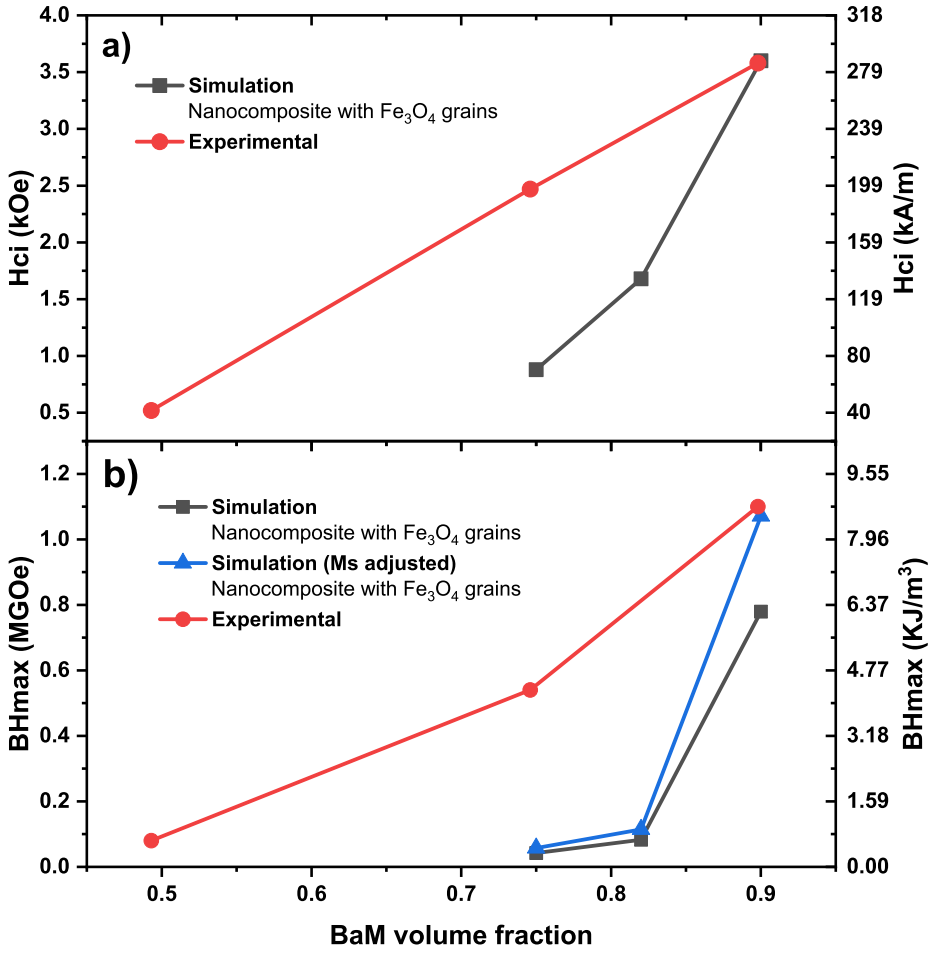

Fig. 6.13: Comparison between the (a) H_{ci}, and (b) $BH_{(max)}$ of the simulation and experimental results of BaM/Fe_3O_4 with different BaM volume fractions.

the density of BaM (5.28 g/cm^3), S_{vh} = 1.44 $\times 10^7$ m^{-1}.

In the geometry model, the average thickness is only dependent to the number of Fe_3O_4 layers (10 nm, 20 nm or 30 nm). However, in the experimental composite powder, the average thickness of the soft ferrite layer, t_s, is determined as

$$t_s = \frac{1}{S_{vh}}(\frac{1}{f_{vh}} - 1) \tag{6.41}$$

Figure 6.14 shows the variation of H_{ci} with average thickness of the soft ferrite. Considering the particle size distribution of Fe_3O_4 nanograins, void spaces and irregularity in the thickness of the Fe_3O_4 coating, the average thickness in the experimental results could be much lower than the estimated particle size of Fe_3O_4 nanoparticles

($\sim$ 10 nm). By increasing the average thickness of the soft ferrite, a weak or incomplete exchange-coupling between the magnetic phases occurs, and H_{ci} decreases. The largest coercivity is observed in a complete exchange coupling with a thin coating of Fe_3O_4 nanoparticles. It can be seen that both the simulation results and the calculated average thickness show a reasonable trend [130–132] for the dependence of H_{ci} of the composite with the average thickness of the soft phase.

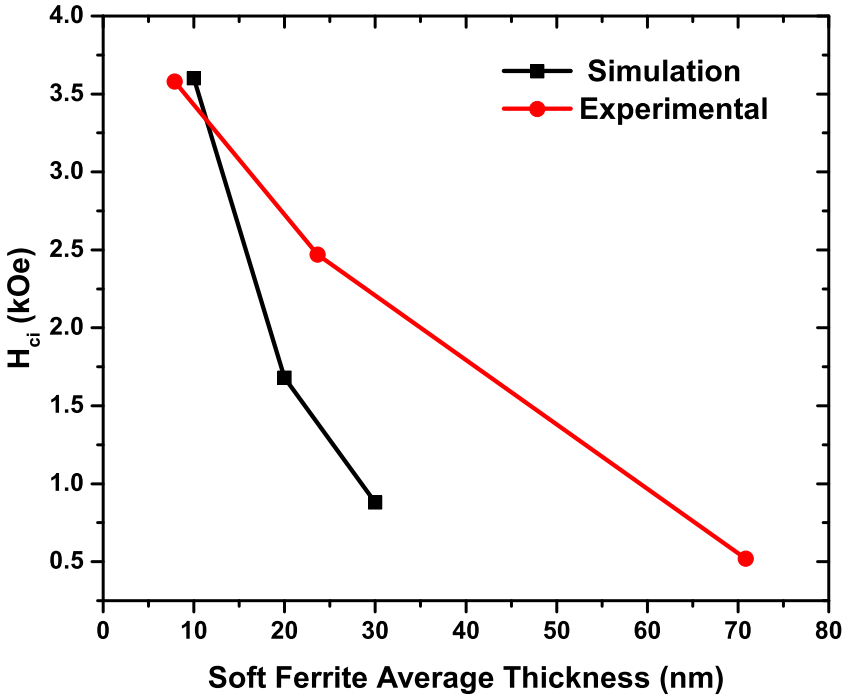

Fig. 6.14: Variation of H_{ci} with average thickness of the soft ferrite.

In order to improve the micromagnetic simulation of the nanocomposites of lower BaM volume fraction, a more complex simulation with lengthier computational time might be employed, namely a model of separate hexagonal shaped BaM particle coated with 10 nm sized magnetite nanoparticles. Recent micromagnetic simulations on single hexagonal particles showed a more rectangular shaped hysteresis curve [133]. Even though all the BaM particles might have similar sizes, the shape of the hysteresis curves might be improved by stacking several particles, each coated with magnetite particles.

6.5 Summary

In this study, the exchange coupling behaviour of the BaM/Fe_3O_4 hard-soft magnetic nanocomposites was investigated by micromagnetic simulations, employing the MuMax^3 software. The simulation results were compared with the experimental results. In order to study the effect of thickness on the H_{ci} of the BaM nanoparticles, 300 nm sized grains with thicknesses from 10 to 100 nm were simulated. The results showed that an increase in the thickness of the hard ferrite causes an increase in the H_{ci} and the grains with 50 and 60 nm of the hard ferrite showed a comparable H_{ci} with the previously analysed BaM nanoparticles prepared by a sol-gel autocombustion and annealed at 1000 °C for 5 h (Table 4.1).

Using different simulation models to achieve a superparamagnetic behaviour in the Fe_3O_4 nanoparticles, the proper magnetic behaviour was found to only be achievable by employing the recently added extension "ext_make3dgrains" of MuMax^3 with negligible intergranular exchange interaction.

The simulated hysteresis curve for the BaM/Fe_3O_4 nanocomposites with $\sim$ 0.9 BaM volume fraction showed comparable magnetic properties, such as $BH_{(max)}$ and H_{ci}, with previously studied experimentally prepared nanocomposites. Even though the experimental results on the nanocomposite with $\sim$ 0.75 BaM volume fraction shows an incomplete exchange coupling between the soft and the hard magnetic phases, the simulation results showed smaller H_{ci} and $BH_{(max)}$ compared to the experimental results. The employed sandwich simulation model of hard and soft magnetic phases causes less interparticle interactions which leads to a weaker exchange coupling in nanocomposites with larger volume fractions of Fe_3O_4 particles.

Chapter 7

Conclusions and Future Works

Recent economic and environmental concerns have prompted intensive research on the development and optimisation of rare-earth free permanent magnets. In this study, we investigated strategies to improve the hard magnetic properties of early generations of permanent magnets, in particular, Alnico magnets and M-type ferrites.

Alnico alloys are one of the most commonly used rare-earth free permanent magnets with high saturation magnetisation and relatively low coercivity. Recent studies on the Alnico V thin films have shown unusually high H_{ci} values compared to bulk Alnico magnets for heat treated thin films. In order to investigate the origin of the reported high coercivities, we studied the effects of different heat treatment processes on the morphology and crystal structure of high coercivity Alnico V thin films on Si substrates. The as-prepared Alnico V thin film samples were annealed in an Ar atmosphere. The results, seen in Chapter 3, show H_{ci} values of 1 kOe in the thin film sample heat-treated at 600 °C followed by quenching. Unexpected values of H_{ci} up to 1.8 kOe (4 times greater than the bulk Alnico V value) in the sample annealed at 800 °C were also achieved. It was observed that the pressure of Ar atmosphere during the heat treatment plays an important role to the H_{ci} of the samples. The high H_{ci} only appears in the samples annealed at above atmosphere pressure of Ar. Structural studies showed that the origin of this high coercivity is different from the formation of Fe-Co rich precipitations in Al-Ni matrix which causes the magnetic properties of bulk Alnico magnets. Unlike previous studies on Alnico thin films on Si substrates, high coercivity values were also observed in slow-cooled samples and in those with Ag

buffer layers. We show how Fe, Co and Ni atoms diffuse into the Si substrate and form triangular shaped precipitates along the interface between the substrate and the film inside the substrate, which are identified as MSi_2 disilicides (M= Ni, Co, Fe). While the presence of these precipitates is directly correlated to the observed high magnetic coercivity in the samples, the mechanism behind the magnetocrystalline anisotropy is not clear. Nonetheless, it could result from an inhomogeneous or layered positioning of atoms inside these features. Further studies are suggested to investigate the reason behind the formation of the triangular shaped features inside the substrate and to unravel the origin of the observed high coercivity values.

In Chapter 4, the exchange-coupling behaviour of BaM/Fe_3O_4 and SrM/Fe_3O_4 was investigated. M-type barium hexaferrites and strontium hexaferrites are technologically important, low-cost permanent magnets, with high T_C and high resistance to oxidation and corrosion. Their magnetic performance can be improved upon by exploring exchange-coupling mechanisms, to increase competitiveness with existing rare-earth magnets. In this part of the study, flake-like single phase BaM and SrM nanoparticles were synthesised using a sol-gel auto-combustion method followed by heat treatment. Well known chemical synthesising routes of producing nanoparticles, namely hydrothermal and coprecipitation methods, were used to coat BaM and SrM nanoparticles with Fe_3O_4 nanoparticles with different mass ratios. The structural analysis of the achieved BaM/Fe_3O_4 and SrM/Fe_3O_4 nanocomposites confirms the presence of the two magnetic phases with exchange-coupling behaviour being observed between the hard/soft magnetic phases. The magnetic measurements on the BaM/Fe_3O_4 nanocomposites indicate more than 40% increase in the M_s in each of the nanocomposites compared to the annealed BaM. Results also show a 75% increase in $BH(max)$ at room temperature in the BaM/Fe_3O_4 9:1 hard/soft nanocomposite, compared to the parent hard BaM phase. Results are significant in the sense that they represent an enhancement above 30% in the M_s and the $BH(max)$ of the prepared nanocomposite compared to a commercial BaM powder. Unlike previous studies on the exchange-coupling of BaM and Fe_3O_4 nanoparticles [55, 56], present results demonstrate that an additional post-heat treatment is not required, which reduces the cost and simplifies the preparation process. In contrast to the significant improvement in the magnetic properties of

the BaM/Fe_3O_4 9:1 nanocomposite, the SrM/Fe_3O_4 9:1 nanocomposite shows a moderate increase of $\sim$ 10% in the both M_s and $BH_{(max)}$, and a $\sim$ 20% decrease in the intrinsic coercivity in the nanocomposite compared to the parent hard SrM magnetic phase. This is attributed to the larger size and the wider size distribution of magnetite nanoparticles prepared via a coprecipitation method compared to those prepared via a hydrothermal method, which might cause an incomplete or weak exchange-coupling between particles of the soft and hard magnetic phases. This hypothesis is explored in the simulation work presented in Chapter 6.

In Chapter 5, we investigated the mechanical and magnetic properties of warm compressed high-performance low cost ferrite based exchange-coupled nanocomposites in an epoxy matrix. The bonded ferrite-based composite magnets were prepared via a warm compaction process at 180 °C for 10 *min* with different compaction pressures. The exchange-coupled magnetite coated BaM and SrM nanocomposites, prepared via a sol-gel autocombustion method followed by a hydrothermal or a coprecipitation method, were used as magnetic fillers, and epoxy powder was used as the matrix. The density of the bonded composite magnets increases with the increase of the ferrite concentration in the composite. No significant improvement in the density results from increasing the compaction pressure from 300 MPa up to 700 MPa. Excessive compaction pressure might actually cause a slight decrease in the density due to the formation of cracks in samples prepared at high pressures. The Vickers hardness test indicates that the samples with ferrite concentration of 90 wt.% prepared at 500 MPa for BaM/Fe_3O_4 and 700 MPa for SrM/Fe_3O_4 ferrites have maximised mechanical stability. Magnetic measurements on the bonded magnets show that $BH_{(max)}$ of the exchange-coupled BaM/Fe_3O_4 and SrM/Fe_3O_4 bonded magnets is up to 120% and 45% greater than a commercial bonded SrM magnet of comparable powder to polymer ratio, respectively. The increase in the SrM/Fe_3O_4 concentration from 80 to 95 wt.% in the composite magnet causes no significant improvement in the maximum energy product. In the BaM/Fe_3O_4 magnets, the $BH_{(max)}$ increased with the increase in the ferrite concentration. This might be due to the larger increase in the density of BaM/Fe_3O_4 compared to the SrM/Fe_3O_4 bonded magnets with the increase in the ferrite concentration. It is shown that the epoxy-bonded exchange-coupled SrM/Fe_3O_4 with the

ferrite concentration of 95 wt.% compressed at 700 MPa and the BaM/Fe_3O_4 with the ferrite concentration of 90 wt.% compressed at 500 MPa have optimised magnetic and mechanical properties.

In addition to the experimental works, a simplified model of the BaM/Fe_3O_4 nanocomposite was simulated using MuMax^3 micromagnetism software, presented in Chapter 6 . By employing the recently added extension "ext_make3dgrains" of MuMax^3 a superparamagnetic behaviour was observed in the simulated Fe_3O_4 nanoparticles, which later used in the nanocomposite simulation model. The simulated hysteresis curve for the BaM/Fe_3O_4 nanocomposites with ~ 0.9 BaM volume fraction have comparable magnetic properties, such as $BH_{(max)}$ and H_{ci}, to the experimental study of the nanocomposites. Even though the experimental results on the nanocomposite with ~ 0.75 BaM volume fraction shows an incomplete exchange coupling between the soft and the hard magnetic phases, the simulation results showed smaller H_{ci} and $BH_{(max)}$ compared to the experimental results. The employed sandwich simulation model of hard and soft magnetic phases causes less interparticle interactions which leads to a weaker exchange coupling in nanocomposites with larger volume fractions of Fe_3O_4 particles.

7.1 Future works

In this study, we investigated different approaches to improve the hard magnetic properties of Alnico and ferrite based magnets. Exploring nanostructured rare-earth free magnets provided new ideas for further investigations on this topic.

• For better understanding the origin of the high coercivity in Alnico V thin films and to perform a more detailed analysis on the observed triangular shaped precipitates, it would be interesting to explore the effect of different heat treatments on the multilayers of Alnico/Si nanocomposite. This might open new paths to create new rare-earth free permanent magnets based on this novel phase.

• Exploring the effects of applying different compaction techniques, such as spark plasma sintering (SPS) and injection moulding techniques in the presence of an external magnetic field to prepare bulk exchange-coupled ferrite based magnets. Our prelimi-

nary results on the spark plasma sintered BaM/Fe_3O_4 nanocomposites obtained with collaboration with Dr. Petra Jenus from Jožef Stefan institute in Slovenia have shown promising results.

• While the simulation results, shown in Chapter 6, regarding exchange-coupled nanocomposites are promising and comparable to the experimental results, preparing more complex simulation models could lead to optimising the phase ratios and distributions in different compositions and geometries, such as core-shells, thin films, physically mixed and coated composites, to predict and optimise the $BH_{(max)}$.

The path to industrial scaling production of high performance Alnico based rare-earth free permanent magnets would undoubtedly present many obstacles. On the other hand, our studies on the exchange-coupled ferrite based nanocomposites and on the fabrication of bonded magnets show that these high performance magnets can be produced in large scale. Even though that these improved and high performance rare-earth free magnets show lower $BH_{(max)}$ values compared to rare-earth base magnets, they can be used in multiple applications that a ferrite magnet has inadequate performances. This leads to a lower consumption of rare-earth based magnets and lower environmental and economic impacts. In this study, we showed a new method to prepare exchange-coupled nanocomposite magnets. An interesting approach might be to employ these same coating methods to prepare exchange-coupled rare-earth magnets to improve the performance alongside with reduction of rare-earth elements in the final product.

Bibliography

Author's Works

[P1] F. Mohseni, A. Baghizadeh, A. A. Lourenço, M. J. Pereira, V. S. Amaral, J. M. Vieira, and J. S. Amaral, "Interdiffusion Processes in High-Coercivity RF-Sputtered Alnico Thin Films on Si Substrates," *JOM*, vol. 69, no. 8, pp. 1427–1431, 2017, ISSN: 15431851. DOI: 10.1007/s11837-017-2382-y.

[P2] F. Mohseni, R. C. Pullar, J. M. Vieira, and J. S. Amaral, "Enhancement of maximum energy product in exchange-coupled $BaFe_{12}O_{19}/Fe_3O_4$ core-shell-like nanocomposites," *Journal of Alloys and Compounds*, vol. 806, pp. 120–126, Oct. 2019, ISSN: 09258388. DOI: 10.1016/j.jallcom.2019.07.162.

[P3] F. Mohseni, R. C. Pullar, J. M. Vieira, and J. S. Amaral, "Bonded ferrite-based exchange-coupled nanocomposite magnet produced by Warm compaction," *Journal of Physics D: Applied Physics*, accepted manuscript, Aug. 2020. DOI: 10.1007/s11837-017-2382-y.

[P4] C. O. Amorim, F. Mohseni, V. S. Amaral, and J. S. Amaral, "A geometry-independent moment correction method for the MPMS3 SQUID-VSM magnetometer," in preparation, 2020. [Online]. Available: arXiv:2007.07730.

References

[1] O. Gutfleisch, M. A. Willard, E. Brück, C. H. Chen, S. G. Sankar, and J. P. Liu, "Magnetic materials and devices for the 21st century: Stronger, lighter, and

more energy efficient," *Advanced Materials*, vol. 23, no. 7, pp. 821–842, 2011, ISSN: 09359648. DOI: 10.1002/adma.201002180.

[2] N. Poudyal and J. Ping Liu, "Advances in nanostructured permanent magnets research," *Journal of Physics D: Applied Physics*, vol. 46, p. 043 001, 2013, ISSN: 00223727. DOI: 10.1088/0022-3727/46/4/043001.

[3] M. J. Kramer, R. W. McCallum, I. A. Anderson, and S. Constantinides, "Prospects for non-rare earth permanent magnets for traction motors and generators," *JOM*, vol. 64, no. 7, pp. 752–763, 2012, ISSN: 10474838. DOI: 10.1007/s11837-012-0351-z.

[4] R. Skomski, P. Manchanda, P. K. Kumar, B. Balamurugan, A. Kashyap, and D. J. Sellmyer, "Predicting the future of permanent-magnet materials," *IEEE Transactions on Magnetics*, vol. 49, no. 7, pp. 3215–3220, 2013, ISSN: 00189464. DOI: 10.1109/TMAG.2013.2248139.

[5] B. D. Cullity and C. D. Graham, *Introduction to Magnetic Materials*, Second Edi. Wiley, 2008, ISBN: 9780470386323. DOI: 10.1002/9780470386323.

[6] S. Constantinides, *A manufacturing and performance comparison between bonded and sintered permanent magnets*, 2006.

[7] D. C. Jiles, *Recent advances and future directions in magnetic materials*, 2003. DOI: 10.1016/j.actamat.2003.08.011.

[8] J. M. D. Coey, *Magnetism and magnetic materials*. Cambridge: Cambridge University Press, 2010, pp. 9–10.

[9] H. W. Sung and C. Rudowicz, "Physics behind the magnetic hysteresis loop - A survey of misconceptions in magnetism literature," *Journal of Magnetism and Magnetic Materials*, vol. 260, no. 1-2, pp. 250–260, 2003, ISSN: 03048853. DOI: 10.1016/S0304-8853(02)01339-2.

[10] J. M. D. Coey, "Advances in Magnetics Hard Magnetic Materials : A Perspective," *IEEE Transactions on Magnetics*, vol. 47, no. 12, pp. 4671–4681, 2011, ISSN: 0018-9464. DOI: 10.1109/TMAG.2011.2166975.

[11] Arnold Magnetic Technologies, "The Vocabulary of Magnetism," *TECHNotes*, vol. 1602, 2016.

[12] R. Skomski and J. M. D. Coey, "Giant energy product in nanostructured two-phase magnets," *Physical Review B*, vol. 48, no. 21, pp. 15 812–15 816, 1993. DOI: 10.1103/PhysRevB.48.15812.

[13] E. A. Nesbitt and H. J. Williams, "Mechanism of Magnetization in Alnico V," *Physical review*, vol. 80, no. 1, pp. 112–113, 1950. DOI: doi.org/10.1103/PhysRev.80.112.2.

[14] C. Kittle, E. A. Nesbitt, and W. Shockley, "Theory of Magnetic Properties and Nucleation in Alnico V," *Physical review*, vol. 77, no. 6, pp. 839–840, 1950, ISSN: 00219606. DOI: 10.1063/1.1740416.

[15] R. B. Campbell and C. A. Julien, "Structure of Alnico v," *Journal of Applied Physics*, vol. 32, no. 3, pp. 1–4, 1961, ISSN: 00218979. DOI: 10.1063/1.2000397.

[16] C. A. Julien and F. G. Jones, "Alpha-sub-gamma phase in Alnico 8 alloys," *Journal of Applied Physics*, vol. 36, no. 3, pp. 1173–1174, 1965, ISSN: 00218979. DOI: 10.1063/1.1714155.

[17] A. Cochardt, "Recent ferrite magnet developments," *Journal of Applied Physics*, vol. 37, no. 3, pp. 1112–1115, 1966, ISSN: 00218979. DOI: 10.1063/1.1708357.

[18] K. Strnat, G. Hoffer, J. Olson, W. Ostertag, and J. J. Becker, "A family of new cobalt-base permanent magnet materials," *Journal of Applied Physics*, vol. 38, no. 3, pp. 1001–1002, 1967, ISSN: 00218979. DOI: 10.1063/1.1709459.

[19] M. Sagawa, S. Fujimura, N. Togawa, H. Yamamoto, and Y. Matsuura, "New material for permanent magnets on a base of Nd and Fe (invited)," *Journal of Applied Physics*, vol. 55, no. 6, pp. 2083–2087, 1984, ISSN: 00218979. DOI: 10.1063/1.333572.

[20] R. C. O'Handley, *Modern Magnetic Materials: Principles and Applications*. Wiley, 1999, p. 768, ISBN: 978-0-471-15566-9.

[21] Magnetic Materials Producers Association, "Standard Specifications for Permanent Magnet Materials," *Magnetic Materials Producers Association 8*, no. 0100-00, 2000. DOI: 10.1049/ic:20000454.

[22] K. H. J. Buschow, "New developments in hard magnetic materials," *Reports on Progress in Physics*, vol. 54, no. 9, pp. 1123–1213, 1991, ISSN: 0034-4885. DOI: 10.1088/0034-4885/54/9/001.

[23] A. S. Kim and F. E. Camp, "High performance NdFeB magnets (invited)," *Journal of Applied Physics*, vol. 79, no. 8, p. 5035, 1996, ISSN: 00218979. DOI: 10.1063/1.361566.

[24] C. Harland and H. Davies, "Magnetic properties of melt-spun Nd-rich NdFeB alloys with Dy and Ga substitutions," *Journal of Alloys and Compounds*, vol. 281, no. 1, pp. 37–40, 1998, ISSN: 09258388. DOI: 10.1016/S0925-8388(98)00767-1.

[25] S. Owen, *What Are Rare Earth Metals? What Are They Used For?* 2020. [Online]. Available: https://www.techmetalsresearch.com/guide/what-are-rare-earth-metals/%7B%5C#%7Dmore-86.

[26] D. J. Sellmyer, B. Balamurugan, W. Y. Zhang, B. Das, R. Skomski, P. Kharel, and Y. Liu, "Advances in Rare-Earth-Free Permanent Magnets," *Proceedings of the 8th Pacific Rim International Congress on Advanced Materials and Processing*, pp. 1689–1696, 2013. DOI: 10.1007/978-3-319-48764-9_212.

[27] B. Balasubramanian, B. Das, R. Skomski, W. Y. Zhang, and D. J. Sellmyer, "Novel nanostructured rare-earth-free magnetic materials with high energy products," *Advanced Materials*, vol. 25, no. 42, pp. 6090–6093, 2013, ISSN: 09359648. DOI: 10.1002/adma.201302704.

[28] L. Zhou, M. K. Miller, P. Lu, L. Ke, R. Skomski, H. Dillon, Q. Xing, A. Palasyuk, M. R. McCartney, D. J. Smith, S. Constantinides, R. W. McCallum, I. E. Anderson, V. Antropov, and M. J. Kramer, "Architecture and magnetism of alnico," *Acta Materialia*, vol. 74, pp. 224–233, 2014, ISSN: 13596454. DOI: 10.1016/j.actamat.2014.04.044.

[29] D. Pătroi, D. Bojin, and E. A. Pătroi, "Magnetic and structural behaviour of alnico thin films," *UPB Scientific Bulletin, Series B: Chemistry and Materials Science*, vol. 74, no. 2, pp. 211–220, 2012, ISSN: 14542331.

[30] J. J. Went, G. W. Rathenau, E. W. Gorter, and O. G. W. Van, "Hexagonal Iron-Oxide Compounds as Permanent-Magnet Materials," *Physical review*, vol. 86, no. 3, pp. 424–425, 1952.

[31] R. C. Pullar, "Hexagonal ferrites: A review of the synthesis, properties and applications of hexaferrite ceramics," *Progress in Materials Science*, vol. 57, no. 7, pp. 1191–1334, 2012, ISSN: 00796425. DOI: 10.1016/j.pmatsci.2012.04.001.

[32] Y. Liu, Y. Li, Y. Liu, H. S. Yin, L. L. Wang, K. Sun, and Y. Gao, "Structure information of barium hexaferrite and strategies for its syntheses," *Applied Mechanics and Materials*, vol. 69, no. July 2011, pp. 6–11, 2011, ISSN: 16609336. DOI: 10.4028/www.scientific.net/AMM.69.6.

[33] P. Shepherd, K. K. Mallick, and R. J. Green, "Magnetic and structural properties of M-type barium hexaferrite prepared by co-precipitation," *Journal of Magnetism and Magnetic Materials*, vol. 311, no. 2, pp. 683–692, 2007, ISSN: 03048853. DOI: 10.1016/j.jmmm.2006.08.046.

[34] Ü. Özgür, Y. Alivov, and H. Morkoç, *Microwave ferrites, part 1: Fundamental properties*, 9. 2009, vol. 20, pp. 789–834, ISBN: 1085400999. DOI: 10.1007/s10854-009-9923-2.

[35] X. Obradors, F. D. Fisica, U. D. Barcelona, X. Solans, D. D. Cristallografia, F. D. Geologia, A. Collomb, L. D. Cristallographie, D. Samaras, V. Aristote, J. Rodriguez, M. Pernet, and D. D. Cristallografa, "Crystal Structure of Strontium Hexaferrite $SrFe_{12}O_{19}$," *Journal of Solid State Chemistry*, vol. 72, pp. 218–224, 1988. DOI: 10.1016/0022-4596(88)90025-4.

[36] M. Ghobeiti-Hasab, "Production of Sr-Ferrite Sub-Micron Powder by Conventional and Sol-Gel Auto-Combustion Methods," *International Scholarly and Scientific Research & Innovation*, vol. 8, no. 12, pp. 1363–1366, 2014.

[37] A. Ataie, S. Heshmati-Manesh, and H. Kazempour, "Synthesis of barium hexaferrite by the co-precipitation method using acetate precursor," *Journal of Materials Science*, vol. 37, no. 10, pp. 2125–2128, 2002, ISSN: 00222461. DOI: 10.1023/A:1015254221872.

[38] K. Li, H. Gu, and Q. Wei, "A novel hydrothermal synthesis method for barium ferrite," *China Particuology*, vol. 2, no. 1, pp. 41–43, 2004, ISSN: 16722515. DOI: 10.1016/S1672-2515(07)60019-0.

[39] A. Sutka and G. Mezinskis, "Sol-gel auto-combustion synthesis of spinel-type ferrite nanomaterials," *Frontiers of Materials Science*, vol. 6, no. 2, pp. 128–141, 2012, ISSN: 2095025X. DOI: 10.1007/s11706-012-0167-3.

[40] S. D. Bader, "Colloquium: Opportunities in nanomagnetism," *Reviews of Modern Physics*, vol. 78, no. 1, 2006, ISSN: 00346861. DOI: 10.1103/RevModPhys.78.1.

[41] R. Coehoorn, D. B. de Mooij, and C. de Waard, "Meltspun permanent magnet materials containing Fe_3B as the main phase," *Journal of Magnetism and Magnetic Materials*, vol. 80, no. 1, pp. 101–104, 1989, ISSN: 03048853. DOI: 10.1016/0304-8853(89)90333-8.

[42] E. F. Kneller and R. Hawig, "The Exchange-Spring Magnet: A New Material Principle for Permanent Magnets," *IEEE Transactions on Magnetics*, vol. 27, no. 4, pp. 3588–3600, 1991. DOI: 10.1109/20.102931.

[43] I. Panagiotopoulos, L. Withanawasam, and G. C. Hadjipanayis, *'Exchange spring' behavior in nanocomposite hard magnetic materials*, 1996. DOI: 10.1016/0304-8853(95)00467-X.

[44] T. Schrefl, J. Fidler, and H. Kronmüller, "Remanence and coercivity in isotropic nanocrystalline permanent magnets," *Physical Review B*, vol. 49, no. 9, pp. 6100–6110, 1994. DOI: 10.1103/PhysRevB.49.6100.

[45] V. Kuncser, G. Schinteie, A. Birsan, and W. Keune, "Interfacial Spin Configuration in Exchange Coupled Magnetic Phase: Exchange-Spring and Exchange-Bias Systems," in *Advances in Physics and Astrophysics of the 21st Century*, 2005.

[46] A. Manaf, R. A. Buckley, and H. A. Davies, "New nanocrystalline high-remanence Nd-Fe-B alloys by rapid solidification," *Journal of Magnetism and Magnetic Materials*, vol. 128, no. 3, pp. 302–306, 1993, ISSN: 03048853. DOI: 10.1016/0304-8853(93)90475-H.

[47] L. Withanawasam, G. C. Hadjipanayis, and R. F. Krause, "Enhanced remanence in isotropic Fe-rich melt-spun Nd-Fe-B ribbons," *Journal of Applied Physics*, vol. 75, no. 10, pp. 6646–6648, 1994, ISSN: 00218979. DOI: 10.1063/1.356882.

[48] J. P. Liu, C. P. Luo, Y. Liu, and D. J. Sellmyer, "High energy products in rapidly annealed nanoscale Fe/Pt multilayers," *Applied Physics Letters*, vol. 72, no. 4, pp. 483–485, 1998, ISSN: 00036951. DOI: 10.1063/1.120793.

[49] K. H. Chen, Z. Q. Jin, J. Li, G. Kennedy, Z. L. Wang, N. N. Thadhani, H. Zeng, S. F. Cheng, and J. P. Liu, "Bulk nanocomposite magnets produced by dynamic shock compaction," *Journal of Applied Physics*, vol. 96, no. 2, pp. 1276–1278, 2004, ISSN: 00218979. DOI: 10.1063/1.1760834.

[50] C. B. Rong, V. Nandwana, N. Poudyal, J. P. Liu, T. Saito, Y. Wu, and M. J. Kramer, "Bulk FePt/Fe_3Pt nanocomposite magnets prepared by spark plasma sintering," *Journal of Applied Physics*, vol. 101, no. 9, pp. 7–10, 2007, ISSN: 00218979. DOI: 10.1063/1.2710811.

[51] C. B. Rong, V. Nandwana, N. Poudyal, J. P. Liu, M. E. Kozlov, R. H. Baughman, Y. Ding, and Z. L. Wang, "Bulk FePt-based nanocomposite magnets with enhanced exchange coupling," *Journal of Applied Physics*, vol. 102, no. 2, 2007, ISSN: 00218979. DOI: 10.1063/1.2756619.

[52] O. Akdogan and G. C. Hadjipanayis, "Alnico thin films with high coercivities up to 6.9 kOe," *Journal of Physics: Conference Series*, vol. 200, no. 7, p. 072 001, 2010, ISSN: 1742-6596. DOI: 10.1088/1742-6596/200/7/072001.

[53] O. Akdogan, W. Li, and G. Hadjipanayis, "High coercivity of Alnico thin films: Effect of Si substrate and the emergence of a novel magnetic phase," *Journal of Nanoparticle Research*, vol. 14, no. 6, p. 891, 2012, ISSN: 13880764. DOI: 10.1007/s11051-012-0891-8.

[54] R. K. Sharma and R. Ghose, "Synthesis and characterization of nanocrystalline zinc ferrite spinel powders by homogeneous precipitation method," *Ceramics International*, vol. 41, no. 10, pp. 14 684–14 691, 2015, ISSN: 02728842. DOI: 10.1016/j.ceramint.2015.07.191.

[55] Y. Lin, Y. Liu, J. Dai, L. Wang, and H. Yang, "Synthesis and microwave absorption properties of plate-like $BaFe_{12}O_{19}$@Fe_3O_4 core-shell composite," *Journal of Alloys and Compounds*, vol. 739, pp. 202–210, 2018, ISSN: 09258388. DOI: 10.1016/j.jallcom.2017.12.086. [Online]. Available: https://doi.org/10.1016/j.jallcom.2017.12.086.

[56] K. P. Remya, D. Prabhu, S. Amirthapandian, C. Viswanathan, and N. Ponpandian, "Exchange spring magnetic behavior in $BaFe_{12}O_{19}/Fe_3O_4$ nanocomposites," *Journal of Magnetism and Magnetic Materials*, vol. 406, pp. 233–238, 2016, ISSN: 03048853. DOI: 10.1016/j.jmmm.2016.01.024.

[57] N. Mizutani, T. Iwasaki, S. Watano, T. Yanagida, and T. Kawai, "Size control of magnetite nanoparticles in hydrothermal synthesis by coexistence of lactate and sulfate ions," *Current Applied Physics*, vol. 10, no. 3, pp. 801–806, 2010, ISSN: 15671739. DOI: 10.1016/j.cap.2009.09.018.

[58] J. Stabik, A. Chrobak, G. Haneczok, and A. Dybowska, "Magnetic properties of polymer matrix composites filled with ferrite powders," *Archives of Materials Science and Engineering*, vol. 48, no. 2, pp. 97–102, 2011, ISSN: 18972764.

[59] D. Plusa, M. Dospial, B. Slusarek, U. Kotlarczyk, and T. Mydlarz, "On the magnetic properties of bonded magnets made from a mixture of Nd(Fe, Co)B and strontium ferrite or Alnico powder," *REVIEWS ON ADVANCED MATERIALS SCIENCE*, vol. 18, pp. 541–544, 2008.

[60] C. Muntenita, V. Bria, C. Eni, A. Circiumaru, and I. Graur, "Physical characterization of nano-ferrites modified epoxy resins," *Materiale Plastice*, vol. 53, no. 3, pp. 509–511, 2016, ISSN: 00255289.

[61] C. Munteniţă, C. Eni, I. Graur, C. Ungureanu, and M. Bodor, "A study of friction wear behaviour of nano-ferite modified epoxy resins," *IOP Conference*

Series: Materials Science and Engineering, vol. 174, no. 1, 2017, ISSN: 1757899X. DOI: 10.1088/1757-899X/174/1/012025.

[62] M. H. Makled, T. Matsui, H. Tsuda, H. Mabuchi, M. K. El-Mansy, and K. Morii, *Magnetic and dynamic mechanical properties of barium ferrite-natural rubber composites*, 2005. DOI: 10.1016/j.jmatprotec.2004.06.013.

[63] M. R. Anantharaman, K. A. Malini, S. Sindhu, E. M. Mohammed, S. K. Date, S. D. Kulkarni, P. A. Joy, and P. Kurian, "Tailoring magnetic and dielectric properties of rubber ferrite composites containing mixed ferrites," *Bulletin of Materials Science*, vol. 24, no. 6, pp. 623–631, 2001, ISSN: 02504707. DOI: 10.1007/BF02704011.

[64] W. Liu, W. Xi, R. Hu, M. Yue, Y. Yin, J. Guo, D. Zhang, and H. Zhang, "Preparation and characterization of sodium silicate/epoxy resin composite bonded Nd-Fe-B magnets with high performance," *Journal of Rare Earths*, vol. 37, 1083=1087, 2019. DOI: 10.1016/j.jre.2019.03.012.

[65] M. P. Paranthaman, C. S. Shafer, A. M. Elliott, D. H. Siddel, M. A. McGuire, R. M. Springfield, J. Martin, R. Fredette, and J. Ormerod, "Binder Jetting: A Novel NdFeB Bonded Magnet Fabrication Process," *JOM*, vol. 68, no. 7, pp. 1978–1982, 2016, ISSN: 15431851. DOI: 10.1007/s11837-016-1883-4.

[66] D. Sumanth Kumar, B. Jai Kumar, and H. Mahesh, "Quantum Nanostructures (QDs): An Overview," in *Synthesis of Inorganic Nanomaterials*, Elsevier Ltd., 2018, pp. 59–88, ISBN: 9780081019757. DOI: 10.1016/b978-0-08-101975-7.00003-8.

[67] S. Feng, "Introductory Chapter: Basic Theory of Magnetron Sputtering," in *IntechOpen*, 2018. DOI: 10.5772/intechopen.80550.

[68] P. J. Kelly and R. D. Arnell, *Magnetron sputtering: A review of recent developments and applications*, 2000. DOI: 10.1016/S0042-207X(99)00189-X.

[69] G. Bräuer, "Magnetron Sputtering," *Physics in Technology*, vol. 19, pp. 57–73, 1988. DOI: 10.1016/B978-0-08-096532-1.00403-9.

[70] G. Will, *Powder Diffraction: The Rietveld Method and the Two-Stage Method*. 2006, p. 224, ISBN: 3540279857. DOI: 10.1007/3-540-27986-5. arXiv: arXiv:1011.1669v3.

[71] Phylips Analytical, *Basic XRD Theory*. 1968, p. 119. [Online]. Available: https://engineering.jhu.edu/labs/wp-content/uploads/sites/76/2016/04/Phillips-Basic-XRD-Theory.pdf.

[72] M. Birkholz, "Principles of X-ray Diffraction Diffraction," in *Thin Film Analysis by X-Ray Scattering*, 2006, pp. 1–42, ISBN: 9783527310524. DOI: 10.1002/3527607595.

[73] J. Dailland and A. Gibaud, *X-ray and Neutron Reflectivity: Principles and Applications*. Springer-Verlag Berlin Heidelberg, 2009, p. 350, ISBN: 978-3-540-88587-0. DOI: 10.1007/978-3-540-88588-7.

[74] A. Gibaus, M. Chebil, and T. Beuvier, "Surface science techniques," in *Springer Series in Surface Sciences*, vol. 51, 2013, ch. X-Ray Refl, pp. 191–216, ISBN: 9783642342431. DOI: 10.1007/978-3-642-34243-1_7.

[75] M. Tolan, *X-Ray Scattering from Soft-Matter Thin Films*. Springer-Verlag Berlin Heidelberg, 1999, p. 198, ISBN: 978-3-540-49525-3. DOI: 10.1007/bfb0112834.

[76] F. Jiménez-Villacorta, *X-Ray Reflectivity Measurement*. [Online]. Available: https://www.slideserve.com/drew-bray/x-ray-reflectivity-measurement-from-chapter-10-of-textbook-2.

[77] K. Akhtar, S. Ali Khan, S. Bahadar Khan, and A. M. Asiri, "Handbook of Materials Characterization," in *Handbook of Materials Characterization*, Springer International Publishing AG, 2018, ch. Scanning E, pp. 113–145, ISBN: 9783319929552. DOI: 10.1007/978-3-319-92955-2_4.

[78] D. McMullan, "Scanning Electron Microscopy," *51st Annual Meeting of the Microscopy Society of America*, vol. 17, pp. 175–185, 1995.

[79] D. B. Wiliams and C. B. Carter, *Transmission Electron Microscopes*. 2009, p. 760, ISBN: 9780387765006. DOI: 10.1007/978-1-4757-2519-3_1.

[80] S. Amelinckx, D. van Dyck, J. van Landuyt, and G. van Tendeloo, *Electron Microscopy: Principles and Fundamentals*. Wiley, 2008, p. 527, ISBN: 978-3-527-61455-4.

[81] M. Weyland, "Electron tomography of catalysts," *Topics in Catalysis*, vol. 21, no. 4, pp. 175–183, 2002.

[82] J. Clarke and A. I. Braginski, *The SQUID Handbook*. 2005, vol. 1, p. 414, ISBN: 9783527603640. DOI: 10.1002/3527603646.

[83] P. Marcon and K. Ostanina, "Overview of methods for magnetic susceptibility measurement," *Progress in Electromagnetics Research Symposium Proceedings*, pp. 420–424, 2012, ISSN: 15599450.

[84] "MPMS SQUID VSM User's Manual,1500-100, Rev E0," 2010.

[85] W. Sun, "Principles of atomic force microscopy," in *Atomic Force Microscopy in Molecular and Cell Biology*, J. Cai, Ed. Singapore: Springer Singapore, 2018, pp. 1–28, ISBN: 978-981-13-1510-7. DOI: 10.1007/978-981-13-1510-7_1. [Online]. Available: https://doi.org/10.1007/978-981-13-1510-7_1.

[86] P. Zhang, S. X. Li, and Z. F. Zhang, "General relationship between strength and hardness," *Materials Science and Engineering A*, vol. 529, no. 1, pp. 62–73, 2011, ISSN: 09215093. DOI: 10.1016/j.msea.2011.08.061.

[87] J. R. Davis, *Metals Handbook Desk Edition*. ASM International, 1998, p. 1521, ISBN: 978-0-87170-654-6.

[88] *Vickers standards and test methods*, 2006. [Online]. Available: http://wolpertgroup.com/old%7B%5C_%7Dsite/pages/06%7B%5C_%7DApplications/appl%7B%5C_%7Dvickers.php.

[89] *Operating Instructions Density Determination Set for Analytical Balance*. KERN & Sohn GmbH, 2012.

[90] P. Kumar, M. G. Krishna, and a. K. Bhattacharya, "Effect of microstructural evolution on magnetic properties of Ni thin films," *Bulletin of Materials Science*, vol. 32, no. 3, pp. 263–270, 2009. DOI: 10.1007/s12034-009-0040-x.

[91] S. Langkau, G. Wagner, G. Kloess, and M. Heuer, "TEM analysis of (Ni,Fe)Si_2 precipitates in Si," *Physica Status Solidi (a)*, vol. 207, no. 8, pp. 1832–1844, 2010, ISSN: 18626300. DOI: 10.1002/pssa.200925309.

[92] G. Sharma and C. A. Grimes, "Synthesis, characterization, and magnetic properties of FeCoNi ternary alloy nanowire arrays," *Journal of Materials Research*, vol. 19, no. 12, pp. 3695–3703, 2004, ISSN: 0884-2914. DOI: 10.1557/JMR.2004.0476.

[93] P. Fu, G. Chen, Y. Xu, P. Cai, and X. H. Wang, "Electrodeposition and magnetic properties of ternary Fe-Co-Ni alloy nanowire arrays with high squareness ratio," *Materials Science-Poland*, vol. 30, no. 3, pp. 259–263, 2012, ISSN: 2083-1331. DOI: 10.2478/s13536-012-0031-2.

[94] N. K. Prasad and V. Kumar, "Structure-magnetic properties correlation in mechanically alloyed nanocrystalline Fe-Co-Ni-(Mg-Si)x alloy powders," *Journal of Materials Science: Materials in Electronics*, vol. 27, no. 10, pp. 10 136–10 146, 2016, ISSN: 1573482X. DOI: 10.1007/s10854-016-5090-4.

[95] S. K. Vajpai, B. V. Mahesh, and R. K. Dube, "Studies on the bulk nanocrystalline Ni-Fe-Co alloy prepared by mechanical alloying-sintering-hot rolling route," *Journal of Alloys and Compounds*, vol. 476, no. 1-2, pp. 311–317, 2009, ISSN: 09258388. DOI: 10.1016/j.jallcom.2008.08.051.

[96] H. Raanaei, H. Eskandari, and V. Mohammad-Hosseini, "Structural and magnetic properties of nanocrystalline Fe-Co-Ni alloy processed by mechanical alloying," *Journal of Magnetism and Magnetic Materials*, vol. 398, pp. 190–195, 2016, ISSN: 03048853. DOI: 10.1016/j.jmmm.2015.09.031.

[97] S. Liang, R. Islam, D. J. Smith, P. A. Bennett, J. R. O'Brien, and B. Taylor, "Magnetic iron suicide nanowires on Si(110)," *Applied Physics Letters*, vol. 88, no. 11, pp. 23–25, 2006, ISSN: 00036951. DOI: 10.1063/1.2185610.

[98] W. Tang, B. M. Nguyen, R. Chen, and S. A. Dayeh, "Solid-state reaction of nickel silicide and germanide contacts to semiconductor nanochannels," *Semiconductor Science and Technology*, vol. 29, no. 5, 2014, ISSN: 13616641. DOI: 10.1088/0268-1242/29/5/054004.

[99] C. W. Lim, C. S. Shin, D. Gall, J. M. Zuo, I. Petrov, and J. E. Greene, "Growth of $CoSi_2$ on Si(001) by reactive deposition epitaxy," *Journal of Applied Physics*, vol. 97, no. 4, pp. 1–6, 2005, ISSN: 00218979. DOI: 10.1063/1.1774263.

[100] C. H. T. Chang, P. C. Jiang, Y. T. Chow, H. L. Hsiao, W. B. Su, and J. S. Tsay, "Enhancing silicide formation in Ni/Si(111) by Ag-Si particles at the interface," *Scientific Reports*, vol. 9, no. 1, pp. 1–10, 2019, ISSN: 20452322. DOI: 10.1038/s41598-019-45104-3. [Online]. Available: http://dx.doi.org/10.1038/s41598-019-45104-3.

[101] R. Xiong, W. Li, C. Fei, Y. Liu, and J. Shi, "Exchange-spring behavior in $BaFe_{12}O_{19}$-$Ni_{0.5}Zn_{0.5}Fe_2O_4$ nanocomposites synthesized by a combustion method," *Ceramics International*, vol. 42, no. 10, pp. 11 913–11 917, 2016, ISSN: 02728842. DOI: 10.1016/j.ceramint.2016.04.114.

[102] H. Yang, T. Ye, Y. Lin, M. Liu, P. Kang, and G. Zhang, "Enhancements of (BH)max and remanence in $BaFe_{12}O_{19}/CaFe_2O_4/CoFe_2O_4$ nanocomposite powders by exchange-coupling mechanism," *Materials Chemistry and Physics*, vol. 171, pp. 27–32, 2016, ISSN: 02540584. DOI: 10.1016/j.matchemphys.2016.01.010.

[103] F. Song, X. Shen, M. Liu, and J. Xiang, "Magnetic hard/soft nanocomposite ferrite aligned hollow microfibers and remanence enhancement," *Journal of Colloid and Interface Science*, vol. 354, no. 1, pp. 413–416, 2011, ISSN: 00219797. DOI: 10.1016/j.jcis.2010.11.020.

[104] C. A. Herme, P. G. Bercoff, and S. E. Jacobo, "Formation of a magnetic composite by reduction of Co-Nd doped strontium hexaferrite in a hydrogen gas flow," *Physica B: Condensed Matter*, vol. 407, no. 16, pp. 3102–3105, 2012, ISSN: 09214526. DOI: 10.1016/j.physb.2011.12.036.

[105] L. H. Lewis and F. Jiménez-Villacorta, "Perspectives on permanent magnetic materials for energy conversion and power generation," *Metallurgical and Materials Transactions A: Physical Metallurgy and Materials Science*, vol. 44, no. SUPPL. 1, pp. 2–20, 2013, ISSN: 10735623. DOI: 10.1007/s11661-012-1278-2.

[106] E. Roohani, H. Arabi, R. Sarhaddi, S. Sudkhah, and A. Shabani, "Effect of annealing temperature on structural and magnetic properties of strontium hexaferrite nanoparticles synthesized by sol-gel auto-combustion method," *International Journal of Modern Physics B*, vol. 29, no. 27, pp. 1–11, 2015, ISSN: 17936578. DOI: 10.1142/S0217979215501908.

[107] S. Alamolhoda, S. A. Seyyed Ebrahimi, and A. Badiei, *A study on the formation of strontium hexaferrite nanopowder by a sol-gel auto-combustion method in the presence of surfactant*, 2006. DOI: 10.1016/j.jmmm.2005.10.194.

[108] H.-c. Wu, S. K. Arora, O. N. Mryasov, and I. V. Shvets, "Antiferromagnetic interlayer exchange coupling between Fe_3O_4 layers across a nonmagnetic MgO dielectric layer," *Applied Physics Letters*, vol. 92, no. 18, p. 182 502, 2008. DOI: 10.1063/1.2919081.

[109] J. M. D. Coey, *Magnetism and Magnetic Materials*, 1-2. 2009, vol. 46, ISBN: 978-0-511-67743-4. arXiv: arXiv:1011.1669v3.

[110] A. Verma, O. P. Pandey, and P. Sharma, "Strontium ferrite permanent magnet - An overview," *Indian Journal of Engineering and Materials Sciences*, vol. 7, no. 5-6, pp. 364–369, 2000, ISSN: 09714588. DOI: 10.1002/chin.200138258.

[111] Y. Hou, J. Yu, and S. Gao, "Solvothermal reduction synthesis and characterization of superparamagnetic magnetite nanoparticles," *Journal of Materials Chemistry*, vol. 13, no. 8, pp. 1983–1987, 2003, ISSN: 09599428. DOI: 10.1039/b305526d.

[112] B. K. Rai, L. Wang, S. R. Mishra, V. V. Nguyen, and J. P. Liu, "Synthesis and Magnetic Properties of Hard-Soft $SrFe_{10}Al_2O_{19}/NiZnFe_2O_4$ Ferrite Nanocomposites," *Journal of Nanoscience and Nanotechnology*, vol. 14, no. 7, pp. 5272–5277, 2014, ISSN: 15334880. DOI: 10.1166/jnn.2014.8836.

[113] H. Shokrollahi and K. Janghorban, "Soft magnetic composite materials (SMCs)," *Journal of Materials Processing Technology*, vol. 189, pp. 1–12, 2007. DOI: 10.1016/j.jmatprotec.2007.02.034.

[114] A. Vansteenkiste, J. Leliaert, M. Dvornik, M. Helsen, F. Garcia-Sanchez, and B. Van Waeyenberge, "The design and verification of MuMax3," *AIP Advances*, vol. 4, no. 10, 2014, ISSN: 21583226. DOI: 10.1063/1.4899186. arXiv: 1406.7635.

[115] H. Kronmüller, *General Micromagnetic Theory and Applications*. 2019, pp. 1–43, ISBN: 9783527603978. DOI: 10.1002/9783527603978.mst0460.

[116] W. Heisenberg, "Zur Theorie des Ferromagnetismus," *Zeitschrift für Physik*, vol. 49, no. 9-10, pp. 619–636, 1928, ISSN: 14346001. DOI: 10.1007/BF01328601.

[117] S. Blundell, *Magnetism in Condensed Matter*. Oxford Master Series in Physics, 2001, p. 256, ISBN: 9780198505914.

[118] H. Kronmüller and M. Fähnle, *Micromagnetism and the Microstructure of Ferromagnetic Solids*. Cambridge University Press, 2003, p. 450, ISBN: 9780521331357.

[119] *http://wpage.unina.it/mdaquino/PhD_thesis/main/node12.html*.

[120] R. C. O'Handley, *Modern Magnetic Materials: Principles and Applications*. Wiley, 2000, p. 768, ISBN: 978-0-471-15566-9.

[121] A. Hubert and R. Schäfer, *Magnetic Domains The Analysis of Magnetic Microstructures*. Springer-Verlag Berlin Heidelberg, 1998, p. 696, ISBN: 978-3-540-85054-0. DOI: 10.1007/978-3-540-85054-0.

[122] L. LANDAU and E. LIFSHITZ, "On the theory of the dispersion of magnetic permeability in ferromagnetic bodies," *Perspectives in Theoretical Physics*, vol. 169, no. 14, pp. 51–65, 1992. DOI: 10.1016/b978-0-08-036364-6.50008-9.

[123] T. L. Gilbert, "Lagrangian formulation of the gyromagnetic equation of the magnetization field," *Physical review*, no. 100, pp. 1243–1243, 1955.

[124] *The Go Programming Language https://golang.org/*. [Online]. Available: https://golang.org/.

[125] *NVIDIA CUDA C programming guide*, 2020. [Online]. Available: https://docs.nvidia.com/cuda/index.html.

[126] M. J. Donahue and D. G. Porter, "OOMMF user's guide, version 1.0," *National Institute of Standards and Technology*, 1999.

[127] J. Fidler and T. Schrefl, "Micromagnetic modelling - The current state of the art," *Journal of Physics D: Applied Physics*, vol. 33, no. 15, 2000, ISSN: 00223727. DOI: 10.1088/0022-3727/33/15/201.

[128] G. S. Abo, Y. K. Hong, J. Park, J. Lee, W. Lee, and B. C. Choi, "Definition of magnetic exchange length," *IEEE Transactions on Magnetics*, vol. 49, no. 8, pp. 4937–4939, 2013, ISSN: 00189464. DOI: 10.1109/TMAG.2013.2258028.

[129] S. Mørup, M. F. Hansen, and C. Frandsen, "Magnetic interactions between nanoparticles," *Beilstein Journal of Nanotechnology*, vol. 1, no. 1, pp. 182–190, 2010, ISSN: 21904286. DOI: 10.3762/bjnano.1.22.

[130] V. Skumryev, S. Stonyanov, Y. Zhang, G. C. Hadjipanayis, D. Givord, and J. Nogués, "Beating the superparamagnetic limit with exchange bias," *Nature*, vol. 423, no. June, pp. 850–853, 2003. DOI: 10.1038/nature01687..

[131] G. Lavorato and E. Winkler, "Thickness dependence of exchange coupling in epitaxial $Fe_3O_4/CoFe_2O_4$ soft/hard magnetic bilayers," *Physical Review B*, vol. 054405, no. 94, pp. 1–6, 2016. DOI: 10.1103/PhysRevB.94.054405.

[132] E. E. Fullerton, J. S. Jiang, and S. D. Bader, "Hard/soft magnetic heterostructures : model exchange-spring magnets," *Journal of Magnetism and Magnetic Materials*, vol. 200, no. 1-3, pp. 392–404, 1999. DOI: 10.1016/S0304-8853(99)00376-5.

[133] D. Djuhana, D. Oktri, and C. Kurniawan, "Micromagnetic Study on the Magnetization Reversal of Barium Hexaferrite ($BaFe_{12}O_{19}$) Thin Film," *Makara Journal of Science*, vol. 22, no. 4, pp. 198–204, 2018. DOI: 10.7454/mss.v22i4.9986.